UNIVERSITÄT ZU LÜBECK

From the Institute of Biomedical Optics
of the University of Lübeck
Director: Prof. Dr. Robert Huber

Automated Selective Retina Therapy

Dissertation
for Fulfillment of Requirements
for the Doctoral Degree
of the University of Lübeck

from the Department of Natural Sciences

Submitted by
Eric Seifert
from Görlitz (Germany)

Lübeck, 2023

First referee: Prof. Dr. Reginald Birngruber

Second referee: Prof. Dr. Christian Hübner

Chair: Prof. Dr. Thorsten Buzug

Date of oral examination: 26.10.2023

Approved for printing: Lübeck, 10.11.2023

Abbreviation Index

AMD *Age-Related Macular Degeneration*
AOM *Acousto Optic Modulator*
APD Avalanche Photodiode
BCVA *best corrected visual acuity*
CSCR *Central Serious Chorio-Retinopathy*
CV Cross Validation
cw Contious Wave
DME *Diabetic Macula Edema*
DR *Diabetic Retinopathy*
ED *Effective Dose*
ETDRS *Early Treatment in Diabetic Retinopathy Study*
FA *Fluorescein Angiography*
GCL *Ganglion Cell Layer*
HE *Hematoxyl and Eosin*
HeNe *Helium Neon*
HSP *Heat-Shock Protein*
ILM *Inner Limiting Membrane*
INL *Inner Nuclear Layer*
IPL *Inner Plexiform Layer*
IS\OS *Inner-Segment/Outer-Segment Junction*
laser *light amplification by stimulated emission of radiation*
MMP2 *Matrix Metalloproteinase 2*
NA *Numeric Aperture*
NFL *Nerve Fiber Layer*
OA *Opto-Acoustic*
OCT *Optical Coherence Tomography*
OLM *Outer Limiting Membrane*
ONL *Outer Nuclear Layer*
OPL *Outer Plexiform Layer*
pDR *Proliferative Diabetic Retinopathy*
PDT *Photodynamic Therapy*
PED *Retinal Pigment Epithelium Detachment*
PEGF *Pigment Epithelial-Derived Growth Factors*
PRP *Pan-Retinal Photocoagulation*
RMS *Root Mean Square*
VEGF *Vascular Endothelial Growth-Factors*

1 Introduction

1.1 Selective Retina Therapy

The effect of retinal intense light irradiation (photocoagulation) first gained attention in the late 19th century.[1, 2] In 1949, Meyer Schwickerath applied sunlight to treat retinal detachments.[3] This approach enabled a non-invasive treatment of the retina for the first time. The success of this approach led to the development of a Xenon lamp-based coagulator.[4] In the 1960s, the effect of light amplification by stimulated emission of radiation (laser), as predicted by Schawlow and Townes,[5] became technically possible.[6] In order to study potential hazards and benefits of ruby lasers, experimental treatments on rabbit eyes were performed.[7] First clinical applications as an alternative light source for photocoagulation were performed a few years later.[8, 9] The smaller spot size of a ruby laser beam, compared to a Xenon lamp, permitted a more precise treatment. To further reduce the spatial extent of the damaged volume, by a reduction of penetration depth, laser light with a higher absorption in the targeted tissue was used. These argon lasers emit light at 488 nm and 515 nm. Later, the invention of frequency-doubled solid-state lasers (532 nm) led to the development of much smaller laser devices that could deliver a more stable output power. From this point, disease- and treatment-specific irradiation parameters have been the main focus of studies on retinal laser treatment. One important parameter was the irradiation time which has been lowered from formerly 200ms to less than 50ms in the recent decades.

The main light absorbing layers are the Retinal Pigment Epithelium (RPE) and the choroid. Around 50% of the light entering the eye is absorbed by the RPE. [10] With around 4µm the pigmented part of the RPE is smaller the choroid with about $270\mu m$. Thus, heat generation due to laser light absorption induces peak temperatures in the RPE-cells which are directly attached to the photoreceptors. Heat flows from the RPE in the neighboring regions due to heat conduction. Heat convection does not affect the temperatures to a significant amount in the µs and ms time regime. [11]

While a successful treatment of some diseases may require affecting the photoreceptors, a successful treatment of other diseases, like diabetic macula edema (DME) or central serous retinopathy (CSCR), seems to depend on the healing effects of the main light absorbing cell layer, the retinal pigment epithelium (RPE)[12-14] [15, 16], which is located

just behind the photoreceptors. In the laser treatment of CSCR and DME, any damage of everything but the RPE cells is collateral damage.

To limit the induced damage to the RPE, the principle of selective photo-thermolysis can be used.[17, 18] This is a method which makes use of short irradiation times to confine the laser induced heat within an absorbing layer in a less absorbing surrounding within the time of irradiation.

For repetitive irradiation and a micrometer sized layer like the RPE, numerical calculations have already found pulse durations of 5 µs to be suitable to confine heat in the RPE, called "micro-coagulation" or "selective coagulation". [19] Histological examinations supported this principle. [20, 21]

However, the observed threshold for cell damage resulting from the application of the microsecond laser pulses has contradicted the predictions obtained by application of cell damage models, which assumed only thermal effects (Arrhenius damage models).[22]

In search of the root cause of this contradiction, other cell damage mechanisms were needed to be considered as well. Further research on this topic has found that the local temperature of the intracellular melanosomes can lead to vaporization of cell liquid and consequently, microbubble formation within the cell.[23]

High speed photography was used to document how micrometer sized bubbles (microbubbles) disrupt RPE cells [24]. Those bubbles can grow from the size of several nanometers to several micrometers. It has been found that the relationship between bubble lifetime and maximum bubble diameter can be described by the Rayleigh Plesset equation [25] (chapter 2.4.2).

The shorter the pulse duration the less time there is for protein denaturation to take place. The minimum radiant exposure required to induce RPE cell damage can be lower than the minimum radiant exposure required for denaturation-based cell damage.[26, 27] At a pulse duration of 1.7µs the laser induced heat can suffice to vaporize cell liquid before protein denaturation accumulates to a degree which is deadly for the cell. At the beginning of this work, it was thought that microbubble formation may also be the initial cell damage mechanism at 5µs.[28] Within this work this hypothesis was rejected.

In a clinical treatment scenario, selective RPE damage is impossible to achieve reproducibly since, in contrast to conventions laser induced lesions, selective RPE lesions

are not visible during treatment.[21] Variations in transparency of anterior eye media (cornea and lens) and variations in RPE and choroidal pigmentation make it impossible to operate with a constant laser pulse energy. [29, 30] This makes it necessary to adapt the laser power during treatment. Otherwise, a therapeutical effect may not be induced in the case of under pigmentation (undertreatment) or collateral damage may be induced by heating the photoreceptors too much due to heat flow (over-treatment).

A treatment protocol for safe and effective selective treatment should include a) titration spots in the periphery, b) an eye-individual pulse energy threshold derived from this titration spots, and c) a diagnostic procedure to confirm RPE damage directly after the irradiation process. The preferred diagnostic technique to identify RPE damage is fluorescein angiography (FA). However, FA cannot distinguish between RPE pathology and laser treatment induced RPE effects. By this reason it can only offer information about cell damage in non-symptomatic regions. SRT is usually applied inside or very close to symptomatic regions FA is not suitable for dosimetry. This alone makes FA not suitable to test for selective RPE damage after laser irradiation.

It was investigated in preclinical studies whether the pulse energy range to achieve a selective RPE lesions can be discriminated from the pulse energy range where even pulsed laser systems cause an ophthalmoscopically visible lesion. The radiant exposure required to achieve a 50% chance of FA identifiable RPE lesions in rabbits can be exceeded by around a factor of 2 until ophthalmoscopically visible spots can be found.[31] A clinical treatment procedure based on this therapeutic window never established.

Since microbubbles are the origin of cell damage, a microbubble formation (MBF) detection technique could be used to predict whether cell damage was induced after an irradiation. This information about the presence or absence of MBF could be used by a clinician (or the laser system) to actively adapt the laser power during treatment. Hence, techniques to detect microbubbles become necessary for use in a practical clinical routine.

Several optical and acoustical techniques have been developed to detect microbubbles. The first acoustical feedback techniques required a series of pulses of the same energy to detect microbubbles.[32] Since the laser pulse energy to induce selective RPE damage varies intra and inter-individually, such a microbubble detection technique is best applied in a treatment protocol which requires the clinician to start with a very low pulse energy,

always. Then the laser pulse energy can be increased with every irradiation of the same region, until MBF can be identified. This procedure is still too time intensive. A system which can perform this treatment protocol autonomously is desirable. But this requires microbubble detection techniques which can identify microbubble during laser irradiation. Ideally microbubble formation should be identifiable during/after the irradiation with a single pulse.

In this work multiple novel approaches (optical and optoacoustical), solely using treatment laser irradiation and no other laser sources, were developed and utilized to detect microbubble formation after individual irradiations. These approaches to detect MBF were utilized during a series of laser pulses with pulse-wise increasing laser pulse energy (ramp-mode). The laser irradiation is intended to be ceased if MBF is detected.

1.2 Kurz-Zusammenfassungen

1.2.1 Studie 1 Grenzwerte (Ex-vivo, 19 Proben und In-vivo, 11 Tiere)

Motivation: Der bei Laserbestrahlung eintretende initiale Zellschadensmechanismus ändert sich im unteren Mikrosekundenbereich von einem rein thermo-mechanischen Effekt (Mikroblasenbildung, MBF) hin zu einem rein thermischen Effekt (Proteindenaturierung). Um die Detektion von Mikroblasen als Indikator für RPE-Zellschädigung verwenden zu können, muss die Mikroblasenbildung auch die initiale Ursache für Zellschädigung sein. Neuartige Hochleistungs-Diodenlasersysteme sind in der Lage die Pulse mit variable einstellbaren Pulsdauern zu erzeugen. Es ist das Ziel dieser Studie die Grenzwerte für Mikroblasenbildung und RPE Zellschaden in vivo und ex vivo zu ermitteln (Kapitel 2.6.4).

Methoden: Ein Diodenlasersystem (A.R.C Laser Systems, Nürnberg, Germany) mit einer Wellenlänge von 514nm, einer Leistung von 15W und einer variablen Pulsdauer von 2 µs bis 50 µs wurde verwendet (Kapitel 3.2). Organ Explantate von enukleierten Schweineaugen und Augen von Chinchilla Bastard Kaninchen wurden bestrahlt um die Grenzwerte der Bestrahlungsstärke $H\ [mJ/cm^2]$ für RPE Zellschädigung ($\overline{H}_{cell}$) mittels Calcein Vitalitäts assays und Fluorescein Angiographie zu ermitteln. Der Grenzwert für Mikroblasenbildung ($\overline{H}_{MBF}$) wurde optoakustisch ermittelt.

Ergebnisse: Ex-vivo und in-vivo lag $\overline{H}_{MBF}$ bei Pulsdauern $\geq 5\ \mu s$ oberhalb von $\overline{H}_{cell}$ ($p < 0.05$). Bei einer Puls-Dauer von 2 µs konnte kein statistisch signifikanter Unterschied der beiden Grenzwerte festgestellt werden. Der Abstand von $\overline{H}_{MBF}$ zu $\overline{H}_{cell}$ erhöht sich mit zunehmender Pulsdauer von 1.07 auf 1.48 (ex-vivo, Kapitel 4.1, Figure 48) und von 1.1 auf 1.6 (in-vivo; siehe Kapitel 4.1, Figure 50).

Schlussfolgerung: Die Ergebnisse deuten darauf hin, dass Mikroblasenbildung bei einer Pulsdauer von 2 µs der initiale Zellschadensmechanismus ist. Bei Pulsdauern von 5 µs und längsr ist ein rein thermischer Zellschadens-Mechanismus die initiale Ursache für RPE-Zelltod. Folglich soll in den folgenden SRT-Studien mit einer Pulsdauer $\leq 2\ \mu s$ gearbeitet werden (siehe Kapitel 5.1).

1.2.2 Studie 2 Simulation optischer Mikroblasendetektion

Motivation: Der Brechungsindex von Mikroblasen ($n_{Bubble} = 1$) unterscheidet sich von dem der Zellflüssigkeit ($n_{Liq} = 1.3$). Mit einem Durchmesser im unteren Mikrometerbereich macht dies eine Mikroblase zu einem optisch streuenden Objekt, welches durch Mie-Streuung beschrieben werden kann (Kapitel 2.7.1). Jedoch kann Mie-Streuung allein nicht alle in Experimenten beobachteten Phänomene erklären. Es ist das Ziel dieser Studie, die Einflüsse von Mikroblasen, optischen Design-Parameter, und zufälligen Start-Voraussetzungen zu simulieren und deren Bedeutung für die Mikroblasendetektion zu bewerten.

Methoden: Mikroblasenwachstum wurde mittels der Rayleigh Plesset Gleichung in Schritten von 1 ns berechnet (Kapitel 2.4.2). Für jede Mikroblasengröße wurde die Nahfeldlösung der Mie-Gleichung berechnet (Kapitel 2.7.1.2). Zusammen mit zufälligen Start-Werten ergeben sich mit der Nahfeldlösung die Amplituden und Phasen, welche das optische Feld in der Objektebene beschreiben. Abbildungs-Gleichungen für kohärente Strahlung wurden verwendet, um die Objektebene in die Bildebene abzubilden (Kapitel 2.7.2). Ein Orts-Integral über die Sensorfläche ergibt ein Spannungs-Äquivalent der einer Photodiode.

Ergebnisse: Es konnte beobachtet werden, dass unter der Abwesenheit von Mikroblasenbildung der zeitliche Verlauf des von der Photodiode erfassten Lichtes dem des applizierten Laserpulses in abgeschwächter Form gleicht. Unter Anwesenheit einer Mikroblase wurde das zurückgestreute Licht moduliert. Je größer die Mikroblase je größer die Modulationen (Kapitel 4.2.1, Figure 52). Es konnte weiterhin beobachtet werden, dass eine Zunahme im Durchmesser der Apertur-Blende des optischen Systems sowie eine Zunahme in dem Durchmesser der bestrahlten Fläche (Spot) die Modulationen verringern (Kapitel 4.2.2, Figure 53). Unterschiede in den Start-Variablen von Amplitude und Phase führten zu unterschiedlichen maximalen Leistungen (Kapitel 4.2.3, Figure 54 und Figure 55) und zu unterschiedlichen zeitlichen Verläufen und Ausprägungen der Mikroblasen-induzierten Modulation im aufgezeichnetem Signal (Kapitel 4.2.2, Figure 53). Des Weiteren zeigen die Ergebnisse, dass Unterschiede im Strahlprofiel (der örtlichen Verteilung der Laser-Energie innerhalb der bestrahlten Fläche) die Gesamtamplitude und Modulations-Verlauf ebenfalls beeinflussen (Kapitel 4.2.4, Figure 56).

Schlussfolgerung: Das vorgestellte wellenoptische Modell konnte dazu verwendet werden, Signaleigenschaften zu simulieren, welche mit klassischer Mie-Theorie allein

nicht beschrieben werden konnten. Dies beinhaltet die Abhängigkeit der Gesamtamplitude von den zufälligen Start-Werten von Amplitude und Phase in der Objektebene (Kapitel 5.3.1). Obwohl gezeigt werden konnte, dass Modulationen im aufgezeichneten Signal mit dem Maximal-Radius der Mikroblase ansteigen, ist es aufgrund dieser Zufallseinflüsse leider nicht möglich aus den Modulationen einen Rückschluss auf die Mikroblasengröße zu ziehen. Ein Algorithmus zur Auswertung der von Mikroblasen erzeugten Signalen kann es daher nur leisten, eine binäre Klassifizierung über das Vorhandensein von Mikroblasen vorzunehmen.

1.2.3 Studie 3 Automatisierte SRT (In-Vivo, 10 Tiere)

Motivation: Zu Beginn der Studie existierten noch keine Erfahrung über die Auswirkungen von möglichen Störeinflüssen wie Bewegungen durch Atmung, Herzschlag, Nystagmus, etc. auf die optische Mikroblasenerkennung. Es war daher das Ziel dieser Studie zu testen ob automatische Abschaltungen der Laserbestrahlung bei dem Auftauchen von Mikroblasen in-vivo möglich sind.

Methoden: Ein frequenzverdoppelter Nd:YLF Laser (527 nm) mit einer Pulsdauer von 1.7 µs und einer Repetitionsrate von 100 Hz wurde als Lichtquelle verwendet. Die Laserpulse Energie jedes Pulses wurde durch einen akusto-optischen Modulator (AOM) über eine maximale Gesamtzahl von 30 Pulsen von 10% auf 100% einer zuvor gewählten Maximal-Energie erhöht und bei dem Erkennen einer Mikroblase unterbrochen. Zurückgestreutes Licht von dem 132µm großen Spot auf der Netzhaut wurde über einen 80/20 Strahlteiler in einen Observations-Pfad geleitet. Dieser führt zu einer Avalanche-Photodiode (Kapitel 3.3.1). Kaninchen mit einem Minimalgewicht von 2.9kg wurden bestrahlt (Kapitel 3.6.1). Zellschädigung wurde mittels Fluorescein Angiographie nachgewiesen (Kapitel 3.7.3). Schnittbilder des bestrahlten Bereichs via optischer Kohärenztomographie und Histologischer Schnitte wurden verwendet, um auf Selektivität der Zellschädigung zu testen (Kapitel 3.7.4).

Ergebnisse: Einige Ergebnisse der Simulationen konnten durch die Experimente gestützt werden. Einschließlich der zufällig variierenden maximalen Energie des zurückgestreuten Lichtes (Kapitel 4.3.1, Figure 57 bis Figure 60). Es konnte durch Fluorescein Angiographie gezeigt werden, dass automatische Abschaltungen an einem Punkt stattfanden, an welchem Zellschaden verursacht wurde (Kapitel 4.3.3, Figure 64). Die Mikroblasenerkennung funktionierte jedoch nicht optimal. Ein systematischer Fehler, welcher dann auftrat, wenn Mikroblasenbildung schon bei dem ersten Puls erzeugt

wurde, konnte identifiziert werden. Trotz nicht perfekter automatischer Unterbrechungen der Bestrahlungen, konnten OCT- und Histologie Schnitte eine nahezu normale Morphologie nachweisen (Kapitel 4.3.4, Figure 66 und Figure 67). Der einzige Unterschied zu einer völlig normalen Morphologie bestand darin, dass es vereinzelt zu einem Übereinander-wachsen von RPE Zellen kam (Kapitel 4.3.4).

Schlussfolgerung: Automatisches Unterbrechen der Laserbestrahlung kann dazu verwendet werden selektive RPE Schäden zu erzeugen. Verbesserungen an dem Algorithmus der Blasenerkennung waren noch notwendig (Kapitel 5.4.3, Figure 67).

1.2.4 Studie 4 Optische Mikroblasendetektion (Klinische Studie, 15 Patienten)

Motivation: Während gezeigt werden konnte, dass optische Mikroblasenerkennung und die damit verbundenen automatische Abschaltung in gesunden jungen Kaninchenaugen funktionierte, blieb die Frage, ob diese Technologie auch in klinischen Situationen beständig funktionieren kann. Es war das Ziel dieser Studie, auf Basis von klinischen Daten einen Algorithmus zu entwickeln, welcher unter klinischen Bedingungen Mikroblasen erkennen kann.

Methoden: Ein Laser mit einer Wellenlänge von 527 nm und einer Repetitionsrate von 100 Hz und einer Pulsdauer von 1.7 µs wurde angewandt. Es wurden maximal 15 Pulse aufsteigender Energie appliziert. Die Pulsenergie erhöhte sich von 50 % auf 100 % einer zuvor eingestellten Maximalenergie. Zurückgestreutes Licht wurde auf eine Photodiode geleitet. Die digitalisierte Spannung der Photodiode diente als Eingangs-Signal für den zu entwickelnden Algorithmus (Kapitel 3.3.2). Sensitivität und Spezifität waren die Messgrößen, welche im Zuge der Algorithmus-Entwicklung maximiert wurden (Kapitel 3.10.1).

Ergebnisse: Elf Patienten mit zentral seröser Retinopathie und vier Patienten mit Diabetischem Makulaödem wurden behandelt. Insgesamt standen 4626 Pulse für die Entwicklung und Tests zur Verfügung. Bei dem Grenzwert, welcher zu der geringsten Anzahl an falschen Entscheidungen führt, wurde eine Sensitivität von 1 und eine Spezifität von 0.93 in dem mit Zellschädigung gelabelten test-Datensatz erreicht. Differenzen zu zwei weiteren Datensätzen, welche zur Entwicklung und Validierung verwendet wurden, betrugen 0.03 und 0.05 (Kapitel 4.4.1, Figure 71).

Schlussfolgerung: Trotz großer intra-individueller Unterschiede in den Grenzwerten für Mikroblasenbildung können die entwickelten Algorithmen dazu eingesetzt werden, mittels der erfassten Photodioden-Signale, Zellschädigung vorherzusagen (Kapitel 5.5).

1.2.5 Studie 5: (Opto-) Akustische Mikroblasendetektion (Klinische Studie, 15 Patienten)

Motivation: Während die optischen Eigenschaften der vorderen Augenmedien bei der Erfassung zurückgestreuten Lichtes Probleme verursachen können (z.B. Katarakt), ist dies für akustische Wellen nicht der Fall. Das schnelle ausdehnen und/oder zusammenziehen eines Objektes kann eine Druckwelle auslösen, welche an der Augen-Oberfläche sensorisch erfasst werden kann. Bei dem Objekt kann es sich um eine Mikroblase oder um sich thermisch ausdehnendes Gewebe handeln (Kapitel 2.4.3). Druck-Transienten von Mikroblasen unterschieden sich von thermoelastischen Signalquellen in a) Ihrer Druckamplitude (Kapitel 2.6.2), b) dem Verlust der Zeitinvarianz (Kapitel 2.6.3) und c) in dem Zeitpunkt ihres Auftretens (Kapitel 2.6.4). Folglich können auch opto-akustische Signale zur Mikroblasendetektion verwendet werden. Es ist das Ziel dieser Studie, mittels klinischer Daten, ein opto-akustisches Verfahren zu entwickeln, welches zur Vorhersage von selektiver RPE-Zellschädigung eingesetzt werden kann.

Methoden: Die Daten wurden simultan mit den optischen Daten aus Studie 4 erfasst. Der Sensor, welcher die opto-akustischen Signale erfasst, war in das Kontaktglas eingebaut. Das Signal wurde um 64dB verstärkt und mit 100MS/s digitalisiert. Die digitalisierte Spannung wurde als Eingangs-Signal für die Algorithmen verwendet (Kapitel 3.3.2). Der erste Optoakustik-Algorithmus verwendet den nichtlinearen Druck-Anstieg im Falle einer Mikroblasen-Bildung als Indikator (NL-Algorithmus, Kapitel 2.6.2). Der zweite Optoakustik-Algorithmus identifiziert die unterschiedlichen zeitlichen Verläufe der Drucktransienten im Falle der Mikroblasenbildung (TV-Algorithmus, 2.6.3). Beide Algorithmen werden gegen ein Baseline Modell getestet, welches lediglich die Gesamtamplitude auswertet (BL-Algorithmus; Kapitel 3.3.2.4).

Ergebnisse: Insgesamt wurden 4646 Drucktransienten für Entwicklung und Tests verwendet. Die Entwickelten Algorithmen waren dem Baseline Model überlegen (Kapitel 4.5, Figure 75). Die Algorithmen wurden an mit Zellschädigungs-informationen gelabelten Datensätzen getestet, welche nicht für die Entwicklung verwendet wurden. An dem

Grenzwert, welcher zu geringsten Anzahl falscher Entscheidungen führt, weist der NL Algorithmus eine Sensitivität von 0.96 und eine Spezifität von 0.97 auf (Kapitel 4.6.1, Figure 79). An dem Grenzwert welcher zu geringsten Anzahl falscher Entscheidungen führt, weißt der TV Algorithmus eine Sensitivität von 0.96 und eine Spezifität von 0.96 auf (Kapitel 4.6.2, and Figure 80)

Schlussfolgerung: Trotz großer intra-individueller Unterschiede in den Grenzwerten für Mikroblasenbildung können die NL- und TV-Algorithmen dazu eingesetzt werden, mittels der erfassten Drucktransienten Zellschädigung vorherzusagen (Kapitel 5.6). Der Nachteil Verfahrens ist, das immer ein Referenz Transient verfügbar sein muss. Bei dem NL-Algorithmus muss dieser Referenz-Transient rein thermoelastischen Ursprungs sein.

1.3 Abstracts

1.3.1 Study 1: Thresholds (ex-vivo, 19 specimens and in-vivo 11 rabbits)

Motivation: The initial cause for RPE cell death changes with the pulse duration if the lower µs time regime from thermomechanical mechanism (Microbubble Formation, MBF) to thermal mechanism like protein denaturation. Microbubble detection can only be used as a predictor of RPE cell death when Microbubble formation is the initial cause of RPE cell death. Novel high power laser diode systems can generate laser pulses over a wide range of pulse durations. It is the purpose of this study to identify the thresholds for microbubble formation and RPE cell damage ex vivo and in-vivo (chapter 2.6.4).

Methods: Diode laser (A.R.C Laser Systems, Nürnberg, Germany) with a wavelength of $514\ nm$, a power of $15\ W$ and pulse durations between 2 and $50\ \mu s$ was used (Chapter 3.2). Porcine RPE-choroidal explants (ex vivo) and chinchilla bastard rabbits (in vivo) were irradiated to determine threshold radiant exposures for RPE damage $\overline{H}_{cell}$ by calcein vitality staining (chapter 3.7.1) and fluorescence angiography (chapter 3.7.2), respectively. Thresholds for micro-bubble formation (MBF) $\overline{H}_{\mathrm{MBF}}$ were evaluated by time resolved opto-acoustic microbubble detection (chapter 3.8.1).

Results: $\overline{H}_{\mathrm{MBF}}$ is higher than $\overline{H}_{\mathrm{Cell}}$ at pulse durations $\geq 5\ \mu s$ ($p < 0.05$) ex vivo, while at $2\ \mu s$ no statistically significant difference was found. The ratio between $\overline{H}_{\mathrm{MBF}}$ and $\overline{H}_{\mathrm{cell}}$ increases with pulse duration from 1.07 to 1.48 and 1.1 to 1.6 ex vivo and in vivo, respectively. (Chapter 4.1, Figure 48 and Figure 50)

Conclusion: The results suggest that MBF can be the initial cause of cell damage at pulse durations of $2\ \mu s$ and shorter. Furthermore, the results suggest that at $5\ \mu s$ and longer thermal denaturation is the initial cause of cell damage. Laser pulses with a duration of $1.7\ \mu s$ were used in studies where microbubble formation is required to be the initial cell damage mechanism (chapter 5.1).

1.3.2 Study 2: Simulation of optical microbubble detection

Motivation: Microbubbles have a different refractive index ($n_{Bubble} = 1$) than the surrounding cell liquid ($n_{Liq} = 1.3$). Together with their size in the lower micrometer regime, this makes them optically scattering objects (chapter 2.7.1). However, scattering alone does not explain all phenomena which were observed during measurements. It is the purpose of this study to evaluate influences on the optical signal like microbubble growth, optic design, randomly valued wave-optical properties.

Methods: Bubble growth was simulated by solving the Rayleigh Plesset equation (chapter 2.4.2) for time steps of 1 ns. For each time step the nearfield solution of the Mie scattering equations was calculated (chapter 2.7.1.2). Together with initial random values, the nearfield solution describes the amplitude and phase of the object plane. Coherent imaging equations were applied to propagate the object plane to the image plane (chapter 2.7.2). A spatial integral of the intensity profile in the object plane then gives a voltage-equivalent at the photodiode (chapter 3.1.2).

Results: It was observed that, under stable conditions, without microbubble formation, photodiode signals show the same time-evolution as the applied laser pulse. In the case of microbubble formation, the backscattered light was modulated. The larger the microbubble, the larger the modulations of the signal received by the photodiode. (chapter 4.2.1, Figure 52) It was observed that an increasing spot size or the diameter of the aperture stop, decreases the modulation amplitude. (chapter 4.2.2, Figure 53) Differing initial values for amplitude and phase result in differing maximum laser power received by the photodiode. (chapter 4.2.3, Figure 54 and Figure 55) as well as differences in the time evolution of the modulations. Simulations also suggest that variations in the beam profile have a significant influence on the sensor signals as well (chapter 4.2.4, Figure 56).

Conclusions: The wave optical model could be used to simulate signal characteristics which cannot be explained with Mie theory alone. Most importantly, the dependence of

the maximum power received by the photodiode (modulation free scenario) on the random amplitude and phase values in the object plane (chapter 5.3.1).

Although the model suggests that increasing microbubble diameter led to higher modulations, it is not possible to draw conclusions on the bubble diameter since randomly valued amplitude and phase of the optical field in the object plane cannot be known. (chapter 5.3.2) Consequently, the algorithms for microbubble detection, needed to be designed to make binary decision whether a microbubble formation took place or not.

1.3.3 Study 3: Automated SRT (in vivo, 10 rabbits)

Motivation: At the beginning of this study there was no experience of optical microbubble detection in vivo. It has been expected that eye movements can influence the signal. Movements may originate from blood flow, changes in blood pressure (systolic - diastolic), breathing, etc. It was the purpose of this study to evaluate whether automatic SRT can be performed in vivo.

Methods: A frequency doubled Nd:YLF laser ($527\ nm$) with a pulse duration of $1.7\ \mu s$ and a repetition rate of $100\ Hz$ was used as light source. Pulse wise changes in laser pulse energy was realized by an acusto-optic modulator (AOM). Light was guided to a slit-lamp via an optical fiber with a core diameter of $50\ \mu m$ and a numerical aperture of 0.11. The light was imaged into an intermediate image plane with a magnification factor of 4. Hence the diameter of the illuminated area is increased to $200\ \mu m$. The intermediate image please is then imaged to the fundus by a Mainster contact lens.(chapter 3.4.4) Due to the anatomic properties of the rabbit eye the magnification factor of this second imaging process is around 0.66.(chapter 3.4.3) Hence, the spot diameter on the RPE is around $132\ \mu m$. A fraction of the backscattered light from this irradiated area was guided to an observation path by an 80/20 beam splitter. The light passes an aperture stop with a diameter of 1mm and enters a fiber with a core diameter of $50\ \mu m$ and a numerical aperture of 0.11. The fiber leads to an avalanche photodiode with an active area of $1\ mm\ x\ 1\ mm$. All the light of the fiber is captured by the photodiode. (chapter 3.3.1)

In the experiments rabbits with an average weight of $2.9\ kg$ were used for irradiation. A pattern of irradiations with and without automatic irradiation ceasing was applied.(chapter 3.6.1) To test whether the automatic irradiation ceasing was performed at a pulse energy sufficient to induce cell damage, another diagnostic technique (fluorescein angiography, FA) was applied. (chapter 3.7.3) To test whether automatic

irradiation ceasing was performed at a point where no collateral cell damage was induced, optical coherence tomography and histology (HE staining) was applied.(chapter 3.7.4)

Results: Some predictions made by the simulations have been supported by the results of the experiments. Most importantly, random pulse-wise and spot-wise changes in received (backscattered) laser pulse energy (chapter 4.3.1, Figure 57 to Figure 60). Comparisons with fluorescein angiography have shown that automatic irradiation ceasing was executed at a point where cell damage was induced (chapter 4.3.3, Figure 64). However, Microbubble identification did not work perfectly. A systematic error which occurs when the first backscattered pulse was not below microbubble formation threshold was identified. Additional tests (OCT, HE staining) have shown an intact morphology (chapter 4.3.4 Figure 66 and Figure 67). However, it has been observed that the RPE-cells tended to overgrow each other instead of forming a new monolayer (chapter 4.3.4).

Conclusion: Automatic irradiation ceasing based of optical microbubble detection can be used to induce selective RPE lesions. (chapter 5.4.4) Improvements of the optical microbubble detection algorithm were necessary (chapter 5.4.3, Figure 67).

1.3.4 Study 4: Optical microbubble detection (clinical study, 15 patients)

Motivation: While it has been shown in healthy young rabbit eyes that automatic ceasing can induce selective cell damage, the question remains whether this can be reliably achieved in diseased human eyes. It is the purpose of this study to develop an algorithm which can be applied for automatic irradiation ceasing in the case of initial microbubble formation.

Methods: A laser with a wavelength of $527\ nm$, a Repetition Rate of $100\ Hz$, and a pules duration of $1.7\ \mu s$ was applied. This laser system applied 15 pulses at most, in each irradiation. Like in the previous system, backscattered light was guided to a photodiode. The digitized voltage of the photodiode delivered the input for the algorithm for microbubble detection (chapter 3.3.2). Sensitivity and specificity were the metrics maximized through an automatic optimization process (chapter 3.10.1). Cell damage was verified by fluorescein angiography. (FA, chapter 3.7.3)

Results: Eleven patients with central serous chorioretinopathy and four with diabetic macula edema were treated. Overall, 4626 pulses were used for algorithm parameter

optimization and testing. At a threshold which leads to the least amount of false decisions overall, a sensitivity of 1 and a specificity of 0.93 was achieved in the FA labeled test set. The difference to the sensitivity and specificity evaluated with the development set was of 0.03 and 0.05, respectively (chapter 4.4.1, Figure 71).

It was observed that the threshold pulse energy for microbubble formation can vary up to a factor of 4.4 from a non-diseased region in the periphery to a region with pathological symptoms in the center (chapter 4.4.2).

Conclusion: Despite the high intra-individual differences in microbubble formation thresholds, the algorithm for optical microbubble detection can be applied to predict cell damage (chapter 5.5).

1.3.5 Study 5: Optoacoustic microbubble detection (clinical study, 15 patients)

Motivation: While the optical conditions of the anterior eye media (e.g. cataract) can cause difficulties to the optical microbubble detection technique, an ultrasonic waves are not influenced by the optical properties. In optoacoustics, rapid expansion and/or collapse of an object, induces a pressure wave which can be detected. The object may be heated tissue or a microbubble (chapter 2.4.3). Pressure transients of microbubbles differ from thermoelastic pressure transients in a) pressure amplitude (nonlinear increase with respect to pulse energy; chapter 2.6.2), b) time-invariance (loss of time invariance in the case of microbubble formation; chapter 2.6.3), and c) time of occurrence (occurs during laser irradiation; chapter 2.6.4). Thus, pressure transients can be used for microbubble prediction. It is the purpose of this study to develop and evaluate algorithms which uses digitized pressure transients for microbubble/cell damage prediction.

Methods: The data was acquired in the same study as the optical data for microbubble detection. The sensor to detect the ultrasonic pressure waves was a ting transducer which was embedded in a contact lens. The sensor voltage was amplified by $64\ dB$ and digitized ($100\ MS/s$). The digitized voltage was then used as input for algorithms for microbubble prediction (chapter 3.3.2). The first algorithm makes use of the nonlinear pressure increase with respect to laser pulse energy (NL-Algorithm; chapter 2.6.2). The second algorithm makes use of the fact the consecutive pressure transients differ in time evolution when microbubble formation takes place (TV-algorithm, 2.6.3). Both algorithms were compared to a baseline model (BL-algorithm; chapter 3.3.2.4).

Results: Overall, 4646 pressure transients were used for algorithm optimization and testing. The tested algorithms were superior to a baseline model (chapter 4.5, Figure 75).

For the NL-algorithm, at a threshold which leads to the least amount of false decisions, a sensitivity of 0.96 and a specificity of 0.97 was achieved in a dataset which was not used in the development process (chapter 4.6.1, Figure 79).

For the TV-algorithm, at a threshold which leads to the least amount of false decisions, a sensitivity of 0.96 and a specificity of 0.96 was achieved in a dataset which was not used in the development process (chapter 4.6.2, and Figure 80).

Conclusions: Despite the high intra-individual difference in microbubble formation thresholds, the NL and TV algorithms for microbubble detection can be applied to predict cell damage (chapter 5.6). The drawback of the optoacoustic techniques for microbubble detection is that they always need a refence transient. The reference transient of the NL Algorithm needs to originate from thermoelastic origins only (no microbubble formation). It is not possible to draw conclusions about microbubble formation, at the threshold of microbubble formation, from one single transient.

2 Fundamentals

2.1 The anterior eye media

The axial length of the human eye vary from 23.14 mm to 24.08 mm [33] The cornea, anterior chamber, iris, lens, and vitreous influence the imaging process of an object onto the retina. Figure 1 displays the mentioned eye-media. Parameters like the radii of cornea and lens, and asphericity can influence the imaging quality. The parameters that mark a healthy adult human eye can be found in the literature.[33-37]

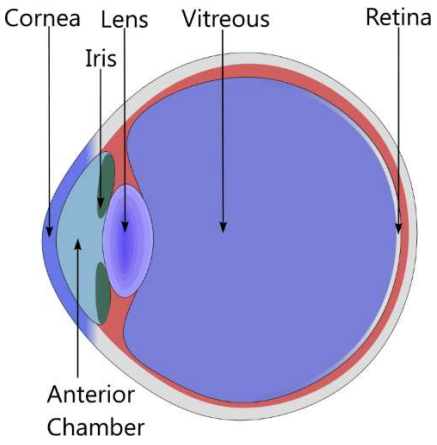

Figure 1. Optical media of the eye. In this work a light absorbing monocellular layer right below the retina is treated. Anterior eye media (cornea, lens, vitreous) change in transparency with age and disease. The light absorbing retinal pigment epithelium is directly attached to the retina.

Several parameters such as the anterior and posterior corneal radii, asphericity, and transparency change over the course of one's lifetime. "On average, the cornea becomes more spherical with age and, as a consequence, spherical aberrations tend to increase."[38] The transparency of the anterior eye media reduces with age. Light which is not absorbed or scattered back can be considered as transmitted. This can also include forward scattered light. In the context of laser treatment non scattered light is of importance. Thus, it shall be distinguished between total and direct transmission. The term "total transmission" refers to all the transmitted light, including the light scattered by the ocular media. The term "direct transmission" refers to the non-scattered proportion of the transmitted light. The direct transmittance of a young lens (4.5 years old) at 700 nm has been measured with around 88 % of the laser power applied to the eye, the transmittance of an old lens (75 years old) has been measured with around 41 %. [29] Figure 2 displays the spectra for total and direct transmission.

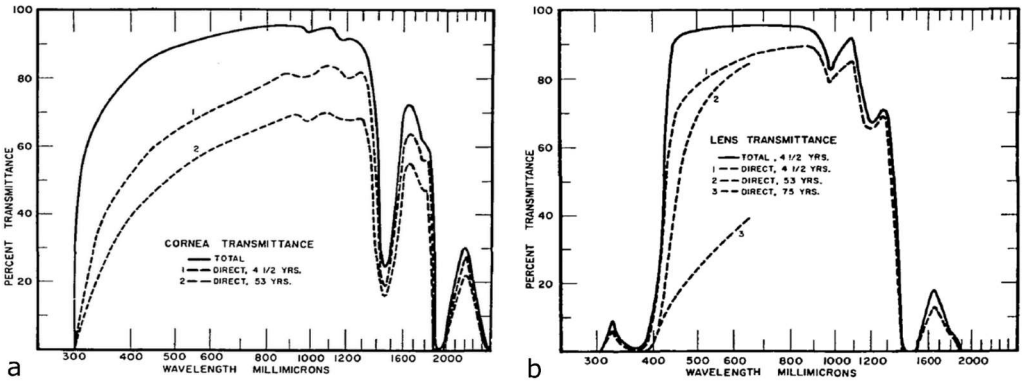

Figure 2. a) Total transmittance (including the light scattered by the anterior media and b) direct transmittance (light that does not change its direction) of the ocular media.[29] It can be seen that the transmission of the anterior eye media of a child is higher than those of a 53 or 75 year old human.

2.2 The fundus of the eye

2.2.1 Morphology of the neural retina

The inside, back surface of the eye (fundus oculi) consists of several layers orthogonal to the direction of light propagation through those layers. Figure 3a displays a sketch of the most important cell types of the fundus. In the following paragraphs the different cell types and its layers are presented. Different imaging technologies have different spatial resolutions. While microscopy images of dead tissue can display individual cells, OCT B-Scans, which can be done in a living patient, can show layers of varying scattering properties, but with lower resolution than a microscope. Hence, the differentiable retail layers depend on the imaging technology. In this work Images of the retinal layers were acquired by OCT and microscopic images with hematoxylin and eosin (H&E) staining were used. An example of an H&E stained sample is shown in Figure 3b. Details about the staining method are discussed in the materials and methods section (chapter 3.7.4).

Cross-section images obtained through OCT can be used to image the retina. In OCT images the backscattered light of each layer is displayed. Figure 3c shows an OCT image of a heathy human retina. In the following sentences a description of each layer can be found. The first inner retinal layer is the inner limiting membrane (ILM). The ILM's thickness ranges from 70nm (foveal region) to 400nm (equatorial region). It is composed of "plasma membranes of glial cells, basement membranes of glial cells, and the vitreous cortex with its fibrils."[39] This layer is followed by the nerve fiber layer (NFL; Figure 3a gray), which is composed of the axons of the ganglion cell layer (GCL, Figure 3a pink). The

primary task of the ganglion's cells is to transmit visual signals to the brain. Next, the apical sided dendrites of the ganglion cells, amacrine cells, bipolar cells and horizontal cells form the inner plexiform layer (IPL; Figure 3a purple). The bodies of these cells form the inner nuclear layer (INL; Figure 3a green). The basal sided dendrites of these cells form the outer plexiform layer (OPL; Figure 3a orange). The photoreceptor's cell body (containing the nucleus) forms the outer nuclear layer (ONL; Figure 3a dark blue). The outer limiting membrane (OLM; not colored in Figure 3a) located between the ONL and the junction of the inner- and outer-segments (IS/OS; Figure 3a dark blue and light blue) is thought "to play a role in maintaining the structure of the retina through mechanical strength"[40] and is "considered as a part of the retinal barrier that can be disrupted in [a] pathological condition."[40] This layer is not visible in Figure 3 (H&E staining does not make this layer visible). The outer segments of the photoreceptors (rod and cone cells) define the outer end of the neural retina. These outer segments are in direct contact with the highly pigmented RPE. The RPE is discussed in more detail in chapter 2.2.2. The outer segments of the photoreceptors and the RPE form the outer segment of the PR and RPE (OPR) complex. This layer is followed by the pure RPE layer, Bruch's membrane, and the choroid.

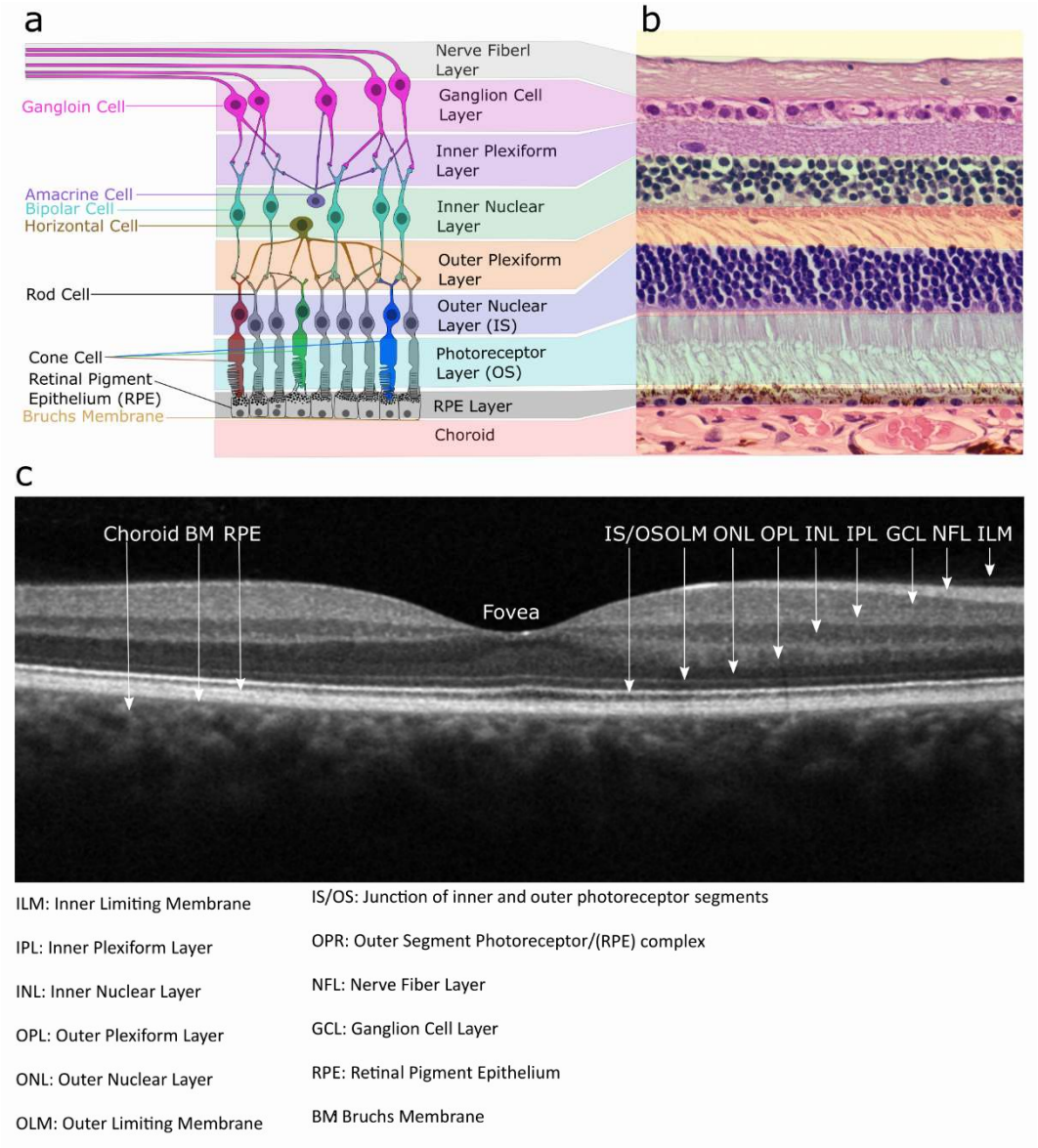

Figure 3. a) Illustration of cells in the human fundus [made by the Author]. The sketch only shows the cells that are visible in the histologic figure in subfigure b. b) Edited histologic image of human fundus (hematoxylin and eosin stain) [Science-Photo.de; Licensed for this thesis]. C) Optical coherence tomography image of a healthy human retina [Fundus of the author]. By comparing the subfigures, it can be seen that each cell-type contributes to several layers in the OCT image. Pathologic changes, as presented in the following chapters, are characterized by their morphologic changes like detachment of retinal layers from the RPE and edema.

This knowledge of the layered structure of the retina is required in this work to understand how the spatial extent of cell damage influences the degree of vision impairment that can be induced by laser irradiation. If cell damage can be limited to the light absorbing RPE, it can be assumed that no vision impairment has been induced by the

laser irradiation, since the photoreceptors and all layers would have experienced almost no heating. The more photoreceptors and interconnecting cells are damaged, the more severe the local visual impairment becomes. Moreover, damaging the nerve fiber layer (NFL) needs to be avoided in all laser treatment modalities, since this can lead to large blind spots (scotoma) from all regions from which the damaged nerve fibers originate.

2.2.2 The retinal pigment epithelium and choroid

2.2.2.1 Absorption properties of the fundus

Absorption properties of the fundus are affected by its two most pigmented layers: the RPE and choroid. The major light absorbing pigment is melanin, and it is stored in the melanosomes. Early studies on the concentration and distribution of melanin in the RPE have demonstrated intra- and interindividual variations of local light absorption by a factor of 1.75 to 2 at a wavelength of 500nm.[30] There are systematic and random influences on the melanin distribution in the RPE and choroid Regarding spatial variations of melanin concentration in the RPE, a pigmentation peak can be found in the macula region. The pigmentation decreases outside of the macula and then increases again in the periphery. The concentration of another pigment called lipofuscin is highest in the macula, and it has a local decrease at the fovea.[41] Age and disease influence the absorption properties of the RPE and lead to interindividual variations in local light absorption by a factor of four.[10] The absorption within a region of the size of a laser-spot varies by 3 %.[42, 43] Within an RPE cell, the melanosomes accumulate at the photoreceptor sided (apical) end. Figure 4 displays the photoreceptors (elliptical shapes in the upper part), melanosomes (smaller round black shapes in the center), and one nucleus (bigger circular structure in the lower middle). Due to the apical sided allocation of the melanosomes, RPE light absorption can be expected to take place primarily in the first two to three micrometers of this layer. Below the RPE is where the non-pigmented Bruch's membrane and the pigmented choroid are located. The choroid reaches its maximum melanin pigmentation at the macula region, and its melanin pigmentation steadily decreases in the periphery.[41] Its absorption varies by a factor around 2 (evaluated via spectral absorption measurements in humane eyes).[30]

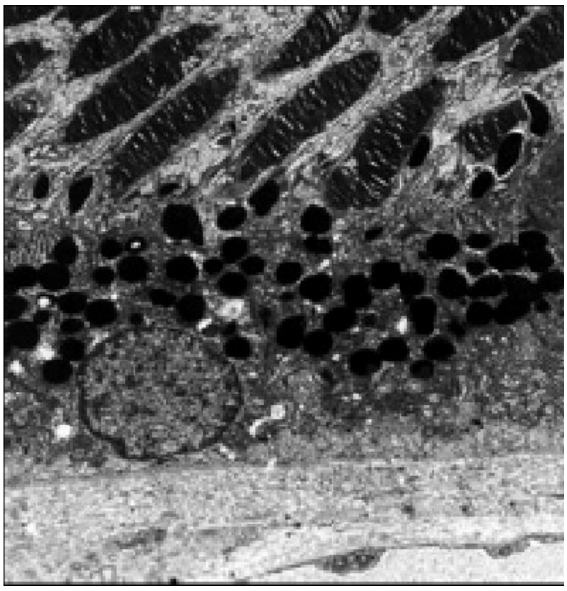

Figure 4. Electron microscope image of the RPE. It can be seen that melanosomes (black round objects) accumulate at the photoreceptor sided region of the RPE cell.[44]

The absorbed energy in the RPE is nearly equal to the energy absorbed in the choroid (51.5 % of the light in the green regime is absorbed in the RPE[45]). However, due to the much smaller thickness of the RPE, its energy density is higher. Hence, the role of the RPE is important in laser treatments using lasers in the green spectral regime (515-527nm).[30]

In clinical practice, variation of RPE pigmentation and transparency of the anterior eye media (chapter 2.1) make a prediction of the laser power to induce an intended effect unpredictable. Thus, there is a risk of inducing a larger volume of damage than required for treatment. Likewise, there is a risk of the absence of any biological effect. These risks justify the necessity of innovating techniques that can be used to support a treating clinician.

2.2.2.2 Selected properties of the RPE

RPE cell are interconnected with tight junctions. These junctions connect the RPE cells as well as regulate cell proliferation, polarity, and para-cellular diffusion.[46] The latter aspects make the RPE layer especially critical for the supply of the neural retina. The tight junctions enable also make the RPE to an important part of the blood-retina-barrier. Diseases like age-related macular degeneration and diabetic retinopathy are "… directly associated with alterations of the blood-retina barrier."[47]

Furthermore, the RPE is significant because it secretes multiple factors such as growth factors and factors related to the structural integrity of the retina and choriocapillaris.[48] Among the growth factors secreted by the RPE is the vascular endothelial growth factor (VEGF). In healthy eyes, VEGFs are expressed in low amounts. This moderation prevents endothelial cell apoptosis, keeps the choriocapillaris intact, and acts as a permeability factor for the endothelium.[48-54] Overproduction of VEGFs, which can be triggered by hypo-oxygenation, seems to play a key role in the development of proliferative diabetic retinopathy.[48, 55] Thus, the reduction of VEGFs is a significant goal of most treatment modalities, including those of panretinal photocoagulation (PRP; laser treatment) and intraocular injection of VEGF blockers (drugs).

Another relevant factor produced in the RPE is the heat-shock protein (HSP), which is required for normal cell function.[56-59] The HSP90 (an HSP with 90kDa) accounts for 1 % to 2 % of a cell's total proteins under non-stress conditions.[59] These proteins are expressed even more during almost all types of cellular stress, especially during heat shocks.[57-59] Depending on the treatment scenario, a decrease or increase of HSP could be therapeutically instigated.[59] In RPE treatments, HSP is significant because it "may serve a protective role, activating cellular response, and slowing or preventing apoptotic and inflammatory pathways that lead to cellular damage."[60]

Retinal pigment epithelium (RPE) cells do not divide, migrate, or proliferate if they are in direct contact with a neighboring RPE cell. As soon as direct contact with a neighboring cell is lost (e.g., due to a small laser lesion affecting the RPE exclusively), the proliferation and migration of neighboring RPE cells cause the lesion to close.[61] In-vitro studies of selective lesions on porcine RPE-choroid explants have demonstrated that the expression of cell mediators, such as matrix metalloproteinase 2 (MMP2), VEGF, and pigment epithelial-derived growth factors (PEGFs), depends on the size of a lesion as well as the area treated.[62]

In this work, optimal laser parameters for an effective treatment are discussed. Studies were performed with the setup described in chapter 3.2. Knowledge about the role of the RPE is relevant to system-design decisions, as it can be argued that affecting the RPE cells selectively can be sufficient in the treatment of some disease (details in the next chapter). To have an effect on a pathologic condition, laser parameters that allow selective RPE effects are to be preferred, since additional damage would be considered as collateral damage.

2.3 Retinal diseases

Previous studies have already shown beneficial effects of selective RPE damage in the treatment of diabetic retinopathy (DR) and central serious chorioretinopathy (CSCR).[12, 63, 64] In addition, the clinical studies presented in this work treated patients with these diseases. The following chapters discuss DR and CSCR in more detail.

2.3.1 Diabetic retinopathy

2.3.1.1 Epidemiology

DR is among the major causes of visual impairment in industrialized countries. The number of people with diabetes is predicted to increase from 285 million (6.4 % of people between the ages of 20–79 years) in 2010 to an estimated 439 million (7.7 % of people between the ages of 20–79 years) in 2030.[65] After 20 years, 30 % to 40 % of all patients with type 1 diabetes suffer from the advanced state of proliferative diabetic retinopathy (pDR). This state of DR is characterized by angiogenesis of the retinal vessels.[66] In patients with type 2 diabetes, the average prevalence of pDR is between 30 % and 40 % with a 10 % prevalence for diabetic macula edema (DME).[66]

2.3.1.2 Pathology

The exact pathogenesis of DR is not fully understood yet. It can be assumed that hyperglycemia is the underlying cause of DR, since it has a variety of direct and indirect effects on the retinal blood flow (including ischemia), basement membrane thickening, and several growth factors.[67-69] Together, these factors lead to a hypo-oxygenation of the fundus. Additional pathways that may be involved in the development of DR are “inflammation, nerve growth factor autophagy, and epigenetics.”[66]

To combat the under-supply of oxygen (hypo-oxygenation), VEGF expression is upregulated. This leads to an increase in the number of blood vessels in the undersupplied area. However, these new blood vessels have weak walls. Thus, they are dangerous for the patient due to an increased risk of intraocular bleeding. High blood pressure further increases this risk. Bleeding can lead to an instantaneous loss of vision, scar formation, retinal detachment and other effects. Furthermore, the increased vascular permeability and angiogenesis can lead to macular edema, which causes also visual impairment.[70]

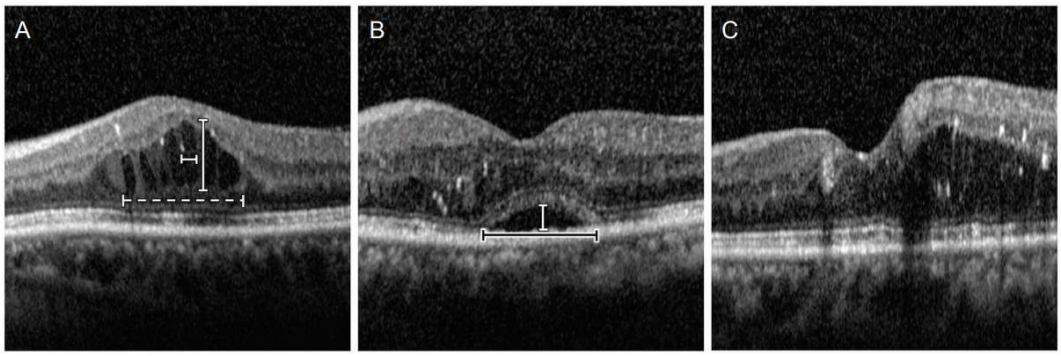

Figure 5. Images A, B, and C show OCT B-scans of diabetic macula edema.[71] The larger distances between neuronal retina and RPE make ophthalmoscopic visibility a suboptimal predictor for RPE cell damage.

2.3.1.3 Classic treatment options

Treatment of DR includes the reduction of hypoglycemia and blood pressure in order to increase oxygenation of the hypo-oxygenated tissue and reduce the production or efficiency of the VEGF proteins. While hyperglycemia and blood pressure can be affected by a patient's lifestyle and medication,[67, 72] oxygenation and growth factor influences must be affected by therapeutic approaches, including pan-retinal photocoagulation (PRP) and the intraocular injection of VEGF blockers. Notably, the early treatment in diabetic retinopathy study (ETDRS) revealed that PRP reduces the risk of vision loss. Since this discover, PRP has become a standard therapy for DR.[73] Treatment of DR and DME should optimally be performed when DR has reached a clinically significant state, but before visual acuity is significantly affected.[66, 74] Visual loss in DME patients can be reduced by at least 50 % if laser treatment is performed. [66, 74, 75] The benefits of PRP have been assumed to be caused by the reduced oxygen requirements of the fundus, since the oxygen-consuming photoreceptors in the treated area are devitalized during this process.[76, 77] The wound healing process of PRP is characterized by scar formation.[78] The reduced oxygen requirements in the periphery, where this treatment is performed through a high number (around 1,000) of irradiated regions (spots), benefits the macula.

In the last decades, the intraocular injection of VEGF blockers has also become a standard treatment for the reduction of neovascularization. The advantage of this method is that it does not induce large areas of visual impairment in the periphery. Its disadvantage, however, is an increased risk of RPE atrophy.[79-83]

2.3.1.4 SRT in DME treatment

In the case of a diabetic macula edema, a focal laser treatment can be applied to affect the malfunctioning retinal pigment epithelium. In this treatment, a small number of spots

(usually less than 10) are placed in (or close to) the edema with a minimum distance of 200 µm to the fovea. In one study with 39 patients, the application of SRT led to an improvement in clinical criteria (best corrected visual acuity, BCVA) after 6 months. [14] Treatment outcome can vary from treatments previous to SRT-irradiation. It has been reported that pan retinal photocoagulation and insulin treatment may influence the effect of SRT positively but macula near coagulation may affect the outcome negatively. [84] Further studies on DME with positive outcome have been performed with the systems developed in this work. [85]

2.3.2 Central serous retinopathy

2.3.2.1 Terminology and epidemiology

Central serious chorioretinopathy is addressed in existing literature by many different names and abbreviations, often with little or no difference in the pathology being described. It has been abbreviated as “CSCR”; “CSC”; “CSR”; “iCSR”; and “iCSC”. In these abbreviations, the letter “i” stands for idiopathic (unknown cause). Central serious chorioretinopathy is also known as “retinal pigment epitheliopathy” and “relapsing central retinitis.” The last term was used by Albrecht von Greafe, who first described this pathology in 1866.[86-88] In the present work, central serious chorioretinopathy is referred to as CSCR.[89]

The mean adjusted incident rate of CSCR is 9.9 per 100,000 men and 1.7 per 100,000 women.[90] Thirty-one percent of all patients experience a recurrence of the disease within 1.3 years.[86]

2.3.2.2 Pathology

The pathogenesis of CSCR is not completely understood. Regardless of whether or not the disease originates in the choroid,[91] the RPE,[92] or a combination of the two, both layers play a role in the development of the symptoms of CSCR.[93] In an acute case, CSCR is characterized by “a detachment of the neurosensory retina with accumulation of serous fluid between the retinal pigment epithelium and photo-receptor outer segments.”[86] Figure 6 shows a detached retina. Retinal pigment epithelium detachment (PED) can accompany CSCR[94] and is reported to be indicated by pigment clumping.[86] In older patients (50 years and up), typical symptoms include choroidal neovascularization.[95]

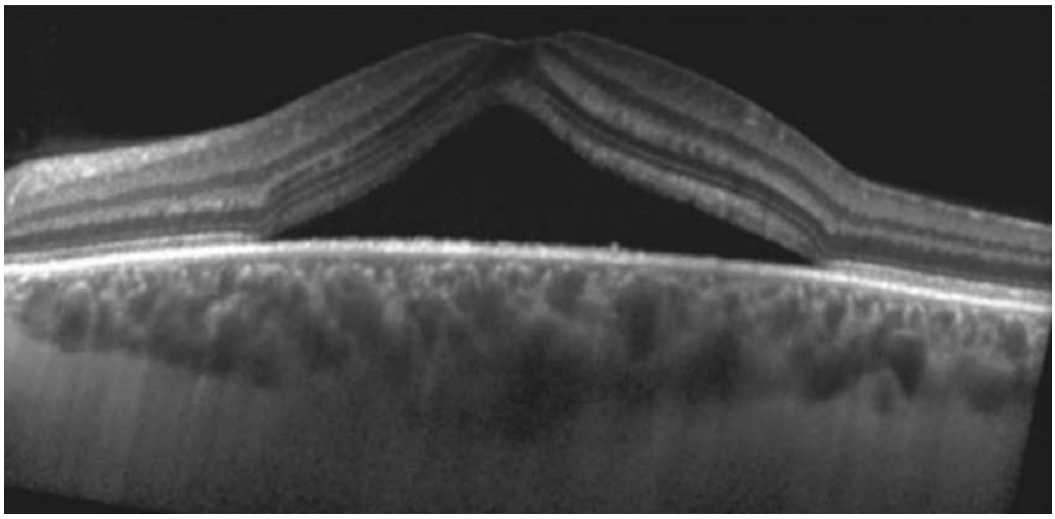

Figure 6. OCT image of retinal detachment from the RPE. [96] Due to the increased distance from the RPE to the retina, laser-induced heat needs to flow over a larger region until retinal layers become affected. This makes ophthalmoscopically visible effects a suboptimal measure for laser induced effects in the case of laser treatment of subretinal fluid.

The overall tendency of CSCR is favorable for the patient. Usually, the sub-retinal fluid resolves spontaneously and visual acuity is regained.[97] Hence, treatments with no or low side effects are the first choice. These treatments include checks and the eventual influence of corticosteroid levels as well as the observation of a potential healing response.[98]

However, extensive retinal pigment atrophy, macular hemorrhage, and "pigmentary disturbances in the macular area resembling to some extent age-related macular degeneration (AMD)" have been observed in untreated cases.[99] Moreover, if the disease persists (chronic CSCR) additional treatments may be necessary to avoid complications, such as peripheral retinal detachments, retinal pigment epithelial atrophic tracts, chronic macula edema, and retinal atrophy.[100-102] A detached retina experiences damage over time. In some cases, the best corrected visual acuity (BCVA) is still reduced four months after the resolution of serous detachment.[102] Given that a resolution of an edema may take several weeks, early treatment after the occurrence of symptoms is reasonable.

2.3.2.3 Classical treatment options

In some CSCR treatments, the choroid is targeted. Photodynamic therapy (PDT) with verteporfin has been investigated regarding its suitability for CSCR treatment. Treatments with conventional PDT parameters applied to AMD (total light energy 50 J/cm^2; light dose

rate of 600 W/cm²; and a treatment time of 15 minutes) have been found to have side effects.[103-107] Thus, laser parameters have been adapted to reduce these effects while maintaining the treatment's therapeutic effect.[108-111]

Photocoagulation can also be an option to treat chronic CSCR. In the case of traditional photocoagulation, special care needs to be taken to avoid damage to the retina, since the neural retina does not seem to play a role in the pathogenesis of CSCR. Hence, retinal whitening due to coagulation "does not constitute a criteria for coagulation effectiveness in CSCR."[112] Furthermore, traditional photocoagulation for CSCR is suggested only in "acute CSC with obvious focal leakage in FA,"[93] since the benefit of photocoagulation in CSCR is the reduced time of CSCR induced edema resolution. [113]

Photocoagulation is limited in its total number of irradiated regions (spots) and localization of spots in CSCR treatments because damage to the neural retina needs to be avoided when it is applied in the macula region, especially when ophthalmoscopic visible effects are used as endpoint indicators. Especially in chronic CSCR the RPE dysfunction is supposed to affect the whole RPE (not just the symptomatic region), [93, 98, 102] If this hypothesis is true the limitation in the number of spots which is used to limit potential collateral damage, , may hinder the intervention's therapeutic effect. This makes laser treatment without collateral damage is desirable. There is a trend of applying coagulation laser spots with short pulse durations to reduce the spatial extent of coagulation damage (not just for reasons of CSCR treatment).[114-118]

2.3.2.4 SRT in CSCR treatment

CSCR is one of the most studied diseases when it comes to the application of SRT. The reason is the relatively quick (view months) and well visible response (reduction in subretinal fluid). An initial study with only 5 CSCR patients reported a reduction of subretinal fluid in only 5 Weeks in 4 of 5 Patients. [119] A following study with 27 patients has reported a complete resolution in 23 of27 patients after 4 Weeks and a resolution if subretinal fluid in 16 of 16 patients which were diagnosed after 3 months.[120] A further 2-center study reported with 10 cases of acute CSCR and 16 cases of chronic CSCR was performed. Subretinal fluid resolved in all 10 cases of acute CSCR and in 11 of 16 cases of chronic CSCR.[121] Another working group reported similar results with resolution of subretinal fluid in 11 of 17 eyes of patients with chronic CSCR after 3 month. [122] With a system developed during this study a total resolution of subretinal fluid in 9 of 12 patients. [123]

2.4 Microbubble formation

2.4.1 Laser irradiation induced retina heating

The laser induced effects discussed in this work are a result of an elevated temperature. The derivation of laser-induced change in retinal temperature is governed by the inhomogeneous partial heat diffusion equation (described in detail in several publications).[43, 124-127] The solution of the inhomogeneous heat diffusion equation was achieved by a convolution of Green's function with the source term.[43] There are solutions for a Gaussian beam profile and for a flat top, or top hat, beam shape.[43, 125, 127] In this work, the solution of Freund et al. for a rectangular top hat beam profile was used for calculations.[127] With this approach, the increase in temperature Δ*T* can be calculated by:

$$\Delta T = \exp(-\mu z)\exp(\kappa t'\mu^2)\frac{\mu I_0}{8r\rho\, c_p}\int_0^t R_{xy}R_z dt \qquad \textbf{1}$$

In the equation ΔT is the temperature increase, μ is the absorption coefficient, κ is the heat diffusivity, ρ is the mass density, c_p is the specific heat at constant pressure, t is the time, z is the spatial depth coordiante, and I_0 is the irradiance. R_{xy} is given by:

$$R_{xy} = \left\{erf\left[\frac{x+r}{2\sqrt{kt'}}\right] - erf\left[\frac{x-r}{2\sqrt{kt'}}\right]\right\}\left\{erf\left[\frac{y+r}{2\sqrt{kt'}}\right] - erf\left[\frac{y-r}{2\sqrt{kt'}}\right]\right\} \qquad \textbf{2}$$

with the coordinates x and y and the spatial variable r. R_z is given by:

$$R_z = \left\{erf\left[\frac{z}{2\sqrt{kt'}} - \mu\sqrt{kt'}\right] - erf\left[\frac{z-d}{2\sqrt{kt'}} - \mu\sqrt{kt'}\right]\right\} \qquad \textbf{3}$$

Where erf stands for the error function and d stands for the depth variable (e.g. thickness of pigmented RPE-layer). The fundus is modeled as a layered structure with different optical properties. The overall temperature increase of the fundus ΔT_F is evaluated by superposition of the thermal increase induced by each layer. [127]

$$\Delta T_F = \Delta T_{RPE} + \Delta T_{Chor} \qquad 4$$

In equation 10, ΔT_{RPE} represents the temperature increase of the RPE and ΔT_{Chor} is the temperature increase of the choroid.

2.4.2 Boiling / Microbubble formation

At sufficiently high laser irradiation induced temperature elevations ΔT_F close to the light absorbing melanosomes a phase change of the cell liquid from liquid to gas takes place. The phase change from liquid to gas is a non-continuous phase change (phase change of the 1st order). This non-continuity is characterized by a required energy surplus (latent heat) that is needed to induce the phase change. For melanosomes in suspension, the nucleation temperature was found to be located at $157 \pm 33\,°C$ for a pulse duration of 1.8µs.[128] As soon as vapor is induced by heating at a constant pressure ("boiling"), bubble formation takes place. This also includes complex processes like bubble coalescence, which cannot be described by the mathematical models mentioned in the following paragraphs. In the case of microbubble formation around single melanosomes, bubbles have a maximum diameter in the lower micrometer regime.[129, 130]

The simulation models applied in this work required knowledge about the temporal evolution of the microbubble diameter. This temporal evolution of a single bubble can be described with the general form of the Rayleigh-Plesset equation[131]:

$$\frac{p_V(T_\infty) - p_\infty(t)}{\rho_L} + \frac{p_V(T_B) - p_V(T_\infty)}{\rho_L} + \frac{p_{G_0}}{\rho_L}\left(\frac{T_B}{T_\infty}\right)\left(\frac{R_0}{R}\right)^3 = R\frac{d^2R}{dt^2} + \frac{3}{2}\left(\frac{dR}{dt}\right)^2 + \frac{4v_L}{R}\frac{dR}{dt} + \frac{2S}{\rho_L R} \qquad \textbf{5}$$

The vapor pressure is referred to as p_V, the ambient pressure is referred to as p_∞, the density of the liquid is referred to as ρ_L, the pressure of the contaminant gas within the bubble is referred to as p_{G_0}, the initial Radius of the spherical bubble is R_0, the bubble radius at a certain point in time is referred to as R, the viscosity is referred to as v_L, and the surface tension is referred to as S. The temperature T_∞ is assumed to be constant. The vapor pressure within a bubble p_V and the temperature within a bubble T_B are assumed to be uniform. The initial state of bubble growth is governed by the momentum interaction (equation 5, term 1) between the bubble and the fluid. The influence of thermal effects (the second term of equation 5) is low. Under the absence of thermal effects and the additional assumption of polytropic properties, the equation becomes: [131] [132]

$$\frac{p_V(T_\infty) - p_\infty(t)}{\rho_L} + \frac{P_0 + 2S/R}{\rho_L}\left(\frac{R_0}{R}\right)^{3k} = R\ddot{R} + \frac{3}{2}\dot{R}^2 + \frac{4v_L\dot{R}}{R} + \frac{2S}{\rho_L R} \qquad \textbf{6}$$

In this case, *k* is the polytropic index and $P_0 = p_\infty(0) - p_V(T_\infty)$. [131] This equation can be solved numerically. Figure 7a and b show the time evolution of microbubbles with different initial bubble radii R_0. The differential equation solver of the library SciPy

(programming language Python) was used to solve equation 6. The graphs were generated with the Python library Matpotlib. In these simulations, the laser pulse started at t=0 µs and ended at t=1.7 µs. Temperature values have been calculated in advance with equation 4. The maximum bubble diameter was reached after the laser irradiation. The graphs in Figure 9 and Figure 10 were calculated with the following parameters for water $p_\infty = 1\ bar,\ \rho_L = 1000\ kg/m^3,\ v_L = 0.00089\ mPa\ s,\ k = 1.33,\ S = 0.0728\ mN/m.$ Absorbing micrometer sized particles like melanin were not considered in particular.

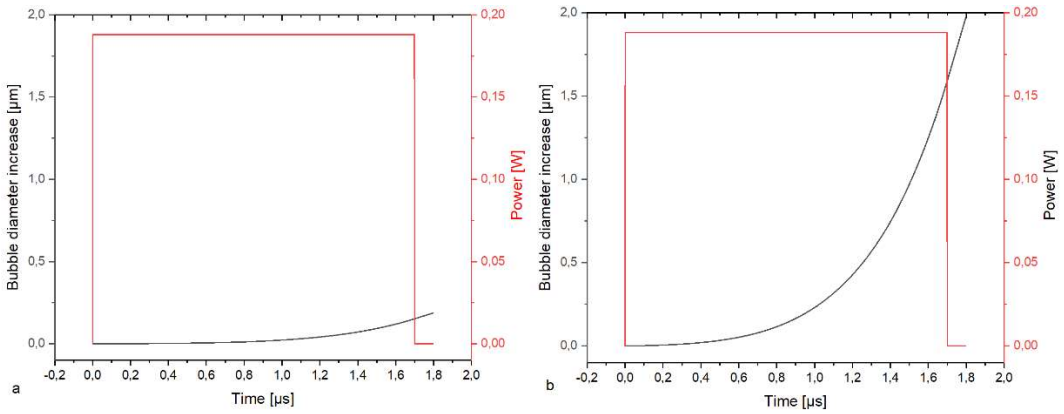

Figure 7 Microbubble diameter increase (black) induced by a 1.7 µs laser pulse (red) that led to an end temperature of 160 °C at the end of the pulse. The initial bubble diameter was set to a) $R_0 = 0.5\ \mu m$ b) $R_0 = 5\ \mu m$

With an increase of 0,151µm during the time of heating at an initial radius of 1µm and an increase of 1,59µm with and initial radius of 10µm an almost linear relationship can be assumed. However, in calculations later in this work, the absolute change, not the relative change, is of major importance.

It needs to be mentioned that this simulation did not consider changes in transmission and scattering properties of the tissue that are induced by the microbubble itself. Changes of the tissue (cell disintegration) inflicted by the microbubble were also not considered. Neither is bubble coalescence. In the chapters 2.4.4 and 2.4.5, previous experimental studies on microbubbles dynamics are discussed to illustrate the eventual blind-spots of the Rayleigh Plesset model, which is used in this work to calculate the microbubble diameter.

2.4.3 (Opto-)Acoustic emission

Any event that accelerates its surrounding liquid induces an acoustic transient. [133] In this work, microbubbles and thermal expansion were relevant sources of acoustic transie

nts. With thermoelastic expansions, the maximum pressure is proportional to the material-specific and temperature dependent Grüneisen Parameter Γ and the laser pulse energy E.[134]

$$p^{max}(T) \sim \Gamma(T) \cdot E \qquad \textbf{7}$$

Previous works studying short pulsed lasers (pulse duration in nanosecond regime) also made use of this temperature dependency of the maximum pressure, in the regime of several hundred micro bar, to measure the temperature during laser photocoagulation of the retina.[135, 136] Furthermore, research has found pulses with a duration of 1.7μs (outside thermal- and stress- confinement) to be applicable for optoacoustic (OA) pressure generation.[137]

A study on the acoustic emission of microbubbles has shown amplitudes marginally higher than those of thermoelastic expansions in the early stage of microbubble formation.[136] When analyzing the acoustic transients, the researchers observed that microbubbles could be identified by differences in the time evolution between consecutive pressure transients in the case of operating close to the threshold of microbubble formation.[136] The study found that if the laser pulse energy was further increased, the pressure of the transients would also increase to the lower mbar regime.[136]

From the perspective of optoacoustic microbubble detection techniques (details in chapter 2.6), transients of thermoelastic origin are physical noise components. In some studies presented in this work, a series of pulses with pulse-wise increasing laser pulse energy was applied. In these cases, p^{max} was influenced by both E and Γ (eqation 7). This interaction made it necessary to adapt algorithms for microbubble detection with normalization procedures (details in chapters 3.3.2.3, 4.5.3, and 5.6) to remove the influence of a change in laser pulse energy from the measured p_{max}.

2.4.4 Previous work on microbubble formation on single melanosomes

Previous studies on single porcine melanosomes in suspension have been performed by Neumann et al. In their work, a Nd:YLF laser (527nm, 200ns to 5 µs) and a Nd:YAG laser (532 nm, 12 ns) laser were used for the heating process. The transmission of continuous wave (cw) HeNe laser light (633 nm) was used to observe the microbubble lifetime. A N_2-pumped dye laser (470nm, 3ns) was used for high speed imaging. A self-made microscopy setup standard 40x objective images the microbubbles to a CCD camera.[138]

With this setup Neumann et. al. found that "… bubble dynamics strongly depend on the laser pulse duration of the heating laser. Due to heat diffusion out of the absorber during the laser pulse …, the threshold radiant exposure for bubble formation increases with pulse duration…"[130] Furthermore, Neumann et. al. reported that "the bubble dynamics have been proven to be temporally symmetrical i.e. the maximum bubble diameter during oscillation is observed at 50 % of its lifetime."[130] Microbubble oscillation was observed at pulse durations of 254 ns (Figure 8b) and 1.8 µs (Figure 8c). The researchers hypothesized that: "Only the surrounding metastable water, which was conductively heated by the particle before bubble nucleation, can vaporize at the bubble interface and increase the kinetic energy of the bubble." [130] After expansion and collapse of the microbubble, the water is able to make contact with the heated particle again. In equation 6 such complex interactions between the microbubbles and its surrounding were not considered.

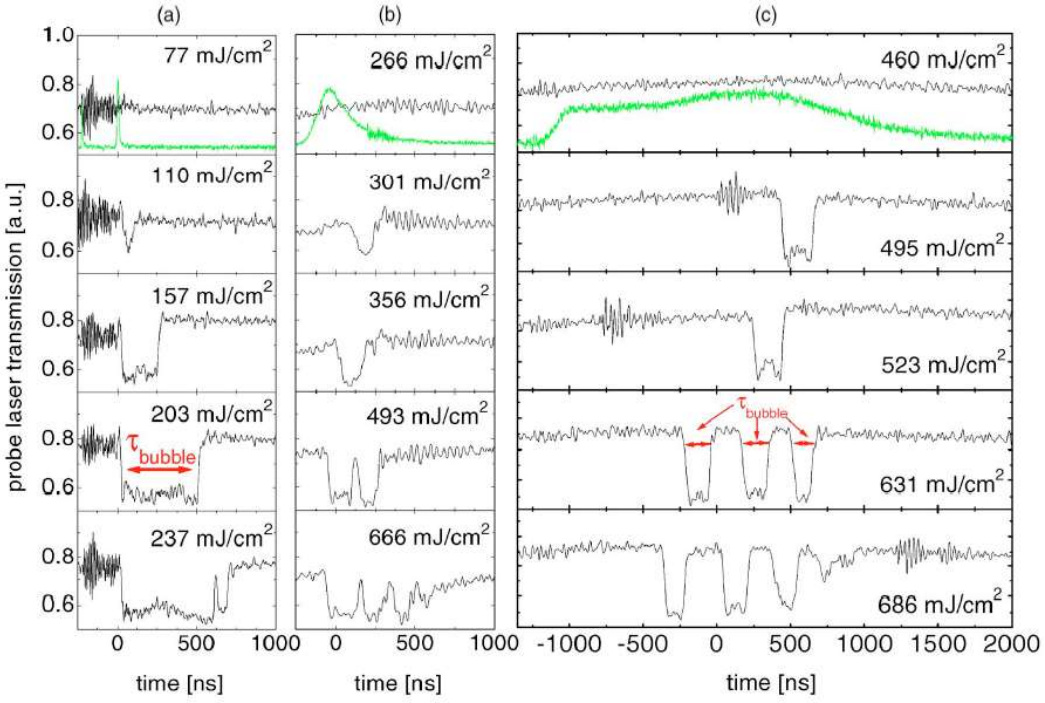

Figure 8. Light transmission for 12 ns (column a), 240 ns (column b), and 1.8 µs (column c). Green graph in the first row indicates the laser pulse. It can be seen that microbubble oscillations occurred at pulses with a duration of 240 ns and longer.[130] This is an additional indicator that microbubble growth is self-limiting. Moreover, this implies an important safety aspect, since it can be assumed that smaller bubbles induce less damage.

Another layer of complexity is added when a whole cell layer is considered instead of a single melanosome. An experiment considering this condition is presented in the next chapter.

2.4.5 Microbubble formation on RPE cells

It is well known that the dynamical properties, like expansion- and collapse-time, of a vaporization bubble are influenced by nearby particles and other bubbles. The experiment presented in the last chapter avoided these influences by irradiating single melanosomes in suspension. Thus, to gain a better understanding of microbubble dynamics under the presence of other bubbles and cell components, experiments on RPE were performed. An Nd:YLF laser (527 nm, 200 ns – 5 µs) served as a heat source and a helium-neon (HeNe) laser based Michelson interferometer (632.8 nm, 5 mW cw) was used to measure microbubble expansion and collapse. Expansion and collapse induce an ultrasonic pressure wave that can be registered with a hydrophone. This technique has been used as a reference measurement for bubble lifetime measurements.

It has been found that microbubbles not just last longer than the pulse duration, but that the microbubbles reach its maximum diameter after the laser pulse duration (after irradiation). The same is suggested by the results of the Rayleigh-Plesset model (chapter 2.4.2) Hence, backscattered light of the initial growing phase can analyzed only by a laser system with an additional illumination laser. Furthermore, the results of this experiment revealed an asymmetry in expansion and collapse. The bubble collapsed in around 30 % of the time required for expansion. In the case of melanosomes in an RPE, cell particles are located close to the microbubbles. Notably, the microbubble expansion processes have been found to take longer than bubble collapse.[25, 138, 139] Figure 9 displays this asymmetry. It was assumed that “the reason for the temporally asymmetrical bubble dynamics might be the coalescence of microbubbles after nucleation.”[23] Since bubbles arising from bubble coalescence can have a diameter above $10\,\mu m$ and significantly longer life times.[139]

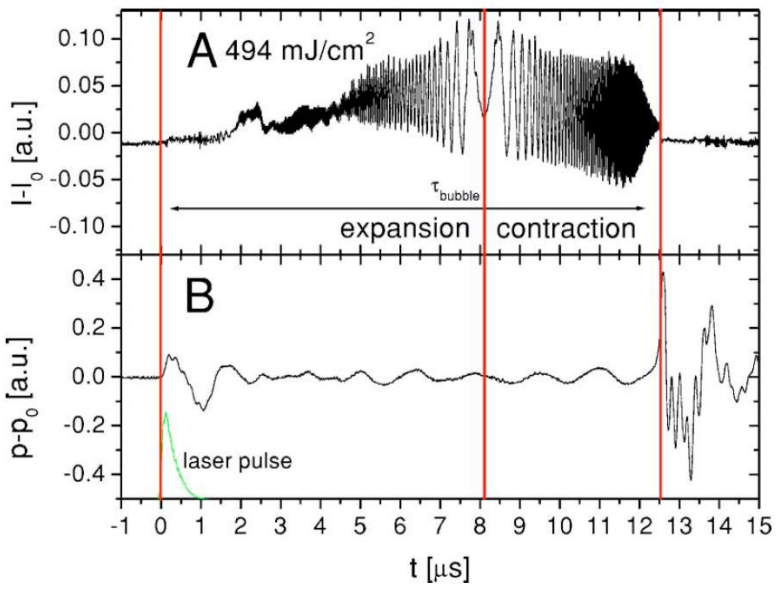

a

Figure 9a An interferometry signal and optoacoustic signal of a large microbubble.[23] The maximum diameter of the microbubble occurred after the laser irradiation.

2.5 Cell damage

2.5.1 RPE cell damage mechanisms

Light induced cell damage of the retina can be induced by several mechanisms. This chapter briefly introduces the two main mechanisms which are relevant for this work. This is thermal and thermomechanical cell damage.

Thermal cell damage is often described by protein denaturation. To a certain degree, thermal damage can be described by Arrehnius rate equations.[42, 125] Usually, thermal damage caused by laser pulses in the ms regime is ophthalmoscopically visible, unless the irradiation targets a region with subretinal fluid.[112] In the millisecond regime “the maximal peak temperatures after 200 ms are found around 70 °C to 85 °C at the end of the irradiation period for weak coagulations, while in stronger ones they can exceed 100 °C.”[140] Heat induced damage can also be confined close to the RPE [141] and some treatment procedures, which are based on the Arrhenius equation, are used for treatment. [142]

The Arrhenius damage model is not the only existing damage model used to describe thermal effects. Till et al. have suggested a biochemical damage process. They claim “that at threshold a short-duration, laser-induced, temperature rise melts the membrane of the melanosomes found in the pigmented retinal epithelial cells. This results in the generation

of free radicals which initiate a slow chain reaction."[143] In this work, laser pulses were applied. It is known that microbubbles arise at the melanosomes first. While Large microbubble may rupture the RPE in a way that is visible under a light microscope, small microbubbles at the threshold of cell damage may not. Special fluorescence microscopy techniques were applied to make damaged/dying cells with intact cell membrane visible (details in chapter 3.7.1)

Roider et al. have investigated whether the RPE can be selectively targeted by laser irradiation to spare the photoreceptors and choroid.[18] One approach to achieve this spatial confinement of laser-induced damage is based on the reduction of pulse durations below the thermal diffusion time of the heated medium (i.e., selective thermolysis).[17] This method leads to pulse durations in the lower microsecond and nanosecond regime. In this regime, multiple cell-damage mechanisms can take place simultaneously. For instance, thermal cell damage, which may be described with the Arrehnius damage integral,[125] may be accompanied by mechanical cell damage induced by the expansion and collapse of micrometer sized bubbles of vaporized cell liquid.[26]

The microscopical studies on thermomechanical cell damage mechanisms have been conducted by Lin et al proof that microbubbles can be the cause of cell damage. Figure 10 displays images of light microscopy and fluorescence microscopy of trabecular meshwork cells.[144] Subfigures a and d show cells before irradiation. In subfigures a and c, the small black particles are melanin granules. The bright structures in subfigure d are living trabecular meshwork cells. Subfigure b displays microbubble formation 225 ns after laser irradiation. The bubbles depicted appeared at the regions where the melanin was located. Subfigure e was acquired after the process of microbubble formation. Post irradiation, there were fewer melanin granules, and the remaining granules were displaced (subfigure c). Subfigure e displays fewer living meshwork cells than subfigure d. Living cells were missing at regions where microbubble formation had been observed. Subfigure f was acquired with a different fluorescent dye than subfigure b and e. In subfigure f, cell components of dying and dead cells are highlighted. These regions were located at places where microbubble formation had been observed.

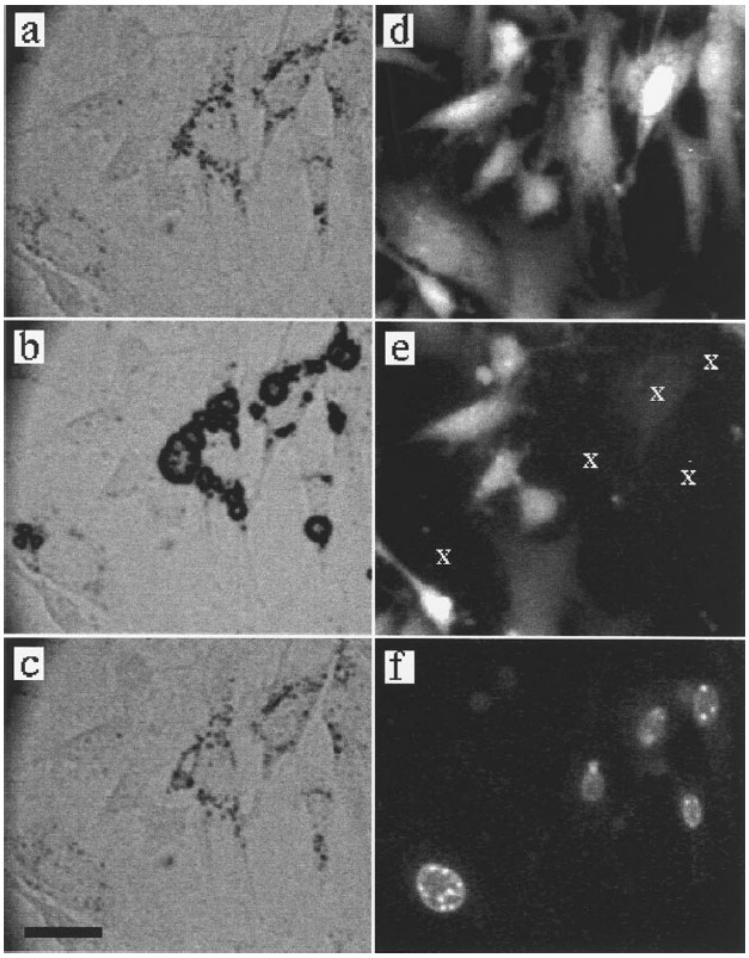

Figure 10. Left: Light microscopy images of cells a) before laser irradiation (melanin pigments are visible), b) 225 ns after laser irradiation (microbubbles are visible), c) seconds after laser irradiation (viewer and displaced melanin pigments are visible). Right: fluorescence images d) before laser irradiation (living cells are fluorescent), e) seconds after laser irradiation (living cells are fluorescent), f) seconds after irradiation (dead cells are fluorescent).[144] When comparing the images, it can be observed that microbubbles occurred at regions with melanin particles and dead cells were found in regions with microbubble formation.

While the work of Lin et.al. has shown that microbubbles can damage RPE cells it does not indicate at which pulse durations cell damage mechanism occurs first at the threshold of cell damage. Since this is a very relevant question to choose the right cell damage detection method, additional work has been done to answer this question. In studies conducted by Brinkmann et. al. it has been suggested that thermo-mechanical damage occurs at lower radiant exposure thresholds than thermal damage in the pulse duration regime between 1 ns and 1 µs.[145] Additional experimental studies by Schüle et.al. suggested that denaturation-induced cell damage occurs at lower radiant exposure thresholds than microbubble formation in the case of pulses around 50 µs and longer.[27, 145] In the present work the transition point of initial cell damage mechanisms was

allocated more precisely, due to a more precise (time-resolved) evaluation of the MBF threshold (see chapter 3.2, 4.1, 5.1).

2.5.2 Non visibility of RPE lesions

In chapters 2.3.1.4 and 2.3.2.4 it has been shown that selective RPE damage can be sufficient to achieve beneficial effect in the treatment of SCSR and DME. Unfortunately, if damage is confined to the RPE, no ophthalmoscopically visible changes can be detected during treatment [21]. Moreover, it is impossible to identify selective RPE damage visually without using additional techniques like fluorescein angiography.

In CSCR, the regions with retinal detachment should be treated. In the case of a detached retina, there is an increased distance from photoreceptors to the RPE in the range of several micrometers. As made apparent in previous chapters, heat diffusion plays a major role in the extent of the damaged volume around the light absorbing RPE. The farther away the neural retina is located from the RPE (the more the retina is detached from the RPE), the greater is the requirement for heat diffusion before the photoreceptor layer is affected by the heat. In some cases, RPE lesions may not even be visible to the treating clinician after the application of conventional photocoagulation.[112]

In a scenario where the goal is to study the selectivity of a laser treatment modality, the irradiation of regions with detached retina does not offer any information on whether an irradiation treatment would have also been RPE selective in a region without retinal detachment. If data regarding ophthalmoscopic visibility were to be gained from regions with subretinal fluid, the results would lead to exceptionally high thresholds to induce ophthalmoscopically visible lesions. These thresholds could not be transferred to irradiations where the retina is still attached to the RPE. Thus, a systems performance needs to be evaluated with data acquired from regions with attached retina, since this is the most difficult condition to obtain selective lesions. This is one reason why the treatment protocols in this study include so-called test spots that are placed in regions where subretinal fluid is absent (details in chapter 3.5).

2.5.3 Consequences of intra- and interindividual variations

As described in chapter 2.2.2.1, the adequate laser pulse energy for selective RPE cell damage varies intra- and interindividually. Thus, the required local threshold laser pulse energy cannot be predicted in advance. This unpredictability may lead to over- or under-treatment of a region. The definition of the terms over-treatment and under-treatment

are inconsistent. The definitions are dependent on the treatment type. In the case of conventional continuous wave laser irradiation (photocoagulation), under-treatment is defined as non-ophthalmoscopically visible lesions, and over-treatment is defined as lesions too large in diameter, ruptures, or hemorrhages. In the context of pulsed laser irradiation intended to target the RPE selectively, over-treatment is defined as ophthalmoscopically visible lesions, while under-treatment is defined as the absence of an evaluable effect on the RPE. Effects on the RPE are verified by additional diagnostic techniques like fluorescein angiography (details in chapter 3.7.3).

Microbubble detection techniques can be used to predict cell damage as well in the lower µs regime.[146] However, to do so without automatic laser irradiation ceasing, a well-defined treatment protocol need to be followed. Early studies on SRT made use of a treatment protocol that included titration irradiations (test spots) in the periphery followed by fluorescein angiography. The threshold laser pulse energy evaluated with this procedure was then used to treat the diseased area (in the macula). While this is a very reasonable treatment protocol for clinical studies, it is quite impractical for clinical practice, since it is time consuming, labor-intensive, and expensive. Since microbubbles can be the origin of RPE cell damage, a microbubble detection technique may be able to indicate whether cell damage has been induced. The techniques described in this work were built to detect microbubbles by analyzing optical and acoustical data.

The following chapters introduce aspects of acoustical and optical effects originating from microbubble formation. These effects are relevant for signal processing of acoustic data and for the simulation of optical effects.

2.6 Acoustic sensing of microbubbles

2.6.1 Thermoelastic signal characteristics

The effect of temperature dependence of optoacoustic pressure transients in the laser heating process of the fundus has been described by Kandulla et al.[147] The change in pressure dp is influenced by the laser's pulse duration. If the pulse duration is below the time required for a pressure wave to leave the heated region during the time of irradiation (stress confinement), the dp becomes:

$$dp = \frac{\beta}{\kappa_T} dT \qquad \textbf{8}$$

The thermal expansion coefficient is referred to as β and the isobaric compressibility is referred to as κ_T. The temperature increase at a single point can be described with the following equation:

$$dT = \frac{\mu_a}{\rho_0 \, c_p} H \qquad \textbf{9}$$

The absorption coefficient is referred to as μ_a, the density is referred to as ρ_0, the specific heat is referred to as c_p and the radiant exposure is referred to as *H.* Thus, the pressure increase becomes

$$dp = \mu_a \frac{\beta}{\kappa_T \, \rho_0 \, c_p} H = \mu_a \Gamma H \qquad \textbf{10}$$

In a work of Schüle et al. it can be seen that temperature measurements are also possible with laser pulses of 1.7 µs.[148] Lasers with these properties were also used in this study with repetitive irradiations (30 Pulses; 100 Hz) with linearly increasing radiant exposure (details in chapter 3.3). This leads to an increase in pressure. Algorithms to detect microbubbles need to be designed in a way that does not falsely interpret a heat induced linear increase of the optoacoustic amplitude as an indicator for microbubbles (details in chapters 3.3.2.3, and 5.6).

2.6.2 Microbubble characteristics: Non-linearity

In order to develop algorithms to identify microbubble formation in optoacoustic pressure transients, it is important to know how microbubble formation influences the transients. In a study by Lin et al., sharp increases in the acoustic amplitude and acoustic energy (55 mJ/cm² at 532 nm for melanosomes in water) were found to coincide with the threshold for microbubble formation.[149]

In this work, there are setups that make use of a series of pulses with increasing laser pulse energy. Below the radiant exposure threshold for microbubble formation H_{MBF}, a series of laser pulses with increasing laser pulse energy leads to a linear increase in the amplitude of pressure transients. If the laser pulse energy is increased further above the threshold for microbubble formation, the additional pressure wave of the microbubble interferes with the pressure wave which is induced by thermoelastic expansion, and the resulting pressure transient becomes significantly larger. The sudden non-linear increase in acoustic pressure is used as an indicator for microbubble formation. The algorithm to utilize this phenomenon is described in chapter 3.3.2.3. In Figure 11b two transients with

an without microbubble formation were shown. The difference in laser pulse energy was around a factor of two. The transients' amplitudes differ by a significantly larger amount which cannot be explained without considering microbubble formation.

2.6.3 Microbubble characteristics: Loss of time invariance

The nonlinear increase in amplitude is not the only indicator of microbubble formation that can be extracted from pressure transients. Schüle et al. also found that close above the point of microbubble formation, variations in the temporal course of the optoacoustic transients can be observed.[136] This indicated that the time invariance that characterizes thermoelastic effects (Figure 11a) is non-existent in the case of microbubble formation. Thus, a series of consecutive pulses with the same laser-settings would cause different pressure transients (Figure 11b).

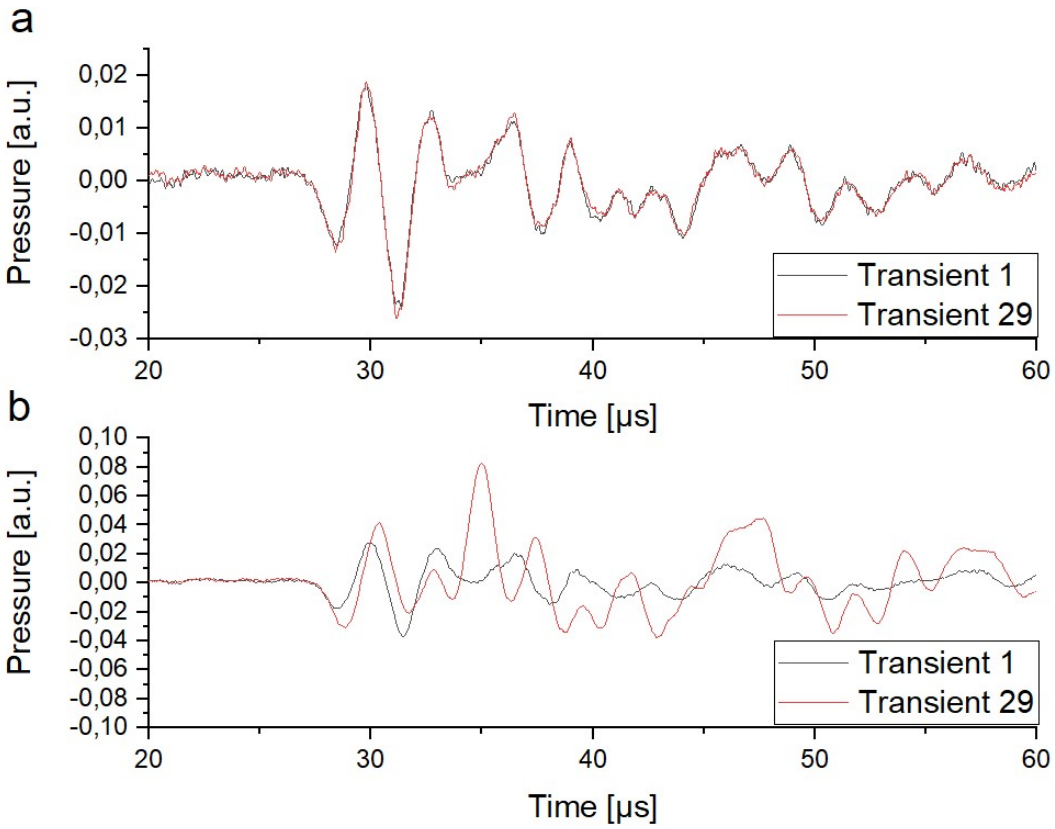

Figure 11. Subfigure a shows the 1st and 29th optoacoustic transient without microbubble formation. The laser pulse energy was kept constant in this example. The transients are almost identical. Subfigure b shows two pulses with microbubble formation. The difference in laser pulse energy between the laser pulses was around a factor of two. The transients' amplitudes are much higher, and the time evolution of the 1st and 29th transient differ noticeably. Increases in amplitude and time invariance are the signal characteristics algorithms were designed to detect.

2.6.4 Microbubble characteristics: Time of transient occurrence

As described previously, acoustic transients can be induced by thermoelastic expansion and relaxation, especially in the case of stress confinement. In the case of longer pulses far outside the regime of stress confinement or even thermal confinement, optoacoustic transients can also be induced if the on- and off-flank of the laser pulse has a steep change in laser power ($^{dP}/_{dt} > 10\ W/\mu s$). If the pulse is long enough (around 20 µs in the case of the ring transducers used in this work) the transients originating from the heating and cooling process can be discriminated from each other. The second transient (cooling phase) has been repeatedly observed to be larger than the heating transient. This holds true even if differences in the slope of the on- and off-flank are considered. Thus, temperature influences can be found with longer micro pulses (10 µs and longer) as well. Figure 12a depicts this case.

When long pulses are used in laser irradiation, microbubbles can be detected by the point in time of their initial occurrence. Whereas thermal relaxation sets in when the laser irradiation ceases, microbubble formation occurs during laser irradiation. Thus, if a transient is detected in a time interval before thermal relaxation effects are to be expected, thermal relaxation can be excluded as a possible sonic source. Moreover, microbubble formation would be the only other known sonic source during this stage. The time from the onset of the first transient to the onset of the microbubble associated transient can be measured with a temporal resolution of 10 ns. As the time evolution of the laser-pulse power is recorded with every pulse (also with a temporal resolution of 10ns), the threshold laser pulse energy for microbubble formation can be calculated by integrating the laser power to the time of microbubble formation (Figure 12b purple area under pulse).

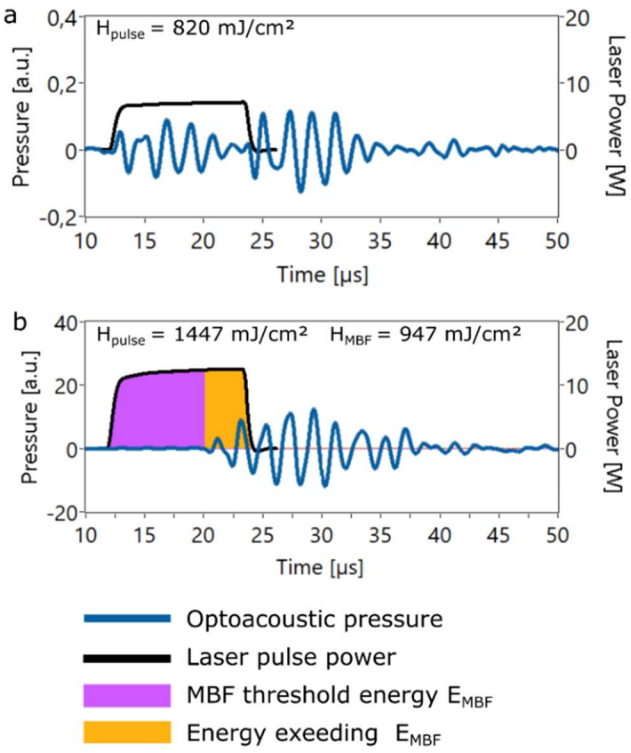

Figure 12. Microbubble detection at pulse durations of 12 µs. In subfigure a, the two thermoelastic components can be distinguished. In subfigure b, the microbubble induced signal components can be identified by amplitude and the point in time of occurrence. For illustration purposes, the acoustic pressure transient was shifted to the transition time required to travel from the RPE to the sensor.

Previous studies investigating threshold radiant exposures required multiple irradiations with increasing laser pulse energy to find one sample for a threshold value.[28] The step size at which the laser pulse energy is increased determines the resolution of threshold determination. Considering that a RPE specimen offers only a limited amount of space and pigmentation variations can be large, step sizes of 10 µJ to 50 µJ are common.

By the identification of the point in time of microbubble occurrence, the laser pulse energy resolution of microbubble formation threshold identification can be increased. The pulse energy resolution of this new method of optoacoustic microbubble detection is determined by the sampling frequency of the digitizer. In this work a GaGe digitizer with a sampling frequency of 100 MHz was used. With a sampling interval of $t_s = 10\ ns$ and a laser power of $P = 10\ W$, the laser pulse energy could be sampled with a resolution of $E_{res} = t_s * P = 100\ nJ$. Furthermore, this threshold can be evaluated for each irradiation which exceeded the threshold of microbubble formation. Before, it was just one irradiation in a sequence of around 10 irradiations. This increases the yield of

evaluable data per experiment. With this enhanced solution, previous measurements of Schüle et al. are repeated in this text (details in chapter 3.2 and 4.1).

2.7 Optical effects induced by laser irradiation

2.7.1 Scattering due to microbubbles

When the influence of microbubbles in the optical field needs to be evaluated, the change in refractive index should be considered as well. The relatively high difference between the cell liquid surrounding the microbubble (n=1.33) and the vaporized cell liquid of the microbubble (n=1) makes it necessary to handle the microbubble as a separate particle that changes in size. With a wavelength in the green spectral regime and a microbubble diameter in the lower µm regime, Mie-scattering calculations should be applied to calculate amplitude and phase of the optical field. [150]

2.7.1.1 Mie scattering in the far field

In Mie theory, the electrical field which interacts with a scattering object is assumed to be a plane wave. [151] If the distance between the microbubble and the observer is large (far field), the angular distribution of the scattered field ($E_{\parallel S}$ and $E_{\perp S}$) can be described by a propagation term, a scattering matrix, and an incident field ($E_{\parallel I}$ and $E_{\perp I}$):

$$\begin{pmatrix} E_{\parallel S} \\ E_{\perp S} \end{pmatrix} = \frac{e^{-ikr}\, e^{ikz}}{ikr} \begin{pmatrix} S_2 & 0 \\ 0 & S_1 \end{pmatrix} \begin{pmatrix} E_{\parallel I} \\ E_{\perp I} \end{pmatrix} \qquad \textbf{11}$$

In this equation, the propagation term consists of plane wave components (e^{ikz}) of the incident wave and spherical components $\left(e^{-ikr}/_{ikr}\right)$ of the scattered wave. The subscripts ∥ and ⊥ denote parallel and perpendicular polarization. In this work, the distance from the microbubbles to the detector was constant. Thus, the propagation term of equation 11 became a constant. The scattering matrix elements can be evaluated with the following equation[151]:

$$\mathrm{S}_1(\theta) = \sum_n \frac{2n+1}{n(n+1)} \left(a_n \pi_n(\theta) + b_n \tau_n(\theta)\right) \qquad \textbf{12}$$

and

$$\mathrm{S}_2(\theta) = \sum_n \frac{2n+1}{n(n+1)} \left(a_n \tau_n(\theta) + b_n \pi_n(\theta)\right) \qquad \textbf{13}$$

The angle dependent function $\tau_n(\theta)$ and $\pi_n(\theta)$ can be expressed by [151]

$$\pi_n(\theta) = \frac{2n-1}{n-1}\, cos\theta\, \pi_{n-1} - \frac{n}{n-1}\pi_{n-2} \quad \textbf{14}$$

and

$$\tau_n(\theta) = n\, cos\theta\, \pi_n - (n+1)\pi_{n-1} \quad \textbf{15}$$

For this equation, the initial value of $\pi_0 = 0$ and for $\pi_1 = 1$. Which relates to π_n for n=0 and n=1.

The scattering coefficients a_n and b_n were calculated by[151]

$$a_n = \frac{m\psi_n(mx)\psi_n'(x) - \psi_n(x)\psi_n'(mx)}{m\psi_n(mx)\xi_n'(x) - \xi_{n_n}(x)\psi_n'(mx)} \quad \textbf{16}$$

and

$$b_n = \frac{\psi_n(mx)\psi_n'(x) - m\psi_n(x)\psi_n'(mx)}{\psi_n(mx)\xi_n'(x) - m\xi_n(x)\psi_n'(mx)} \quad 17$$

The relative refractive index $m = \mathrm{n_{bubble}}/\mathrm{n_{water}}$, the size parameter $\mathrm{x} = (2\pi\, \mathrm{n_{water}}\, \mathrm{d_{Bubble}})/\lambda$, the particle size $\mathrm{d_{Bubble}}$ was the bubble diameter, and the refractive indices of a micro bubble and water were $\mathrm{n_{bubble}}$and $\mathrm{n_{water}}$, respectively. The symbol, ψ_n, refers to the Riccati-Bessel function of the first kind, and ψ_n' refers to the first derivative of ψ_n. Finally, ξ_n refers to the Riccati-Bessel function of the third kind, and ξ_n' refers to the first derivative of ξ_n.

The scattered irradiance per unit incident irradiance can be calculated with[151]

$$I_{\parallel}(\theta) = |S_2(\theta)|^2 \quad \textbf{18}$$

and

$$I_{\perp}(\theta) = |S_1(\theta)|^2 \quad \textbf{19}$$

In this work, changes to the scattered intensity profile $I(\theta)$ due to varying microbubble diameters ($\mathrm{d_{Bubble}}$) were of interest.

2.7.1.2 Mie scattering in the near field

A spherical particle excited by a plane wave is the theoretical starting point for the derivation of the Mie series. A Mie series can be described as an expansion of plane waves in spherical wave harmonics. The external scattering fields E_{scatt} can be described with the following equation [151]:

$$E_{scatt} = \sum_{n=1}^{\infty} E_n(ia_n N_{e1n} - b_n M_{o1n}) \quad \textbf{20}$$

The subscript *e* and *o* denote even and odd, and the number 1 refers to the first order of the underlying Legendre function. The subscript *n* denotes the n[th] degree of the Legendre function. The spherical wave harmonics M_{o1n} and N_{e1n} can be described by[151]

$$M_{o1n} = cos(\,\phi\,)\,\pi_n h - \sin(\phi)\,\tau h \quad \textbf{21}$$

and

$$N_{e1n} = -\sin(\,\phi)\,\tau_n h - \cos(\phi)\,\tau_n h \quad \textbf{22}$$

The angle dependent functions τ_n and π_n are defined in equation 14 and 15. The magnetic permeability of air ($1.256637 \times 10^{-6} H/m$) and water ($1.256627 \times 10^{-6} H/m$) can be assumed to be the same.

The scattering coefficients a_n and b_n were calculated using equations 16 and 17.

The equations 20 to 22 were applied with the publicly available open source MATLAB library Matscat.[152, 153] Figure 13 displays the amplitude of E_{scatt} (the result of equation 20) in a cartesian coordinate system for a microbubble of 15 µm. Such data arrays were used for the simulations described in chapter 3.1.

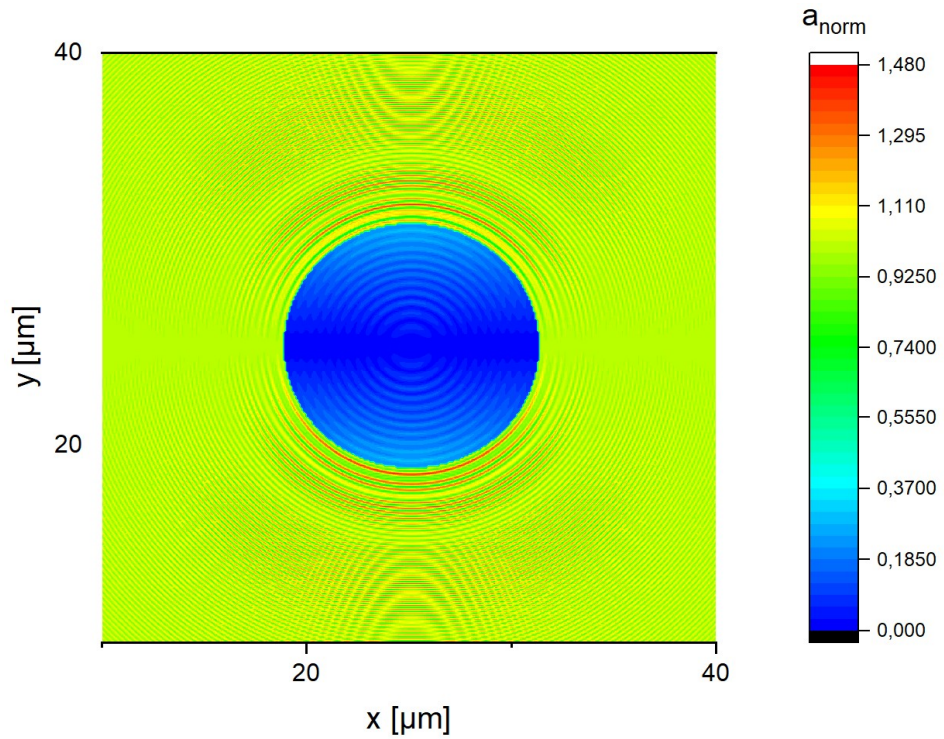

Figure 13. Amplitude of an electric field in object plane in the case of a microbubble (n=1) surrounded by water (n=1.33).

2.7.2 Coherent optical propagation

Despite the fact that the far-field solution (equations 18 and 19) may appear more familiar to most readers, effects of variations in spot sizes, aperture diameter, and elements can hardly be described with the far-field approach. Thus, the solutions of the nearfield calculations (equation 20) were used as a starting point for a wave optical model of an idealized optical system. The optical field in the object plane is described with the phasor notation by

$$E_O(x,y,t) = A_O\ (x,y,t)e^{i\phi_O(x_O,y_O,t)} \qquad \textbf{23}$$

In this equations, the optical field is represented as $E_O(\,x,y,t\,)$, the amplitude (example in Figure 13) as $A_0(\,x,y,t\,)$, and the phase as $\phi_O\ (\,x_O,y_O,t\,)$. The index O refers to the object plane.

In this work, $E_O(x,y,t)$ is equal to zero in regions where the treatment laser does not illuminate the fundus. Element wise multiplication of $E_O(x,y,t)$ with a unity function (or with the beam profile) and the diameter of the spot was used to simulate the electric field in the object plane.

$$E_{Spot}(x, y, t) = E_0(x, y, t) \circ S(x, y) \quad \textbf{24}$$

To transfer E_{Spot} to the sensor plane, E_{Spot} needed to be convoluted with the impulse response function h of the optical system. To increase computational speed, the convolution operation of E_{Spot} and h was performed via multiplication in the frequency domain[154 chapter 6.2.1].

$$G_I(f_{x_I}, f_{y_I}) = H(f_{x_I}, f_{y_I}) G_O(f_{x_I}, f_{y_I}) \quad \textbf{25}$$

$H(f_u, f_v)$ is the coherent image transfer function defined as [154 chapter 6.2.1]

$$H(f_{x_I}, f_{y_I}) = P_{XP}(-\lambda z_{XP} f_{x_I}, -\lambda z_{XP} f_{y_I}) \quad \textbf{26}$$

In the equation, f_{x_I} and $f_{y_I}$are the frequency components in the x and y direction, and P_{XP} is the exit pupil function (circular unity function) of the system. The exit pupil is the object sided image of the aperture stop. The aperture stop is the element which limits the diameter of the light bundle that can propagate through the optical system.

The intensity distribution $I_I\ (x, y)$ in the image plane (sensor plane) is the modulus squared of the field (equation 55). Chapter 5.2 discuss the influence of the aperture stop on the signal acquired by the photodiode.

2.7.3 Laser speckle

2.7.3.1 Fundamentals

Random absorption and scattering events during the random walk of light through tissue leads to spatially varying amplitudes and varying optical path length differences in the object plane. The random component of the optical field in the object plane E_{rand} is defined by the phasor sum of the individual field component k at each point by [155 page 6]

$$E_{rand} = \sum_{k=1}^{N} \left\| a_{O_k} \right\| e^{i\phi_{O_k}} \quad \textbf{27}$$

Imaging a field with random amplitude and phase components (via equation 25) leads to an intensity distribution $I_I(x_I, y_I)$ with bright and dark regions called a speckle pattern. Idealized speckle patterns have the following properties[155 page 8]:

- The amplitudes and phase at a certain point are statistically independent from those at another point (spatially and temporally).
- The amplitudes at a certain point are statistically independent from the phase (spatially and temporally).
- The phases are uniformly distributed from – ϕ to ϕ.

Figure 14 illustrates the values I_I of a speckle pattern originating from an optical field with equally distributed amplitude and phase components (E_{rand}; equation 27).

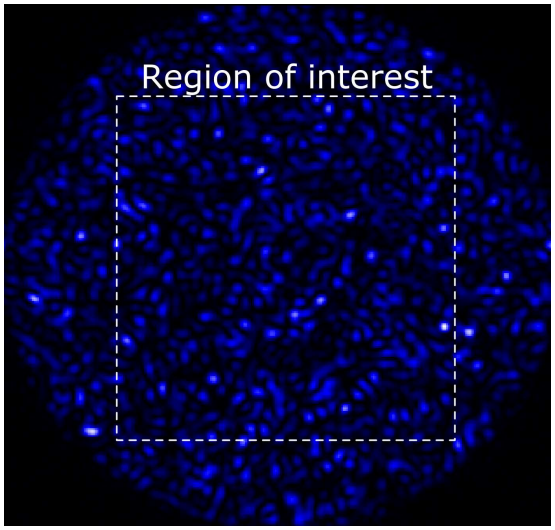

Figure 14. Example of a simulated speckle pattern (via equations 23 to 27). The highlighted ROI is evaluated in the histogram in Figure 15.

In the case of a large number of *N*, the probability density function describing the likelihood of the occurrence of a certain intensity can be described by a negative exponential density function[155 page 28]:

$$p_I(I) = \frac{1}{\{\bar{I}\}} \qquad \textbf{28}$$

A histogram of intensity values within the region of interest in Figure 14 is displayed in Figure 15. The black line represents the negative exponential density function (equation 28). The normalized distribution of intensity values (red bars) of the simulated speckle pattern fits the theoretically expected trend (black line).

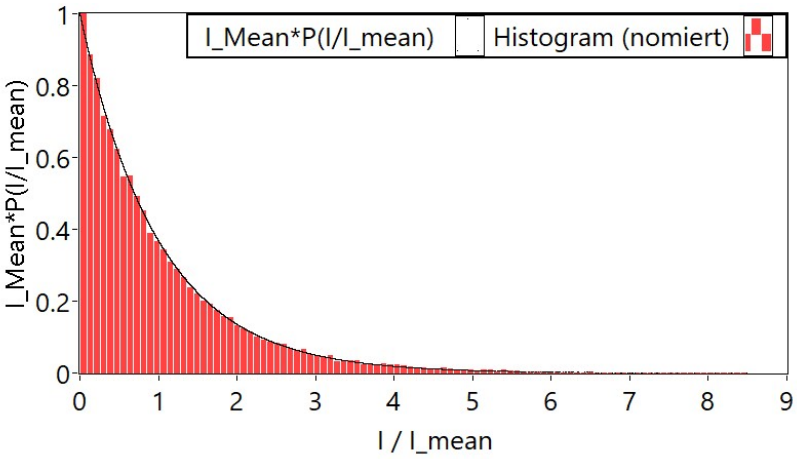

Figure 15. The histogram of the speckle pattern from the ROI in Figure 14 (red bars) shows a exponential decay as predicted by equation 28.

2.7.3.2 Polarization influence on speckle pattern

Light of orthogonal polarization does not interfere with each other. The speckle patterns are also independent of each other. Thus, the resulting intensity of two independent speckle pattern is the sum of both intensities (not the sum of the fields).[155 page 38]

$$I_S = I_1 + I_2 \qquad \textbf{29}$$

As in the previous sections, I_1 and I_2 were assumed to be fully developed speckle patterns. Hence, both have a negative exponential distribution function. The combined distribution function can be expressed as follows[155 page 39]:

$$p_S(I_S) = \frac{1}{\bar{I}_1 - \bar{I}_2}\left[exp\left(-\frac{I_S}{\bar{I}_1}\right) - exp\left(-\frac{I_S}{\bar{I}_2}\right)\right] \qquad \textbf{30}$$

Figure 16 illustrates the probability density function (PDF) for various ratios $r = \bar{I}_2/\bar{I}_1$. The value I_S represents the total average intensity.[155 page 39] If the independent speckle pattern intensities originate from two orthogonally polarized speckle patterns, the polarization ratio Ps can be taken into consideration in the following manner[155 page 49] :

$$p_I(I) = \frac{1}{P\bar{I}}\left[exp\left(-\frac{2}{1+P}\frac{I}{\bar{I}}\right) - exp\left(-\frac{2}{1+P}\frac{I}{\bar{I}}\right)\right] \qquad \textbf{31}$$

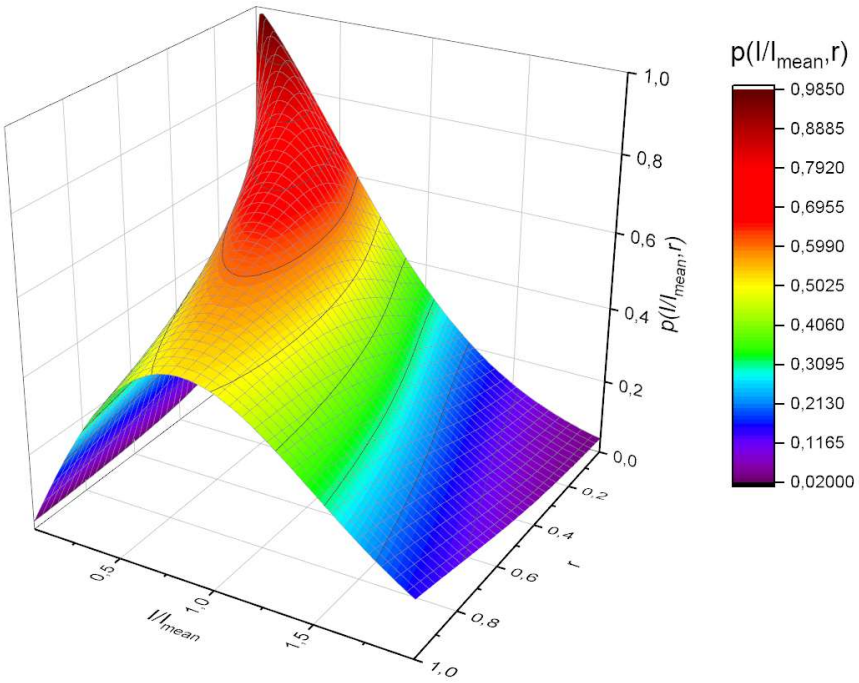

Figure 16. The probability distribution function is depicted as a function ($P(I/I_{mean})$) of the intensity ratio) of two speckle patterns. Two orthogonal polarizations can cause two non-interfering speckle patterns. This needed to be considered by the simulations since the multimode fibers that were used in this work cannot maintain polarization.

As displayed by the graph in Figure 16, the function nearly becomes a negative exponential function when one speckle pattern is dominant ($r = 0.01$). However, the speckle contrast is expected to be highest in this case. In the case of a $50:50$ intensity ratio ($r = 1$), the statistical distribution is likely to change to a Rayleigh distribution.

The optic designs in this work utilized multimode optical fibers. This type of optical fiber does not retain polarization. Thus, the simulation models in this work were needed to be designed in a way that the sum of the two independent speckle patterns could be calculated (details in chapter 3.1).

2.7.3.3 Signal contrast

The systems discussed in this work captured backscattered light with a photodiode. Photodiodes were preferred over cameras to resolve the fast modulations of the backscattered light in the regime of several megahertz. The light of the entire illuminated spot on the retina was guided to the photodiode. Thus, spatial variations within the spot (displayed in Figure 17) did not influence the signal. This design decision allowed the capture of enough light to fit the dynamic range of the photodiode, and it made the optical system more resistant to optical aberrations.

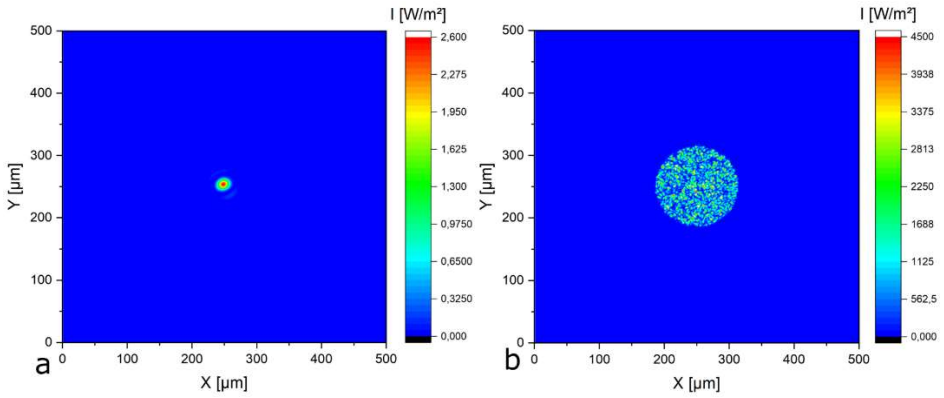

Figure 17. The two images are of the irradiated region as it is imaged on the sensor with an optical system of a) 10 µm spot and 200 µm aperture and b) 128 µm spot and 1000 µm aperture, respectively. Multiple optical designs were simulated to estimate the influence of each design decision.

Integrating the two-dimensional intensity profile results in the laser power received by the sensor, Figure 18 displays a sketch of a possible temporal evolution of the received laser power by a photodiode.

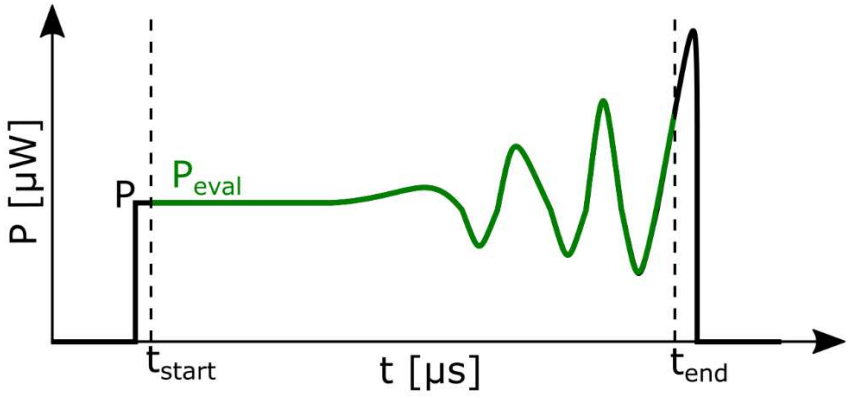

Figure 18. If a non-fully developed speckle pattern changes its pattern on a photodiode, the overall intensity acquired by the photodiode changes. This figure shows a sketch of the laser power received by the laser diode. The green line is the section that is evaluated by the signal processing algorithms presented later in this work.

To quantify the modulations induced by a microbubble, or any other effect, the signal contrast was evaluated. To prepare the calculation of the signal contrast, a region of interest was defined. The region of interest to be evaluated P_{eval} started and ended within the time of irradiation by a laser pulse (displayed in Figure 18).

$$\{ P_{eval}(t) \in P(t) \mid t_{Start} \leq t \leq t_{End} \} \quad \textbf{32}$$

The signal contrast C was defined by the standard deviation and mean:

$$C = \frac{\sigma_{P_{eval}}}{\overline{P_{eval}}} \quad \textbf{33}$$

The influence of aperture size and spot diameter is discussed in chapter 5.2.

2.8 Optical microbubble detection techniques

2.8.1 Detection by back-scattered light (scanning laser)

One approach based on the evaluation of back-scattered treatment light was developed by Alt et al.[156, 157] This research group made use of a scanning mechanism (via an acusto-optic deflector) to achieve a quasi-pulsed irradiation of each region with a continuous-wave laser. The backscattered light was guided to an avalanche photodiode. A pinhole ensured the systems focus to be in the treatment plane by inducing confocality.

Figure 19 displays an irradiated RPE (left) and the acquired photodiode signal (right) from the same working group but without continuous scanning. The same radiant exposure ($86\ mJ/\mathrm{cm}^2$) was applied to all seven regions on the RPE.[158] In this figure it can be observed that in three of the first four cases, an increase in backscattered light was associated with cell death (black regions in microscopy image). The authors described the origin of observed increase in backscattered light via Mie-scattering calculations (far field).[156, 157]

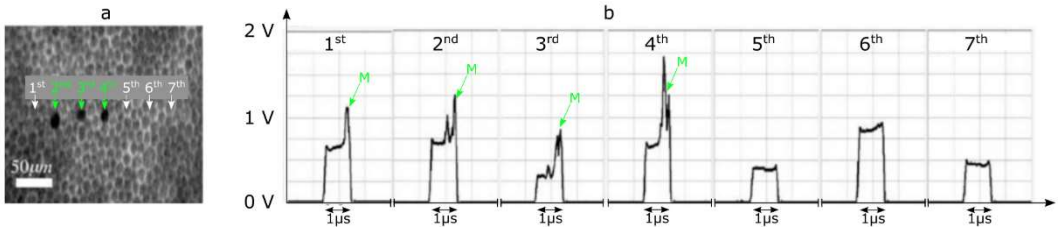

Figure 19. Cell damage (subfigure a; spots 2 to 4; green) is associated with modulations of backscattered light (subfigure b; spots 1 to 4; green M). Microbubbles were detected in regions where no cell damage was observed (1st spot in subfigure a and the corresponding 1st pulse in subfigure b;[158] edited by the author).

Alt et.al. found that safety- and efficiency-defining criteria, such as the selectivity of RPE cell damage and the therapeutic window, depends on the chosen settings (e.g. exposure time)[157 page 86]. Herein may lie a major drawback of this method. In the case of a scanner defect (slower movement or halted movement) during treatment, a higher laser power (several watts) would be applied to a 10 µm region, and this would lead to severe damage of the retina.

2.8.2 Detection by back-scattered light (pulsed laser)

Optical feedback techniques have been found to work with pulsed laser techniques as well.[159] This technique was developed at the Medical Laser Center Lübeck. The first technical realizations led to hardware-embedded techniques that enabled a pulse-wise laser energy increase.[160] The first microbubble detection procedures with this technique were developed using phantom models.[161] These procedures have been improved on to work in ex vivo scenarios.[162]

Seifert et.al. tested several optical designs to identify the most suitable technical realizations.[162] Figure 20 displays the most promising laboratory setup. For this scenario, a frequency doubled Q-switched Nd:YAG-Laser (made by Medizinsiches Laserzentrum Lübeck GmbH) emits a collimated light in the wavelength of 527mn. The laser pulse duration was 1.7 µs and the repetition rate was 100 Hz (10ms repetition rate). A neutral density (ND) filter was used to select the maximum energy that could be applied by the laser system. A PC-controlled shutter used to control the irradiation time, and the shutter was closed either after passing the preselected irradiation time or by the occurrence of a special event (e.g., microbubble detection). Photodiode 1, which had been placed behind the shutter, was used to trigger the acquisition process. A PC-controlled acousto-optic modulator (AOM) was used to change the laser pulse energy of every individual pulse during irradiation. The light was coupled into a fiber with a core

diameter of 50 µm and a numeric aperture (NA) of 0.11. The fiber guided the light to a pankratic optical system. A pankratic optical system is characterized by its ability to change the magnification without changing the location of an object and image. In this particular case, the object was the fiber tip and the image was the spot on the retina. Spot sizes of 50 µm were used most often in the laboratory experiments. Fifty percent of the applied laser light was guided to Photodiode 2 in this setup, and fifty percent of the backscattered light from the retina was guided to Photodiode 3. The voltage of the photodiodes 1, 2, and 3 were then digitized by a PCIe digitizer (Octopus, Dynamic Signals LLC, USA). Data processing took place within 1 ms after the acquisition of each pulse. Thus, an automatic irradiation ceasing was possible with the shutter.

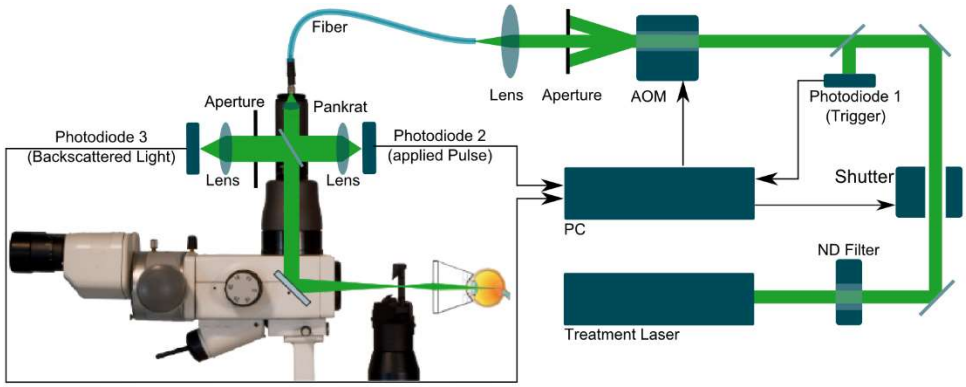

Figure 20. In technical studies from 2011, several scenarios were tested. The best performance was achieved when photodiode 3, which was detecting backscattered light, was placed in front of the fiber, as shown in the figure. In other scenarios, backscattering from the fiber itself created too much noise to evaluate the backscattered light from the eye.

Using the setup displayed in Figure 20, RPE explants were irradiated. The backscattered light was analyzed for signs of random interference patterns and were used as an indirect detection method for microbubbles to estimate the existence of cell damage. Figure 21 displays the results of an experiment conducted with the setup displayed in Figure 20. Figure 21a (left) presents microscopic fluorescent images of irradiated but undamaged regions. Figure 21a (right) shows that there was no modulation of the acquired pulse. Figure 21b (left) reveals that there was little cell damage. Figure 21b (right) shows there were few microbubble-induced modulations. These modulations tend to occur later during irradiation. Figure 21c (left) displays a larger extent of cell damage. Lastly, Figure 21c (right) displays that microbubble-induced modulations occurred earlier during irradiation.

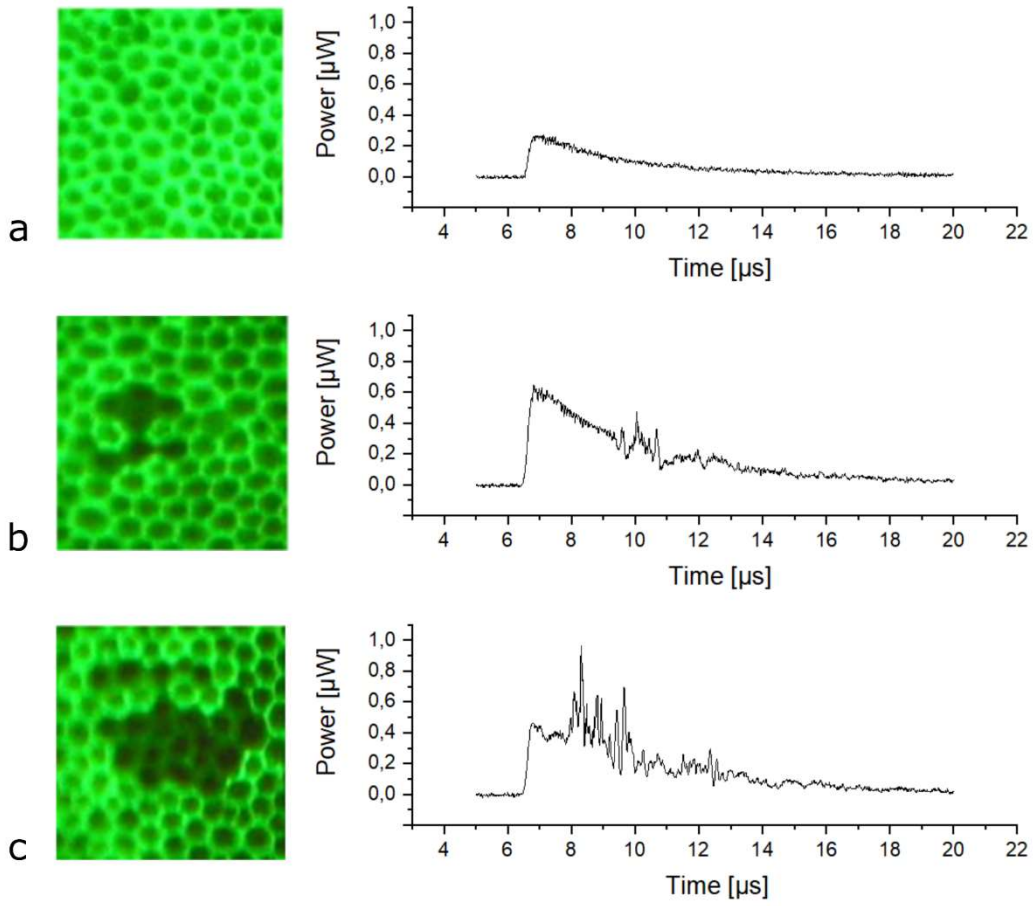

Figure 21. The images to the left display a calcein vitality assay of the RPE. Bright green indicates living cells, and dark regions (only in subfigure b and c) indicate dead cells. The more the pulse energy exceeded the bubble formation threshold, the earlier microbubble-induced characteristics were detected and the longer the modulations last. [162]

3 Material and Methods

3.1 Simulation

3.1.1 Optical field in the object plane

The optical simulations shall provide information about the temporal characteristics of backscattered light from the retina as it would be acquired by a photodiode. This makes it necessary to model the optical field in the object plane, including the influences originating from the microbubble and with influences originating from random scattering processes.

To model the influence of the microbubble, the publicly available MATLAB Library MatScat[152, 153] was applied to solve equation 20 (near field) as well as equation 18 and 19 (far field). This was done for bubble diameter from 10 nm to 15 µm in steps of 10 nm. The initial refractive index of the microbubble was set to one (refractive index of air), and the refractive index of the medium was set to 1.33 (refractive index of water). The results (two-dimensional arrays for amplitude and phase) were stored for quick access.

After the light passed a bubble, it becomes absorbed and scattered in the tissue below (RPE and choroid). Of course, the backscattered light would be influenced by the microbubble as well. Unfortunately, there is no way to model this phenomenon with Mie equations sine the backscatter light is not a plane wave (requirement for Mie calculations) after the scattering events.

To consider that there is backscattered from layers below the microbubble, a field with random amplitude and phase components (E_{rand}) was modeled. E_{rand} consists of a random amplitude a_{rand} varied between 0 and 1, and random phase values ϕ_{rand} varied between 0 and 2π. A uniform distribution was assumed for a_{rand} and ϕ_{rand}. Adding the temporally varying field of the microbubble (E_{scatt}, equation 20) to the constant electric field of the scattering fundus (E_{rand}) led to the following object-field:

$$E_O(x,y,t) = \frac{1}{\sqrt{2}}\left(E_{rand}(x,y,t) + E_{scatt}(x,y,t)\right) \qquad \textbf{34}$$

In the next step, the spot diameter was defined with a circular unity function (or a real beam profile) $S(x,y)$. In the following step, $S(x,y)$ was applied to $E_O(x,y,t)$. At this

stage equations 25 and 26 were applied to calculate the field in the sensor plane. Then, equation 55 was applied to calculate the intensity in the sensor plane.

3.1.2 Simulation process

The optical fibers used in this work did not retain the polarization of the transmitted light. Thus, the intensities of the orthogonal polarized components of light needed to be added (details in chapter 2.7.3.2). At this stage of the simulation, two pairs of random amplitude and phase components had to be loaded. In the next step, the coordinates were initialized. A spatial resolution of 500x500 points was chosen, the spacing was set to 1 µm, and the temporal resolution was selected to be 1ns. With the time coordinates the course of the laser power over time (pulse shape) could be created. Three distinguishable pulses were chosen to be used in this work. One pulse was a rectangular function (Figure 22 green), one was a recorded pulse characterized with a slightly increasing laser power towards the end of the pulse duration (Figure 22 blue), and one was a recorded pulse with unwanted modulations that originated from the laser resonator itself (Figure 22 red).

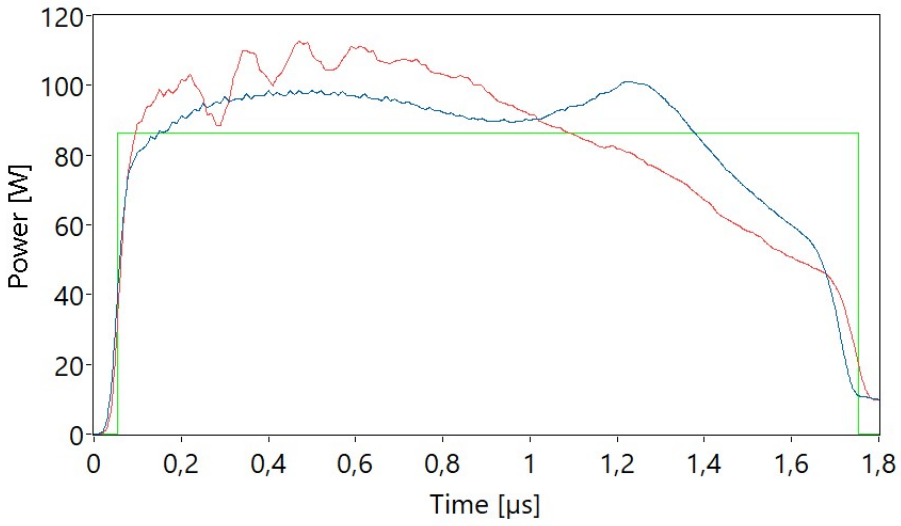

Figure 22. Three laser pulses were used for the simulation tasks. An ideal laser pulse (rectangular function) is shown in green. A typical real laser pulse is shown in blue. A humb at the end of this laser pulse originated from temperature dependencies of the frequency doubling KTP crystal in the Nd:YLF laser. The red line shows a laser pulse with unwanted laser power fluctuations at the beginning of the pulse.

In addition to pulse shape, the two-dimensional beam profile of a laser beam can be chosen, and a circular unity function or real (measured) beam profile can be loaded. For the case of a real beam profile, the hotspots were identified automatically (see Figure 23a, points 1 to 5). By knowing the pixel pitch of the beam profiles (8 µm x 8 µm), the area of a hotspot could be evaluated (see Figure 23b).

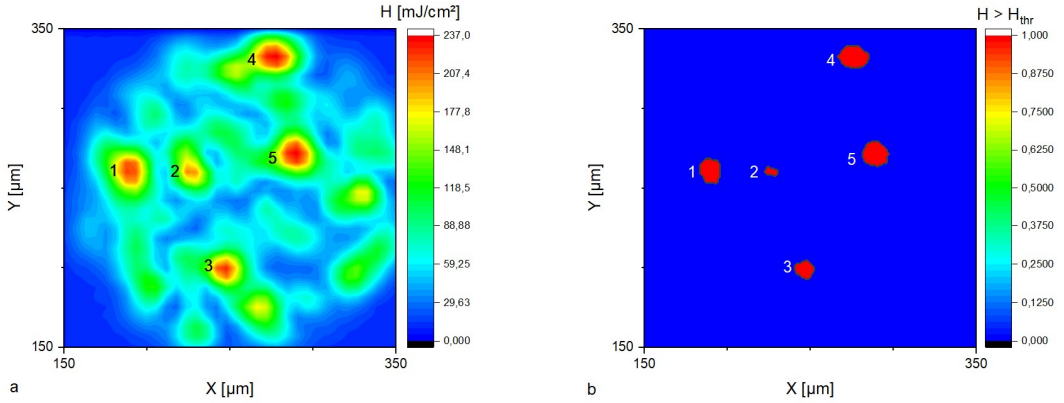

Figure 23. a) Measured beam profile of a fiber with a core diameter of 50 µm and a numerical aperture of 0.11. The beam profile shows hotspots (numbered 1 to 5) that were induced by fiber modes. b) Areas of the hotspots. The areas of the hotspots were used to estimate the volume evaporated by laser irradiation (required for the application of equation 6).

For the next step in the simulation process, the assumption of a 50 nm thick sheet of vaporized liquid was made. The volume of the hotpots' areas and the 50 nm thickness was used to calculate the volume of an initial microbubble. This volume was required to calculate the initial bubble's radius R_0 for the application of equation 6. The maximum radiant exposure within a hotspot was used to make a rough estimation of the temperature increase within a hotspot. To make this estimation, equation 4 was solved for small spot radii in the regime of the hotspot radii (around 5 µm). Changes in the spot diameter had a negligible influence on the results if the condition of heat confinement was given. This was the case for the pulse durations of 1.7 µs that were applied.

Laser power was chosen so that even the smallest hotspot reached the microbubble formation threshold of 150 °C. The temperature of the remaining hotspots was scaled to their respective maximum temperatures. It should once again be noted that the time evolution of the temperature was a very rough estimation, since various conditions like thermal isolation by the microbubble cannot be considered. The resulting increase in microbubble diameter is shown in Figure 24a.

During the simulation process, the respective nearfield solution was loaded for each microbubble diameter for each point in time which was simulated. This nearfield solution was placed (spatially) at the location of a hotspot. Figure 24b displays the amplitudes in the object field at the end of the irradiation (after 1.7 µs of irradiation).

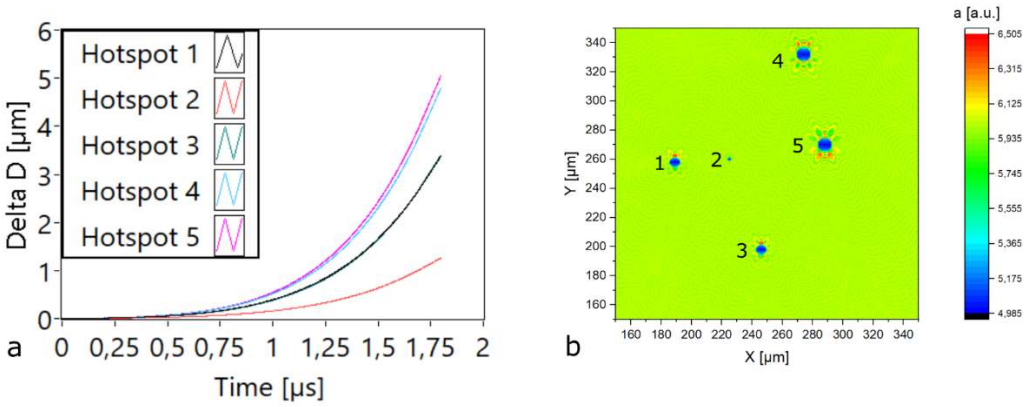

Figure 24. a) Increase in microbubble diameter in the different hotspots according to equation 6. b) Results of equations 20 stacked together at locations of respective hotspots. The amplitude of the optical field in the object plane with microbubble diameters at 1.7 µs (end of the irradiation) is shown.

To test the influence of several design decisions, it was necessary to have reproducible conditions. In such cases a simple circular unity function was used as the beam profile. If a circular unity function was chosen instead of a real beam profile, hotspot 4 (see Figure 24) was placed in the center of the object field.

In the next step, the object field was initialized by combining the randomly phased field with the nearfield solution of Mie scattering equations (application of equations 20 and 27.

After combining E_{Scatt} and E_{Rand} (equation 34), the combined optical field in the object plane can be propagated through the optical system to obtain the field in the image plane where the sensor element is located (equation 25). In all cases, aberration free optics have been assumed.

As mentioned previously, the intensity received by the detector depends on the state of polarization. To account for this fact, the calculations that have been presented to this point were computed twice using two different sets of random amplitude and phase components. The intensities of the two resulting electrical fields in the object plane were then added together. A 50:50 polarization ratio was assumed, and the resulting intensity was integrated over the sensor area. Figure 25 displays the process to simulate the sensor signal with a given set of parameters.

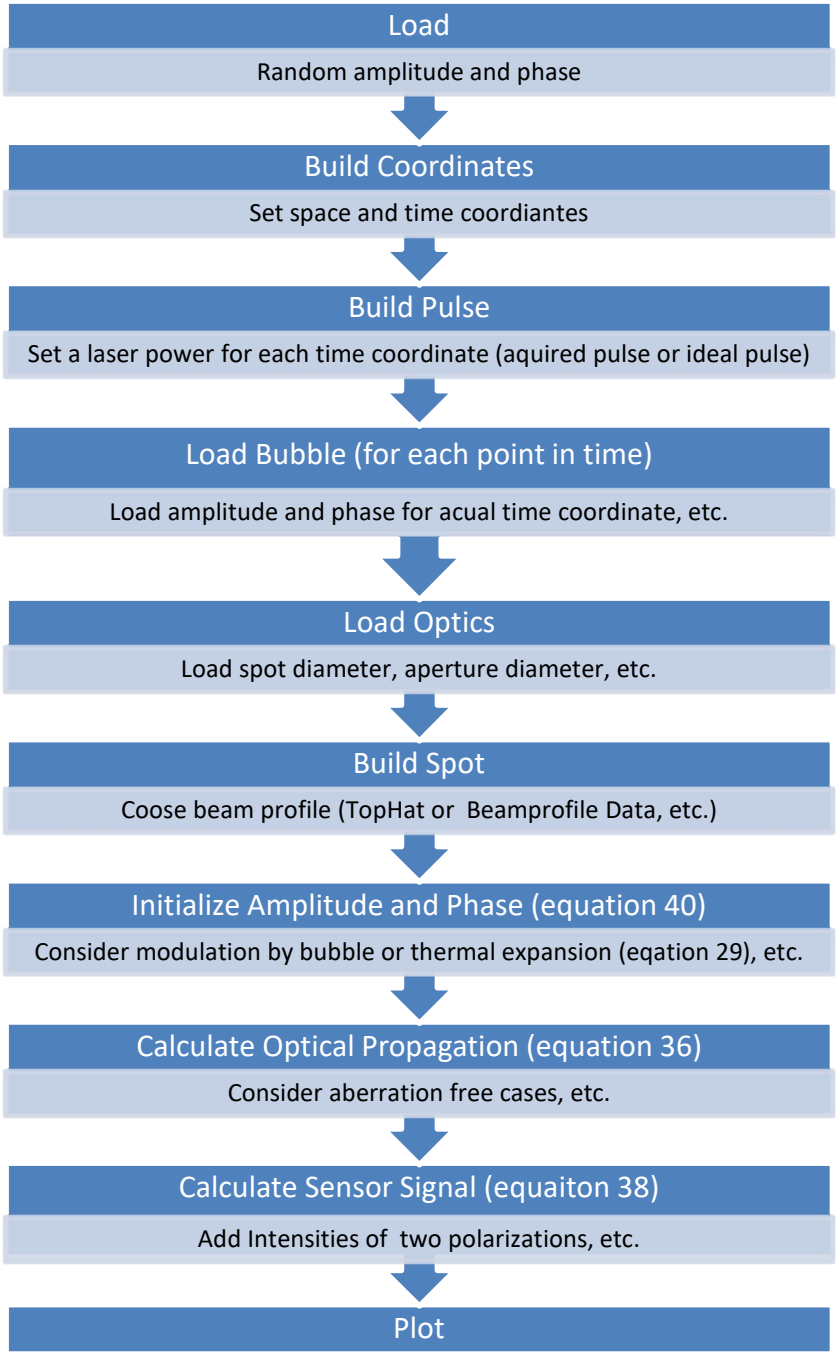

Figure 25 The equations presented in previous chapters were used for the simulation process. Parameters characterizing the optical system, etc. were stored in a SQL-Database. The results of Rayleigh Plesset equation and Mie scattering have been calculated for each microbubble diameter in advance. During the simulation process the corresponding results of Mie scattering equation just needed to be loaded during the initialization of amplitude and phase values. Optical propagation and calculation of the sensor signal was done in each iteration of the simulation process.

In each of the following sections the most important simulation parameters have been listed in a table. Note that numerous other parameters that were constant over all simulations (e.g., spatial resolution of 1 µm, wavelength of 527 nm, 50:50 polarization, etc.) are not listed.

All simulations that are described in the following sections were done with and without the presence of microbubbles or heat induced deformations. This was necessary to differentiate the influence of the random amplitude $a_{rand}(\mathrm{x},\mathrm{y})$ and phase $\phi_{rand}(x,y)$ on the sensor signal from the influences induced by the microbubbles. In practice, the random field components vary from one irradiated region to another. As the effect the random amplitude and phase components had on the acquired signal was of interest, each of the following simulations (process displayed in Figure 25) was conducted with one set of ten different arrays of random amplitudes and phases. The set of 10 different arrays of random amplitudes and phases was the same for all simulations. The results of the influence of random amplitude and phase are presented and discussed in chapters 0 and 5.3.

3.1.2.1 Simulation scenarios

Microbubble diameter: In the fundamentals chapter, it became apparent that the equation describing microbubble growth assumes an already existing spherical bubble as a starting point. This is a problem for the simulation of the signal complex interaction mechanisms like bubble coalescence, changes in light transmission, and heat transfer due to microbubble formation was outside the scope of this work. In this work the existence of a spherical bubble was assumed, and microbubble diameter is calculated with equation 6. The irradiation of the heated surface (RPE) was assumed to be constant over time.

Whether the maximum microbubble diameter has an effect on the acquired signal contrast is of interest to this work. To test whether the microbubble diameter influences the speckle contrast, bubbles with two different radii (2.5 µm and 5 µm) were calculated via the process displayed in Figure 25. Aberration-free optics and a tophat beam profile were assumed. A simulation for each microbubble diameter was performed 10 times with different initial random amplitude and phase values. Changes in the signal contrast were analyzed. Additionally, the far-field solution for Mie scattering calculations are presented for a linearly growing microbubble as well. Results are presented in chapter 4.2.1.

Parameter	Values
Aperture	200 µm, 400 µm, 600 µm, 800 µm, 1000 µm
Spot Diameter	5 µm, 50 µm, 100 µm, 200 µm
Beam Profile	Rectangular top hat
Pulse Shape	Rectangular Function
Bubble Diameter	2.5 µm, 5 µm
Temperature	Not considered

Table 1. Simulation parameters for the examination of the influence of microbubble diameter on the signal acquired by the photodiode.

Aperture diameter and spot diameter: The aperture stop of an optical system limits the size of the beam bundle that can pass through the system. The object-sided image of the aperture stop is the entrance pupil. The size of the entrance pupil defines the opening angle. With an increasing opening angle, the intensity of backscattered light in the image plane increases. In the optical designs discussed in this work, apertures of varying sizes were considered. For this simulation, optical systems with an aperture of 200 µm, 400 µm, 600 µm, 800 µm, and 1000 µm were applied. Aberration-free optics and a top-hat beam profile were assumed. Each simulation of microbubble diameter was performed 10 times with different initial random amplitude and phase values. Changes in the speckle contrast were analyzed. Results and discussion are presented in chapter 4.2.2 and 5.2.

Parameter	Values
Aperture	200 µm, 400 µm, 600 µm, 800 µm, 1000 µm
Spot Diameter	5 µm, 50 µm, 100 µm, 200 µm
Beam Profile	Rectangular, top hat
Pulse Shape	Rectangular Function
Bubble Diameter	5 µm
Temperature Increase	Not considered

Table 2. Simulation parameters for the examination of the aperture and spot diameter on the signal acquired by the photodiode.

Laser Beam Profile: While the beam profile was assumed to be a top hat in previous simulations, in practice the profile was not homogeneous. Simulations were performed with four beam profiles. Aberration free optics were assumed. Changes in temporal signal contrast were analyzed. Eventual effects of a beam profile with non-homogeneous power distribution were investigated in simulations. Results are presented in 4.2.4

Parameter	Values
Aperture	1000 µm
Spot Diameter	200 µm
Beam Profile	Four measured beam profiles
Pulse Shape	Acquired pulse
Bubble Diameter	5 µm
Temperature Increase	Not considered

Table 3. Simulation parameters for the examination of the influence of laser beam profile on the signal acquired by the photodiode.

3.2 Laboratory setup for threshold determination

A laser light source (A.R.C. Laser GmbH, Germany) with a maximum power of 15 W, a wavelength of 514 nm, and a variable pulse duration from 2 µs to 50 µs was used for heating RPE specimens to study the initial cell damage mechanism at different pulse durations. The laser source was a battery of multiple laser diodes. The lights of the multiple laser sources were not coherent with each other. Thus, the light of the combined laser beams showed non-coherent properties. This light was guided to an optical fiber with a core diameter of 128 µm (NA=0.11). The optical system of the slit lamp imaged the fiber tip to an intermediate image plane with a magnification factor of 1. The non-coherence of the laser light led to an absence of interference effects, including hotspots in the beam profiles. In the intermediate image plane, the max-to-mean ratio of the local intensity distribution was 1.2. This value is referred to as the intensity modulation factor (IMF[163, 164]).

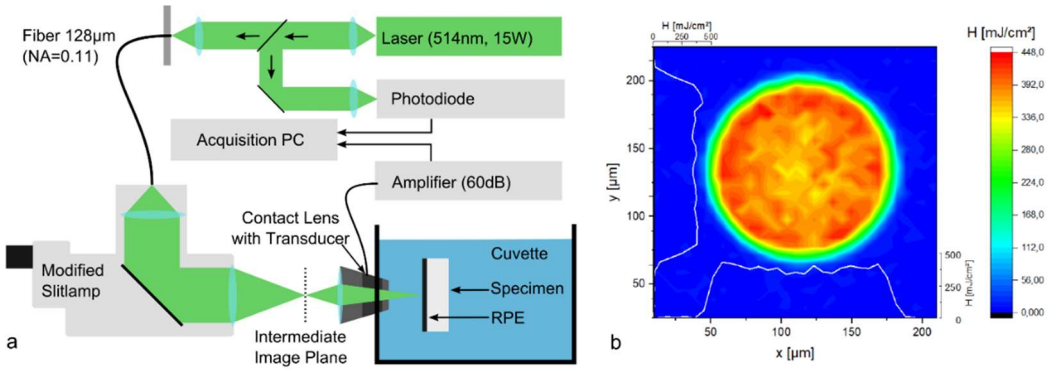

Figure 26. Subfigure a shows the experimental setup (ex vivo). The RPE specimens were place inside a cuvette to be able to control parameters like eye-length and transparency. A photodiode was used to record the applied laser pulse. An ultrasonic transducer was used to acquire pressure transients. Subfigure b shows the spatial beam profile in the intermediate image plane with a max-to-mean ratio (IMF) of 1.2, which is exemplary for a 12 µs laser pulse with a pulse energy of 49 µJ

The IMF was considered at the calculation of radiant exposures. In all experiments, a Mainster contact lens imaged the spot to the RPE. A ring transducer was embedded in the contact lens. The signals from the ring transducer were amplified by a charge-amplifier (Panametrics –NDT Ultrasonic Preamplifier, Olympus). The amplified data was acquired with a digitizer card using a sampling rate of 100 MS/s (GaGe Octopus, Dynamic Signals LLC, USA). These signals were used to evaluate the microbubble formation threshold (details in chapter 3.8.1).

3.3 SRT-systems

3.3.1 Clinic system version 1

The clinic system version 1 is a clinically applicable version of a lab setup developed in 2011 by a team of engineers at the Medical Laser Center Lübeck.[162] For the purposes of this work, the author modified the optical beam delivery path to enable pulse-wise variations of the pulse energy via an AOM (see chapter 3.3.1.1). Furthermore, the author modified the optical system to capture backscattered light (see chapter 3.3.1.1) and implemented software routines to enable the system to treat automatically.

3.3.1.1 Beam delivery path

The treatment light, which heats the RPE to induce microbubble formation (MBF), was generated by a q-switched, intra-cavity frequency-doubled Nd:YLF laser (LU-LQ527-12, Monocrom, Spain) at $527\ \mathrm{nm}$. The maximum laser pulse energy was controlled by a combination of a motor-controlled half wave plate and a polarizing beam splitter. Polarization optics were preferred over neutral density filters due to their higher damage thresholds. A polarization-angle-dependent fraction of the laser light was guided to the primary energy-monitoring component (PDA10A photodiode, Thorlabs). The non-reflected fraction passed through a shutter (SRS 475 shutter with SR470 shutter controller) that operated independently from the computerized components to satisfy safety aspects. The shutter was designed to close automatically 300 ms after a trigger event. With a repetition rate of 100 Hz, 30 pulses were applied. To enable computer-controlled, pulse-wise manipulation of the applied pulse energy, an acousto-optic modulator (R23080-3-LTD, Gooch & Housego, UK) was implemented into the system.

The AOM driver (R21080-2AM, Gooch and Housgo, UK) was connected to a digital-analog converter (Meilhaus Redlab 3110 I/O Box; accessed via LabView). The AOM was aligned in such a way that it guided the 0^{th} diffraction order to the treatment fiber. The 0^{th} diffraction order was preferred over the 1^{st} diffraction order to minimize losses of laser pulse energy. An additional computer-controlled shutter (SH05, Thorlabs) was used to cease the laser irradiation before the 30^{th} pulse, if necessary. With a reaction time of around 30 ms, this shutter was not able to cease the laser irradiation between two consecutive pulses. Thus, it did not serve as the only component for irradiation control in the process of automatic irradiation ceasing. The design decision for this element was made because of its small size (working space was limited). Additional photodiodes (Figure 27., safety reference photodiode and secondary energy monitoring, both PDA10A,

Thorlabs) monitored the light passing through the AOM and SH05 shutters to test their functionality with every applied pulse. The signal of the secondary energy monitoring photodiode was calibrated to the laser pulse energy applied to the eye. The pulse energy meter USB-10MB-HE (Coherent Inc.) was used for this calibration. Graphs showing pulses acquired by the secondary energy monitoring photodiode can be recognized by their power in the watt regime.

A laser diode ($650\ \mathrm{nm}$) was adjusted to be coaxial with the treatment laser light. A red light served as a pilot laser for the treating clinician. This light was coupled into a fiber (core diameter $50\ \mu m,\ NA = 0.11$). Figure 27. displays the setup of the mentioned components, excluding the drivers.

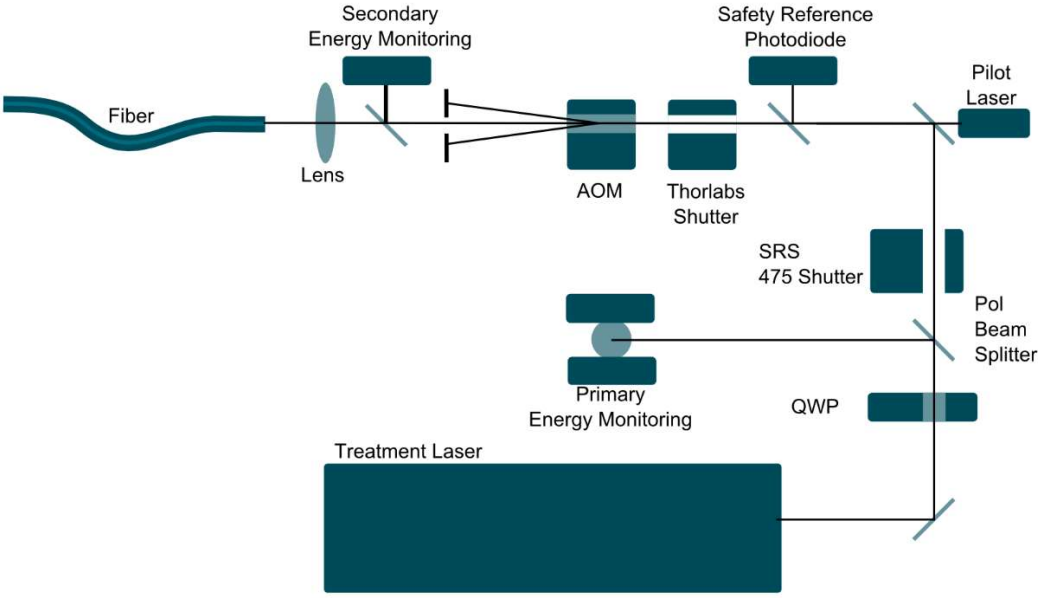

Figure 27. The treatment laser ran constantly so that the primary energy monitoring system could check the maximum laser pulse energy, which was set by a rotating quarter waveplate (QWP). If the shutter was triggered by the foot panel, it opened for 300 ms. A pilot laser (650 nm) was adjusted to be concentric with the treatment laser light. An additional shutter was implemented to cease the laser irradiation in the case of an algorithmic decision (e.g., microbubble detection). An acousto-optic modulator (AOM) was applied to change the laser pulse energy from pulse to pulse within 10 ms. Additional energy monitoring diodes were used to constantly check the functionality of the shutter and AOM.

The fiber guided the light to a zoom element (laser link) mounted on a slit lamp. The laser link was designed to image the fiber tip to an intermediate image plane, and the spot in the image plane was supposed to have a top hat beam profile. This requirement has not been met due to randomly distributed Hotspots in the two-dimensional beam profile. Those hotspots originated from the fiber modes. The peak-to-mean ratio was 3.5 to 3.8.

The spot was imaged to the retina via a Mainster contact lens. The back-scattered light was guided to an observation path via an 80/20 beam splitter. An aperture was used to block unwanted backscattered light from optical surfaces (contact lens surface) and to control the speckle size. An aperture diameter of $1\ mm$ was chosen, and a $14\ mm$ lens was used to couple backscattered light in an additional fiber. Together with the object-sided $70\ mm$ Visulink lens, a magnification of four led to the 300µm observation-spot on the retina. The fiber (core diameter $50\ \mu m$, $NA = 0.11$) guided the light to the acquisition electronics, which are discussed in the next chapter.

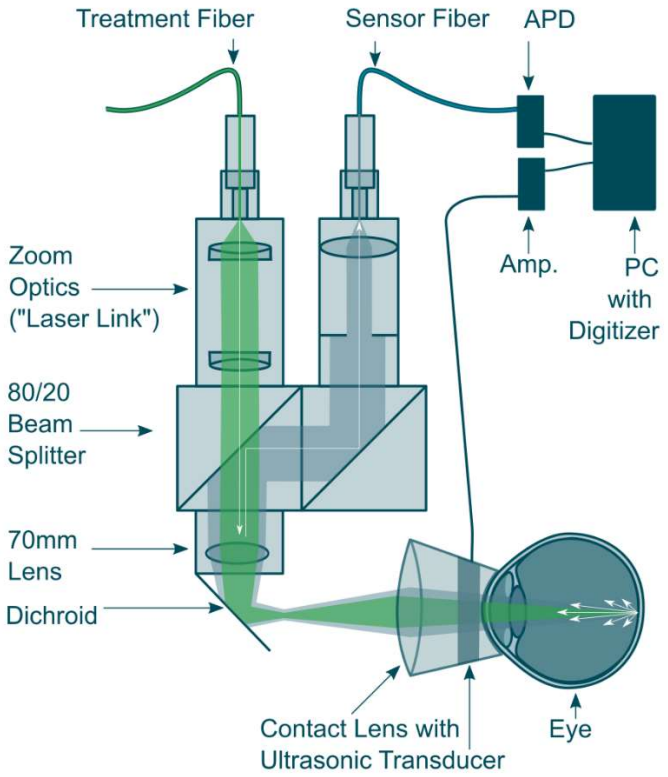

Figure 28. Laser Link: The fiber from the setup presented in Figure 27. was attached to a pankratic imaging system (Zoom Optics). After passing through an 80/20 beam splitter where 80 % of the entering light could pass, an 80 mm lens imaged the fiber tip into an intermediate image plane. This plane was transposed to the retina. As imaging worked both ways, backscattered light also entered the laser link again. Twenty percent of the backscattered light was guided to another fiber that led to an avalanche photodiode. Additionally, optoacoustic pressure transients were recorded by a ring transducer that was embedded in a contact lens. The signal from the ultrasonic sensor was amplified by a charge amplifier. Analog digital conversion took place in a PCIe digitizer that was built using a commercial PC.

3.3.1.2 Acquisition electronics

The optical fiber (Figure 28, Sensor Fiber) led the backscattered light to an avalanche photodiode (APD, APD110A, Thorlabs). The avalanche photodiodes maximum output

voltage was $3.6\ V$ and its overall output voltage noise was $1.5\ \mathrm{mV}$ root mean square (RMS)Its transimpedance gain was $100\ \mathrm{kV/A}$, and the maximum responsivity of the APD sensor was $25\ \mathrm{A/W}$. With these values, the laser power received by the sensor could be calculated. Received backscattered light from the retina is in the rage of microwatts (e.g., Figure 30a).

In order to acquire optoacoustic pressure transients from microbubbles, the acoustic signal was recorded via a piezoelectric element (central bandwidth at 1 MHz) embedded in a Mainster contact lens. Its output voltage was amplified by 60 dB by a charge amplifier (Panametrics –NDT Ultrasonic Preamplifier, Olympus).

The optical and acoustical data were digitized with a $14\ bits$ digitizer (GaGe, Dynamic Signals LLC). Signals were acquired with a sampling rate of 100 MS/s.

3.3.1.3 Software

During the software runtime, which controls the processes mentioned in this paragraph, actions related to the treatment procedure and safety aspects needed to be made within $10\ \mathrm{ms}$. When the digitizer was triggered, the photodiode voltage and OA amplifier voltage were recorded for $100\ \mu\mathrm{s}$. The time, it takes to read out the digitizer card is below $1\ \mathrm{ms}$. The usual time required for algorithmic decision-making is below $1\ \mathrm{ms}$ as well. This left around $8\ \mathrm{ms}$ for adaptions in the control voltage of the AOM. The acquired sensor data (photodiode data and optoacoustic data) was stored for later evaluation and algorithm development. Four different irradiation modes were implemented in the software to enable more complex treatment protocols. Those irradiation modes are explained in the following subsections.

3.3.1.4 Irradiation modes

3.3.1.4.1 Test spot classic and treatment classic modes

In the modes test spot classic and treatment classic, a series of pulses of the same energy were applied. Automatic irradiation ceasing was deactivated in these modes. These modes have two key features that made their application in this work relevant. First, the laser energy deposited into the irradiated tissue was the highest to be achieved with the chosen laser pulse energy. The treating clinician could vary this pulse energy with a hardware switch. The software could only reduce the maximum laser pulse energy selected with the hardware switch. It could not increase this maximum pulse energy. Second, changes in the time evolution of the optoacoustic pressure transient can be

interpreted by a trained observer and the algorithms to evaluate those differences in transients worked reliably under this condition. Thus, those microbubble indicators were used during the first treatments to ensure efficiency the treatment.

The different names (Test spot classic and treatment classic) for these otherwise identical modes exist for improved documentation of the treatment process. The test spot classic mode was applied in a symptom free region in the periphery at the beginning of a treatment while the treatment classic mode was applied during irradiation of diseased areas in the first clinical applications.

3.3.1.4.2 Test spot ramp

The test spot ramp mode is important for the gathering of sensor data in several stages of microbubble formation. It may be applied both to healthy regions (test spots in the periphery) and diseased regions to gain information about differences in the threshold energy for microbubble formation between those regions.

On order to find the threshold for cell damage with one application of a series of laser pulses, the test spot ramp mode makes use of an increasing pulse energy from 10 % to 100 % of the maximum energy. The maximum laser pulse energy was chosen by the clinician. Thirty stepwise increases in laser pulse energy were made without the ability to cease the laser irradiation automatically.

There were three important aspects of this mode. Firstly, the first pulse of a burst is likely to be below the threshold if the maximum pulse energy has been chosen reasonably. Details on how to find a reasonable maximum pulse energy can be found in chapter 3.6.1.2. Second, the pulse energy applied to the tissue was the same as the one applied in an automatic treatment case in which no automatic ceasing was induced. Third, the cell damage induced by a ramp application is likely to be induced by several but not all pulses.

3.3.1.4.3 Treatment ramp

The fourth mode is called treatment ramp. In this mode, the ramping functionality and the automatic irradiation ceasing functionality are enabled. There are two key features in the automatic treatment mode. First, depending on the chosen threshold level for cell damage, only a few pulses (ideally just one) induce cell damage. Second, the irradiation time is reduced. Thus, this mode is the most reasonable for application to treatment spots.

3.3.1.5 RM_{V1} algorithm

The digitized voltage of the photodiode serves as input for an algorithm which was designed to make a binary decision of whether microbubble induced modulations can be found in the photodiode signal. The digitized voltage of the analog digital converter was used without any conversion to the voltage or laser power.

After removing the DC offset from the input signal, a bandpass (Butterworth type) filter with a lower cutoff frequency of 1 MHz and a higher cutoff frequency of 50 MHz was applied. This process not only extracted the microbubble induced modulations but also the rising and falling flanks of the laser pulse. To exclude signal artefacts induced by the rising and falling flank of the laser pulse, a region of interest (ROI) was defined. An integral over the filtered signal ($P_{BP}(t)$; index BP stands for bandpass) within this region of interest was used to quantify the extent of microbubble induced characteristics.

$$I_p = \int_{ROI_{start}}^{ROI_{end}} |P_{BP}(t)|\, dt \qquad \textbf{35}$$

Because of the design of the treatment protocol, the first pulse of a series of 30 pulses was assumed to be below the threshold of microbubble formation. Thus, the I_p value of the first pulse (I_1) represented a reference value for the below-microbubble-formation state. The, I_p values of each pulse *p* were set into relation to I_1.

$$RM_{V1} = \frac{I_p}{I_1} \qquad \textbf{36}$$

The resulting RM_{V1} value was expected to produce values around one in the case of no microbubble formation and values above one in cases of microbubble formation.

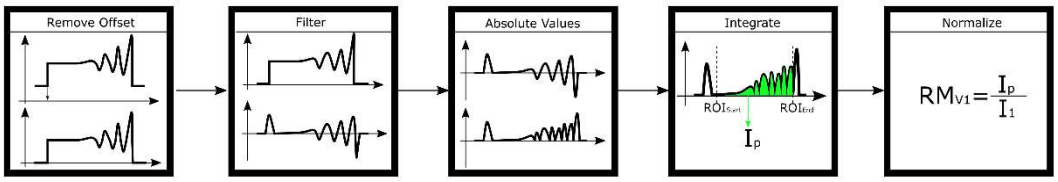

Figure 29. The process flow of RM_{V1} algorithm includes the removal of DC-Offset, filtering to reduce noise, integration of absolute values within a region of interest, and normalization.

The RM_{V1} value is a ratio and does not have any units. Since no prior experience with this algorithm had been gained in vivo, the threshold value for automatic irradiation ceasing

for in vivo experiments was chosen after the irradiation of initial test spots. Figure 29 displays the process flow of the V1 Algorithm.

3.3.2 Clinic system version 3 (R:GEN)

The R:GEN SRT system was developed and built by Lutronic Corp. The author had a consulting role in the development phase of this system. This consulting role included the analysis of (pre)clinically acquired data and the development of microbubble detection algorithms.

3.3.2.1 The V3 system

In this section, public information about the R:GEN system is presented only. The limitation to public information was necessary to avoid non-disclosure agreement violations.

The R:GEN system is based on a frequency doubled Q-switched Nd:YLF laser (527 nm) for treatment. For this setup, the spot size at the retina was 200 µm. The pulse duration was set to 1.7 µs, and 15 pulses were applied with a repetition rate of 100 Hz. A pulse-wise increase of the laser pulse energy (ramp) was implemented. The starting energy was set to 50 % of the maximum energy (E_{max}), and the value of E_{max} was adjusted by the clinician before each irradiation. Since the pulse energy increases linearly, the pulse energy step size was 3.57 % of the maximum energy. All 15 pulses were always applied to each spot, and E_{max} was reached at t[he] 15th pulse.

To guide the treatment light of the Nd:YLF laser to the laser head/slit lamp unit, the light was coupled into an optical step index fiber with a core diameter of 50 µm and a numerical aperture of 0.11. Spatial irradiance variations within the beam profile were measured. The beam profiles had a peak-to-mean ratio of 3.5 (Intensity Modulation Factor, IMF)..

The R:GEN system does not allow for the application of any contact lenses other than those that are designed especially for the system. These contact lenses were developed by Lutronic Corp., and they are designed according to the properties of a Mainster contact lens. The combination of the R:GEN Laser system and the contact lens lead to a spot size of $200\ \mu m$ at the retina (the IMF was 3.5). The R:GEN contact lenses consist of two parts: a lens and a disposable part with an optoacoustic sensor element. The disposable part needs to be connected to the R:GEN system to start a treatment. The acquired pulse was

digitized with a sampling frequency of 100 MS/s and an effective resolution of 14 bits. The acquired sensor data and meta-information, such as pulse energy, was stored. Like the V1 system, the V3 system offers test spot classic, test spot ramp, and the treatment ramp modes to support the same treatment protocols which ensure a maximum of information to be gained about the influence of microbubble formation in sensor data as well as efficiency of treatment and patient safety.

3.3.2.2 RM_{V3} algorithm

At the time of this writing, the algorithm presented in this chapter was not the algorithm implemented in the R:GEN device by the Lutronic Corp. Thus, detailed information can be given without violating any non-disclosure agreements.

Several different algorithms were developed and tested for the SRT systems during the development phases. The algorithm presented in this work was a further development of the algorithm originally created by Seifert et al.[162] The algorithm design was chosen to be as simple as possible to satisfy hardware implementation requirements. The parts of the algorithm presented are the key elements. Safety routines, like the test for an evaluable photodiode-signal and the test for saturation, are not discussed in detail. Additionally, several parameters are mentioned in the following section without being quantified. In the development process, these parameters were evaluated through an optimization process, which is described in chapter 3.11. The algorithm parameters were a result of this work and are outlined in the results section (chapter 4.4).

The digitized photodiode-sensor data delivered by the R:GEN analog digital converter (ADC) was processed after all treatments have been finished. The input of the most relevant processing steps of the algorithm started with input signals, as displayed in Figure 30a. The processing steps performed on these signals are listed as follows:

1 Normalization: The photodiode signal was normalized to its integral. This processing step removed the influence of the laser pulse energy and random fluctuations of its overall intensity. Through this step, the area under the processed signal becomes one.

2 Jitter removal: To be able to address certain regions of interest, the pulse location in the evaluated data set needed to be constant. The jitter-removal process identified the rising flank of the pulse. For pulse identification, a threshold T_{Jitt} needed to be exceeded. The

threshold T_{Jitt} was a product of the mean noise level in a reference region (see Figure 30a) and a factor F_J, and F_J was a variable for the optimization procs.

3 Filtering: For the extraction of modulations, a bandpass filter (Butterworth type) was used. The values of the higher and the lower cutoff frequencies (f_H and f_L) were evaluated through the optimization procs.

4 Summation of a region of interest: The filtered data is referred to as $P(t)$. Examples of $P(t)$ are given in Figure 30b for a pulse above and below the threshold in green and yellow, respectively. When a region of interest (ROI) was defined, modulations could be addressed in the filtered signal and artefacts of the rising and falling flanks were spared. The ROI was defined by its starting point ($\mathrm{ROI_{Start}}$), its endpoint ($\mathrm{ROI_{End}}$), and a threshold value T_{ROI}. Figure 30b illustrates the ROI. It can be observed that the $\mathrm{ROI_{Start}}$ and $\mathrm{ROI_{End}}$ addressed an interval within the pulse but not the edges of the pulse. Thus, the previously mentioned filter-artefacts of the pulse flanks were not considered in further processing steps.

The threshold value T_{ROI} was defined as the product of the noise level of the filtered data within a reference region (see Figure 30b $t_{\bar{p}}$) and a factor (F_{ROI}).

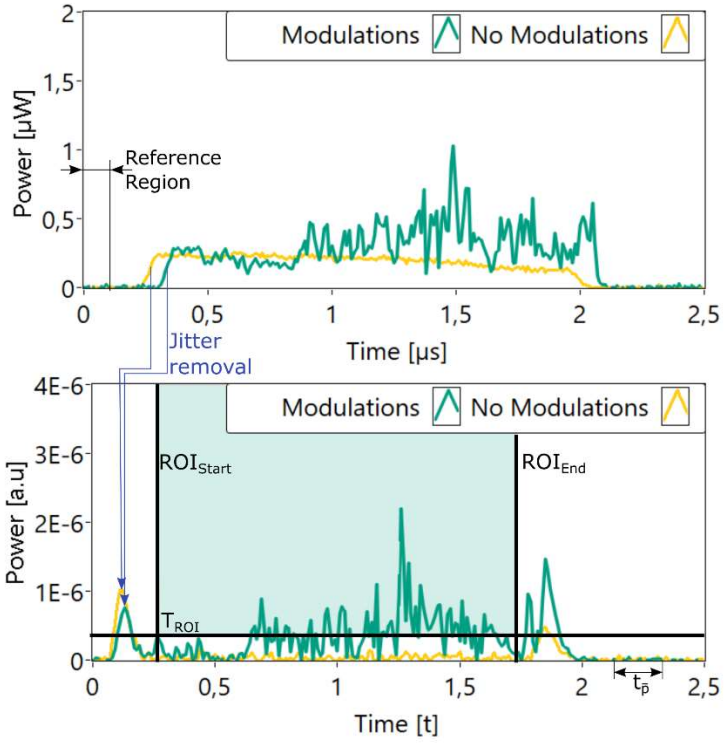

Figure 30. Subfigure a displays received backscattered laser pulses for a scenario with and without micro bubble induced modulation in green and yellow, respectively. The lower subfigure shows jitter removed

and filtered signals, which start at the same point in time. Signal components in the region of interest (section with colored background) were summed up.

The factor F_{ROI} was a variable for the optimization process of the algorithm. The extracted modulations can be found in the subset P_{ROI}:

$$\{ P_{ROI}\,(t) \in P(t) \mid ROI_{Start} \leq t \leq ROI_{End} \cap P(t) > T_{ROI} \} \qquad \textbf{37}$$

Figure 30b illustrates the filtered signals originating from the data displayed in Figure 30a. The green region highlights the threshold ROI. The final RM value is expressed by the sum of the values in this ROI:

$$RM_{V3} = \sum P_{ROI}\,(t) \qquad \textbf{38}$$

Figure 31 displays a simplified flow diagram of the RM_{V3} algorithm.

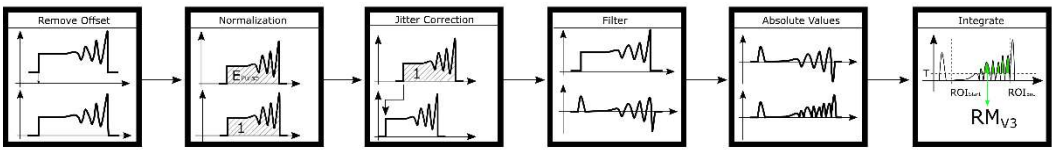

Figure 31. The process flow RM_{V3} algorithm includes DC offset removal, normalization, jitter correction, bandpass filtering. and the integration of the absolute values.

3.3.2.3 Optoacoustic algorithms

The following processing steps made use of the digitized pressure transients delivered by the analog digital converter (ADC) as initial input. Several settings of the algorithm are mentioned in the following sections but not quantified. The values of those settings were found by an automatic optimization procedure (details in chapter 3.11). The exact values are presented in the results chapter 4.5.

Several test and safety processes were executed before the primary microbubble detection calculations began. In cases where digital saturation was detected, a signal was exceedingly low, or signal disturbances were detected by safety routines, the signal was not evaluated.

Non-linearity detection algorithm (NL Algorithm)

If the sensor signal was rated as evaluable, the signal was filtered via a bandpass filter. In addition, the filter settings were automatically optimized. These resulting values are presented in the results chapter.

During the irradiation of a single spot, the laser pulse energy was ramped up. Hence, the laser induced hat in the RPE increases with each pulse. The generated pressure p was a function of the laser pulse energy E and the temperature T dependent Grüneisen coefficient ($p \sim E_n \Gamma(T)$). Thus, the maximum pressure increased with every pulse if a pulse energy ramp is applied. This increase in amplitude which does not contain any information about a microbubble can negatively influence the NL algorithm. Thus, this unwanted increase was eliminated by normalizing the digitized transient P to the laser pulse energy. The energy normalized pressure equivalent δ was evaluated for each pulse.

$$\delta_n = \frac{\int P_n(t)dt}{E_n} \qquad \textbf{39}$$

The ratio of δ_n (δ of the nth pulse) and δ_1 define the NL-value.

$$NL = \frac{\delta_n}{\delta_1} \qquad \textbf{40}$$

The Grüneisen coefficient was assumed to be constant since the low repetition rate of 100Hz minimizes temperature accumulation. Regarding the NL value, it is around one in the case of no bubble formation and larger than one in the case of microbubble formation. Figure 32 displays the flow chart of the NL Algorithm.

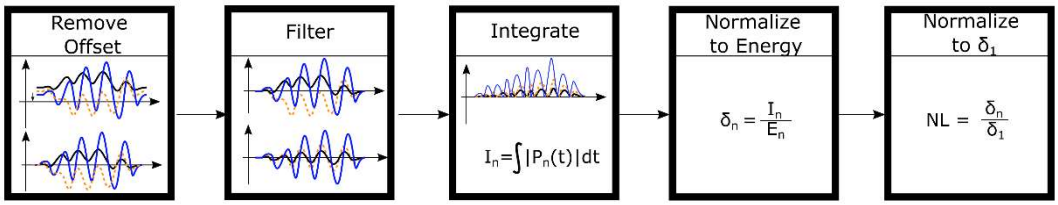

Figure 32. The process flow of OA_{NL} algorithm includes DC offset removal, filtering for noise reduction, integration of absolute values, and normalization steps

Since the presented algorithm makes use of the first thermoelastic transient for its local calibration, it can be speculated that any kind of cell damage (coagulation or microbubble formation) can make this calibration invalid. To work around this risk an additional heuristic has been applied: The NL-value can only be equal or higher than the previous NL value at a particular irradiation. This heuristic has also the side effect, that the optimization procedure becomes more sensitive to cases where an undamaged region is falsely identified as a damaged region (false positive). Since the optimization procedure is very sensitive to false positives, the resulting optima has a low number of false positives,

which was intended. Additional steps to avoid false positives further techniques were presented in later chapters.

Time invariance detection algorithm (TV algorithm)

In the case of laser irradiance below the point of microbubble formation, no significant differences could be observed in consecutive optoacoustic transients, except the laser-pulse-energy-dependent thermo-elastic increase in amplitude.[136] In Figure 33a the transients 1, 8, and 11 display such cases. Microbubbles are a sonic source and the origin of RPE cell disintegration.[26] Consequently, the optoacoustic transients generated by consecutive laser pulses differs in the case of MBF.[136] In Figure 33a, pressure transient 12 differs from the other pressure transients in its time evolution, which is an indicator for microbubble formation.

In previous studies, an individual transient was compared to the mean of all transients after 30 pulses were applied to a spot.[136] This implies that all transients needed to be acquired before the calculation could start. It further implies that microbubble inducing transients also influence the mean value the individual transient is compared to. In the present work this approach has been changed since execution of the algorithm was required after each irradiation (pulse).

In this work, after recording process of each new transient, the whole ensemble of transients of the current irradiation of a spot were considered. Thus, a minimum of 2 and a maximum of 15 transients were used for calculation.

The purpose of the algorithm used in this step was to detect deviations in the course of transients exclusively. No other effect, including other microbubble induced effects (e.g., nonlinear increase in amplitude), were to affect the results of this algorithm. Thus, the potential influence of an increase in amplitude was eliminated through normalization of each transient. As a result, the integral of each transient became 1. A comparison between Figure 33a and b demonstrate the effect of this process. In Figure 33b the transients 1, 8, and 11 have a nearly identical course (time-invariance). Smaller differences between those transients originated from noise.

Transient 12 differed in its course from sub threshold pulses 1, 8, and 11. This indicates a loss of time invariance and is a strong indicator for microbubble formation. Thus, in the second step, the maximum differences ($P_{Diff}(t)$) between all transients in the ensemble were evaluated for each point in time (displayed as pink lines in Figure 33b). The values

of the differences $P_{Diff}(t)$, indicated by the length of the pink dots in Figure 33b, are plotted in Figure 33c.

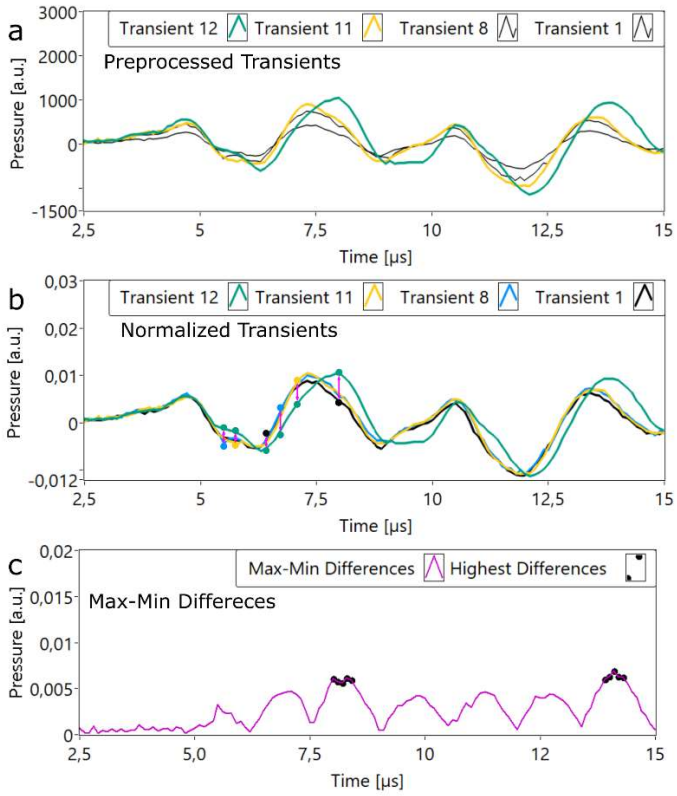

Figure 33. Subfigure a shows preprocessed optoacoustic transients of the same spot irradiation. Transient one serves as a reference for all the following transients. Subfigure b presents the normalized transients. There is nearly no difference between the 8th and 11th transient when the pulse energy dependence is removed. The 12th transient shows the first significant variations as well as a sudden increase in amplitude. Subfigure c depicts the max-min differences of the transients in subfigure b. The mean of the *n* highest differences defined the TV value.

In the next step of the TV algorithm, the i highest differences were evaluated. In Figure 33c, the max-min differences that were used for evaluation are displayed by black dots. The mean of the highest i max-min difference $P_{Diff}(t)$ defined the TV value (value of i is presented in the results chapter).

$$TV = \frac{\sum_i P_{Diff}(t)}{i} \qquad \textbf{41}$$

The value of i was a variable for the optimization process, and it is presented in the results section. Figure 34 displays the flow chart of the TV algorithm.

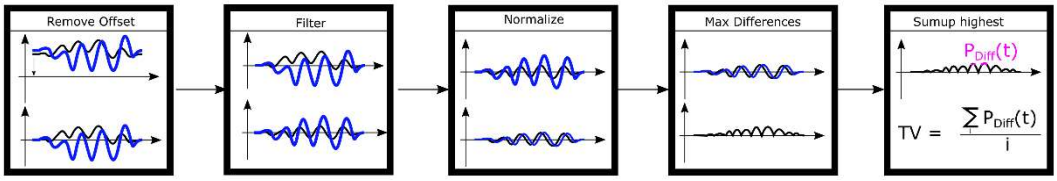

Figure 34. The process flow of the TV algorithm includes DC offset removal, bandpass filtering for noise reduction, Normalization to laser pulse energy, calculation of transient differences and the summation of the largest differences.

3.3.2.4 Baseline methods

Laser pulse energy as baseline

It is good practice to compare a new algorithm being tested to an alternative method (baseline model) that is either the standard of practice or the easiest algorithm imaginable. For the RM algorithm a fix laser pulse energy was used for all patients. To make it the best baseline method, the ROC analysis was done with the laser pulse energy as well. The laser pulse energy that led to the best performance (details about performance measure in chapter 3.10) was then used as the baseline method.

OA Baseline algorithm

In one publication the optoacoustic algorithm used in the R:GEN device is described with the processing steps: 1 Offset removal, 2 Rectification, 3 Summation, 3 Error Check. [165] A normalization process is not mentioned for the optoacoustic signal processing. Thus, absorption differences and transducer angular sensitivity are not considered. [165]. The exact algorithmic hardware implementation by Lutronic is not released in the literature.

It is good practice to compare a new algorithm being tested to an alternative method that is either the standard of practice or the easiest algorithm imaginable. In this work, an algorithm was applied that matches the published processing steps used by the RGEN system. This baseline algorithm (BL algorithm) makes use of the fact that optoacoustic pressure amplitudes tend to be higher in the case of MBF. In order to leverage this phenomenon, the BL algorithm summed up the absolute values of each pressure transient $p(\mathrm{t})$ with a minimum of pre-processing (DC offset removal only). Error detection included the detection of saturated signals, and signal amplitudes were too low to be labeled. This does not need to be identical to the implementation in the RGEN system.

$$BL = \int \left| T_p(t) \right| dt \qquad \textbf{42}$$

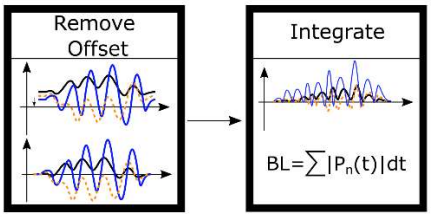

Fig. 1 Processing steps of NL algorithm include offset removal, filtering, rectification, integration, normalization and an error check.

3.4 Study material

3.4.1 RPE explants

Experiments with organ explants contain several uncertainties. Post-mortem changes in optical properties of whole eyes include a steadily increasing opacity of the cornea lens and neural retina (retinal detachment). Thus, ex vivo experiments were conducted with organ explants instead of whole porcine eyes. An organ explant from the RPE to choroid (with the neural retina removed) was used. During the preparation process, RPE examples with low pigmentation were identified and removed.

3.4.2 Cuvette

In experiments for threshold evaluation, the RPE explants were placed inside a cuvette. The distance from the contact lens to the RPE could be varied. By shortening the length of the eye, the spot size could be reduced. A magnification of 1.025 was calculated for a distance of 25 mm from the contact lens to the RPE specimen. The magnification values were evaluated in Zemax.

3.4.3 Rabbit eye

Both threshold evaluations and automatic irradiation ceasing experiments were done with a rabbit model. The transmittance of the anterior rabbit eye media can be assumed to be similar to human eyes.[29] The direct transmittance (the energy in the treatment spot) is around 51 ± 9 %.[166] Considering the fundus (especially retinal layers and RPE cells), Davis et al. have reported that in contrast to human eyes there is no macula in the rabbit retina, but a “sensitive streak” not visible in an ophthalmoscope. A photo of the rabbit fundus can be found in Figure 38. The histologic structure of a rabbit’s retina is

similar to the human retina with some differences in its local thickness. Its general thickness is 120 µm. In the sensitive area ("sensitive streak"), it is 160 µm.[167 page 433] The cells of the rabbits pigment epithelium are irregular in size and arrangement, while the cells in a healthy human retina are hexagonal and regularly arranged. Granules are fusiform in the rabbit epithelium, whereas in the human epitheliusm, they are round.[167 page 435] Regarding the choroid, Davis et al. reported a varying thickness from below 54 µm to 120 µm at the sensitive streak.[167 page 430] The histologic structure is essentially the same as that of the human choroid. The suprachoroidal of the rabbit contains abundant pigment cells so that it is almost solid black in a pigmented eye.[167 page 430]

Depending on the size of the rabbit eye, an area with a diameter of around 7 mm to 9 mm could be used. This region can be used in its horizontal dimension more easily than in its vertical dimension, since the latter option usually requires the rotation of the rabbit along its body axis that could add further complexities regarding variations of the height of the rabbit holder, the slit lamp, or the diagnostic camera (color of FA). Typically, an area with a width of $7\ \mathrm{mm}$ to $8\ \mathrm{mm}$ and a height of $6\ \mathrm{mm}$ to $7\ \mathrm{mm}$ is usable for experimental lesions. For one to separate the ophthalmoscopically invisible lesions in FA images, a minimum spot-to-spot spacing of $400\ \mu\mathrm{m}$ is necessary. This value varies depending on the experience of the treating physician.

3.4.4 Contact lens

A contact lens was used to increase the working distance between the slit lamp and the treated eye, and to keep the eye lids open. In the experiments with the clinic system version 1 and in the experiments with the ARC diode laser (for threshold determination), a Mainster contact lens was used. In the experiments with the RGEN system, the RGEN contact lens (introduced in chapter 3.3.2.1) was used. To avoid spatially unregular refractive index changes induced by air enclosure (reactive index of one) between the cornea (refractive index around 1.3) and the contact lens (refractive index around 1.5), an index matching gel was passed between the cornea and the contact lens. In the experiments described here, Metocel 2 % (refractive index around 1.3) was used. In a (pre)clinical setting the contact lens was placed (with low pressure) on the eye. Excessive pressure would lead to an increasing opacity of the cornea over time.

3.5 Study process for threshold determination

3.5.1 Experimental procedure ex vivo

Organ explants of enucleated porcine eyes consisting of RPE, Bruch's membrane, the choroid, and the sclera were used. The contact lens and the RPE were placed inside a cuvette filled with ringer solution. Pulse durations of 2 µs, 5 µs, 7 µs, 12 µs, 20 µs, 35 µs, and 50 µs were applied. One pulse was applied per spot. The pulse energy was varied with every spot.

The cuvette was used because it offered the ability to vary the length between the eye-sided contact glass surface and the RPE. Thus, the spot-magnification could be varied. For pulse durations of 5 µs, 7 µs, 12 µs, 20 µs, 35 µs, and 50 µs, a spot magnification factor of 1.025 was applied. For a pulse duration of 2 µs, the magnification factor was required to be lowered to 0.325 (65 µm) to increase the radiant exposure at maximum pulse energy.

Calcein viability assays were used to evaluate RPE cell damage. The non-fluorescent dye calcein AM (3 µmol) was applied to the RPE 30 minutes after irradiation for a duration of 15 minutes. The tissue was then mounted on the slide glass, and fluorescence microcopy was performed with the Eclipse Ti-E fluorescence microscope (Nikon Instruments). For the data to be classified as damaged, a minimum of seven cells needed to be damaged within a region that was known to be irradiated. The measurement process was executed by a master student who was supervised by the author.

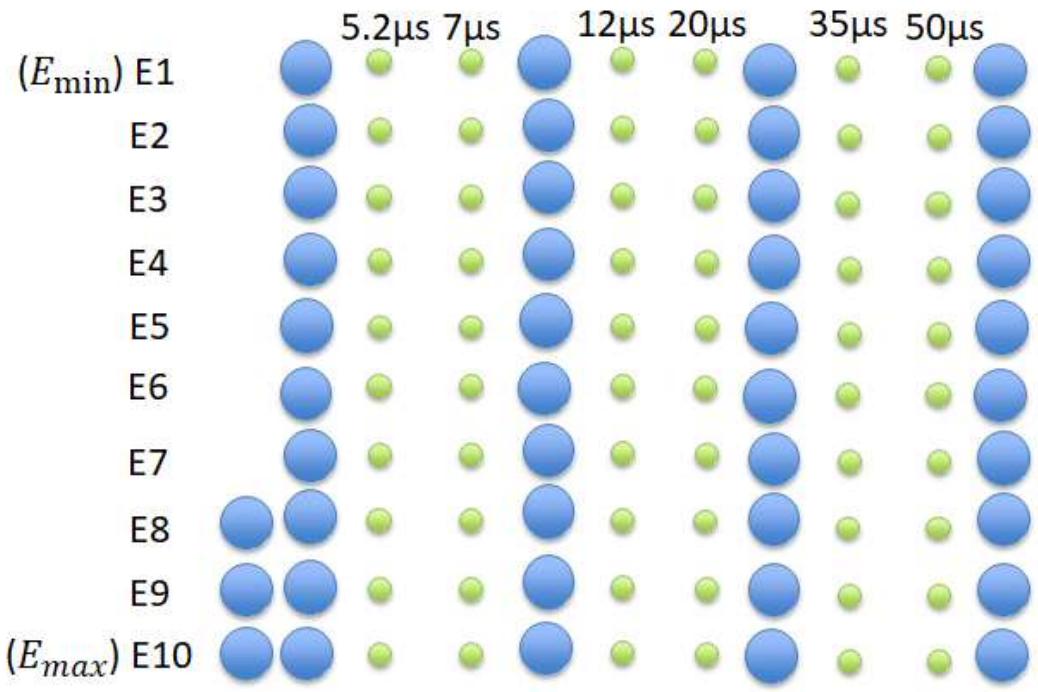

Figure 35. Irradiation pattern used in ex vivo experiments. The pulse duration was changed with each column. The pulse energy was increased with each row.

3.5.2 Experimental procedure in vivo

The experiments were in adherence with ARVO guidelines. Chinchilla gray rabbits were used in this study (permission reference number: V242-12638/2018 (31-4/18)). The rabbits were anesthetized with Ketamine ($25\ mg/Kg$) and Medetomidin (0.25 mg/Kg) via an intramuscular injection. The pupils were dilated with Phenylephrine and Tropicamid, and the ocular surface was locally anesthetized with Conjuncain®. The rabbit was placed in a stabilized position in front of the slit lamp. The contact lens with an embedded ultrasonic transducer was placed on the cornea with an index matching gel (Methocel® 2 %). The eye that was not under treatment was closed to prevent drying.

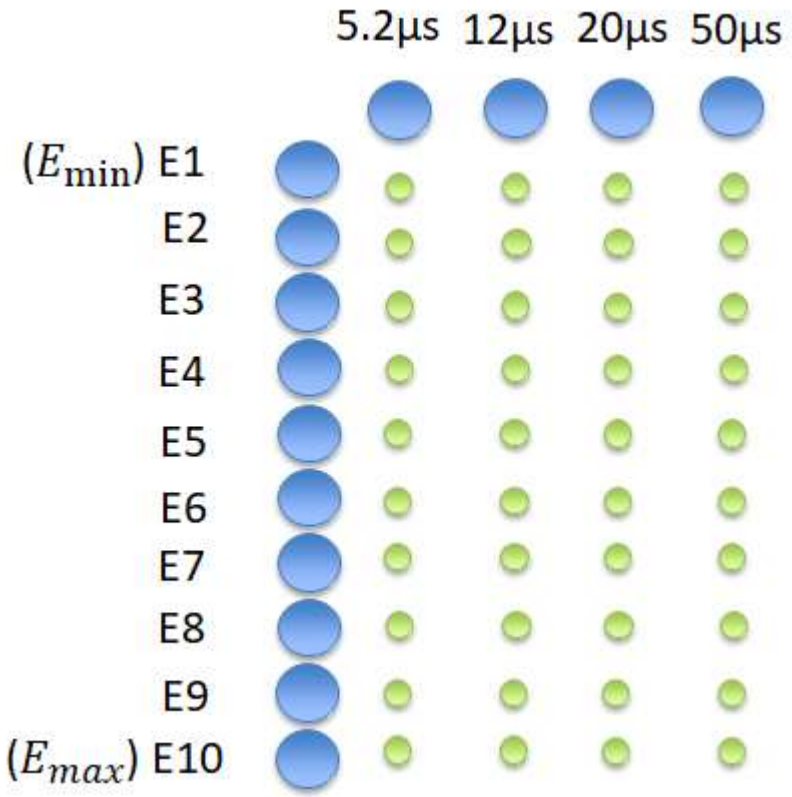

Figure 36. Irradiation pattern used in vivo. Fewer pulse durations were used compared to the ex vivo experiments. This allowed for a repetition of this pattern in each eye. Thus, the number of samples per pulse duration and pulse energy increased.

The anatomical and optical properties of the eye led to a reduced spot size of 85 µm when a Mainster contact lens was applied. Furthermore, a direct transmission of 51 % had been reported for rabbit eyes.[166] These values were considered for the calculation of the radiant exposure ($H_{Cell}, H_{MBF}, H_{Oph}$).

Rabbits of a similar age (nine months) and weight (3 kg) were used in the experiment. An irradiation pattern with predefined radiant exposures and pulse durations was applied to the RPE. The pattern was repeated three times. Marker spots ensured correct spot assignment during the evaluation.

3.6 SRT study process for automated SRT

3.6.1 In vivo validation *with clinic system version 1*

The study was conducted in cooperation with Lutronic Inc., Seoul St. Mary's Hospital, and the Medizinisches Laserzentrum Lübeck GmbH. The clinical coordination and execution of treatments was done by Young Jung Roh MD PhD at the Seoul St. Mary's Hospital. Ethical approvals were granted by the local institutional review board. All treatments and diagnostic procedures were done in presence and with support of the author.

The primary objective was to test the clinic system version 1 for the ability to induce selective RPE lesions. Furthermore, the ability of the system to induce selective lesions through automatic irradiation ceasing was tested.

3.6.1.1 Preparation for the treatment

The rabbits were first anesthetized with zoletil® (Vibrac, Carros, France; 0.2 mg/kg of body weight) and xylazine hydrochloride (5 mg/kg of bodyweight). Indications of waking, such as increased breathing rate and movements of the nose and mouth, were observed frequently during treatment. Cushioning of the rabbit was required to reduce hypothermia, which could influence the anesthesia. Body temperature measurements were performed every 45 minutes. As soon as the rabbit was placed in a holder, pupil-widening eye drops and a local anesthesia were applied to the cornea.

Color images were taken with a fundus camera (e.g., Canon Cr6-45nm non mydriatic camera or Heidelberg compatible fundus camera). These images served as reference images in the classification process after the treatment (details in chapter 3.8). Due to the reduced spot size in rabbit eyes, the lowest laser pulse energy available in the clinic system version 1 needed to be reduced. This was achieved through the appropriate use of the acousto-optic modulator.

3.6.1.2 The treatment procedure

Ten minutes after the injection of the aesthetics, the rabbit was placed in front of a photocoagulation slit lamp. Coagulation marker spots were placed first (Figure 37; red grid). In each rabbit eye, the individual threshold energy for microbubble formation needed to be found. This was accomplished through the application of two rows with spot-wise increasing maximum energy. The first row was treated with the test spot classic mode, and the second row was treated with the test spot ramp mode (Figure 37 first and second row below the marker grid). The raw data was displayed on the monitor after each

irradiation. This allowed the identification of microbubble-induced characteristics in RM and OA sensor data by the author during the experiments.

The pulse energy required to observe the first microbubble induced modulations served as a reference energy. The maximum pulse energy of the test spot ramp and treatment ramp irradiations was adapted after each irradiation. For this adaption, the maximum pulse energy was kept at a level where first pulses with microbubble-induced modulations occurred, around the 15th pulse (out of 30 pulses). Changes to the local pigmentation or a defocused slit lamp could be compensated through this procedure.

During the whole treatment process, a schematic map assigning a spot location to its spot number was drawn to be able to assign each documented spot to its corresponding raw data. Figure 37 displays the grid of spots as it was applied in the in vivo studies.

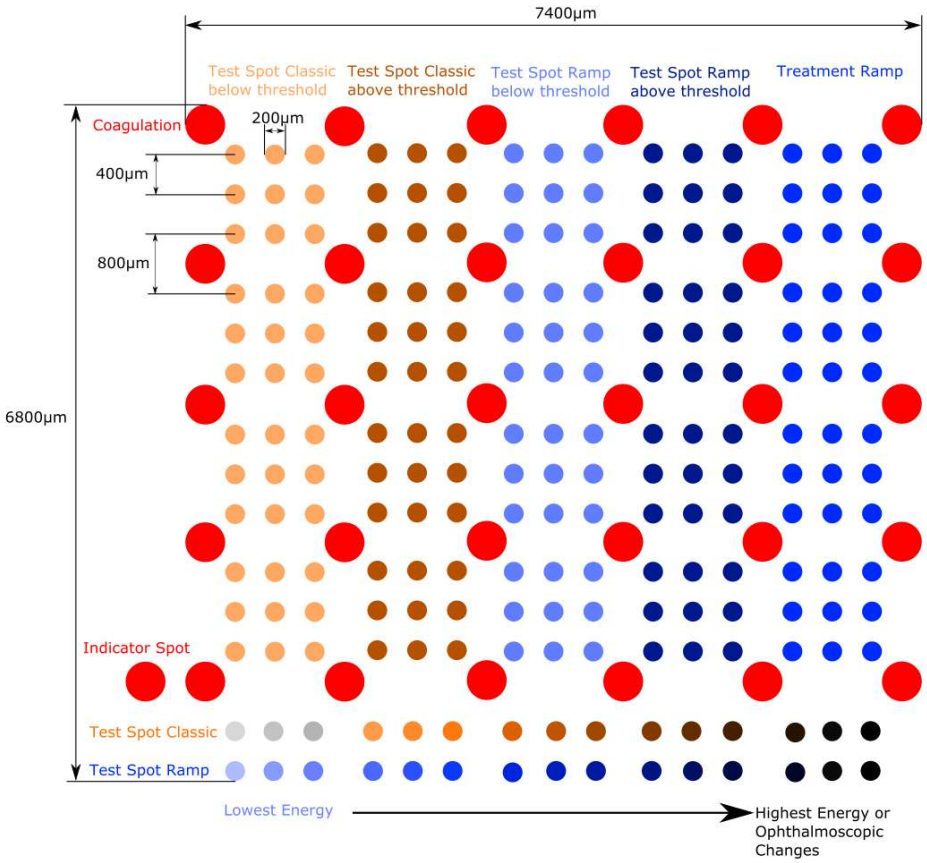

Figure 37. Pattern of irradiated spots in the in vivo study. Different irradiation types (test spot classic, test spot ramp, treatment ramp) allowed for a detailed evaluation of the acquired signals.

3.6.2 Clinical validation with clinical system version 3

Nineteen treatments for 15 eyes of 15 patients (10 males and 5 females; average 54 years old, ranging between 35 and 76 years old) with symptomatic CSCR (11 patients) and DME (4 patients) were performed in this study. The 19 treatments also include four retreatments. The study was conducted at the eye clinics of the University Hospital Schleswig-Holstein (UKSH) Campus Kiel and Hannover Medical School (HMS). The procedures in the study adhered to the tenets of the declaration of Helsinki and its later amendments. The protocol and informed consent forms were compliant with and approved by the local institutional/ethical review boards (ethic committee vote number of HMS: 7393 and UKSH: B577/16). All treatments were done by the clinical staff without the presence of the author.

3.6.2.1 The treatment procedure

Before each treatment, the patients' pupils were widened with a mydriaticum, and a local anesthesia was applied to the cornea. At the beginning of each treatment, test irradiations were applied to spots near the arcades (test spot ramp), and the position and maximum pulse energy were recorded for each spot (Figure 43b). The maximum laser pulse energy (E_{max}) was increased by 10 µJ for every second spot. The lowest E_{max} applied was 30 µJ. This process was stopped as soon as ophthalmoscopically visible effects were observed. The E_{max} value used for the treatment was set to 80 % of the ophthalmoscopically visible spots. The treatment area was done in test spot ramp mode. To ensure selective RPE damage in the treated area and to document the state of the RPE in the test spot area, the clinical staff applied fluorescein angiography (FA) less than one hour after treatment. The acquired sensor data and metadata were saved in the R:GEN system. The data was pseudomized and utilized for analysis after the completion of the study.

3.7 Diagnostic methods

3.7.1 Calcein vitality assay

In the ex vivo experiments information about the state of cell vitality was gained by calcein vitality assays. When calcein AM (calcein-acetoxymethyl ester) gets in contact with RPE cells, it passes the cells' membrane and reacts with esterase in the cytoplasm. The fluorescent molecule calcein is one of the end products of this interaction. Due to its hydrophilic nature, calcein cannot penetrate the cell membrane.[168] Hence fluorescence, observed under the microscope can only originate from intact cells. Fluorescence excitation is usually done at 488 nm (maximum absorption is around

500 nm), and the fluorescence emission maximum can be found around 518 nm. In spots where microbubble formation has been induced, there is usually no cell where the conversion from calcein AM to calcein can take place. Hence, there is a spatially confined absence of fluorescence in damaged regions that can be documented by fluorescence microscopy.

3.7.2 Ophthalmoscopic visibility and fundus photos

In in vivo experiments, ophthalmoscopic visibility describes the subjective impression of a treating physician observing the treated region through a slit lamp. Changes to the fundus that happed immediately with laser irradiation could be associated with thermal or mechanical damage. Changes evolving over time (seconds to hours) are associated with biological reactions to the laser irradiation. The ophthalmoscopic impression of the treating clinician is the only way to gain information about the immediate macroscopic effects if no additional technical assistance is available. Unfortunately, this method did not offer any information about selective cell damage for the conducted experiments. The decision making process was influenced by the optical quality of the anterior eye media (especially the turbidity), and it was not possible to verify the clinician's observation due to the small temporal window during which the decision was made (immediately after laser irradiation or even during laser irradiation). Color images taken after treatment were expected to display discolorations at a much higher number of spots since there was more time for a biological effect to happen (e.g., formation of micro-edema). Figure 38 and Figure 39 display fundus images of a rabbit retina and a human retina, respectively, after SRT treatment. In Figure 38, only the marker lesions are visible. Selective lesions are not visible in either image.

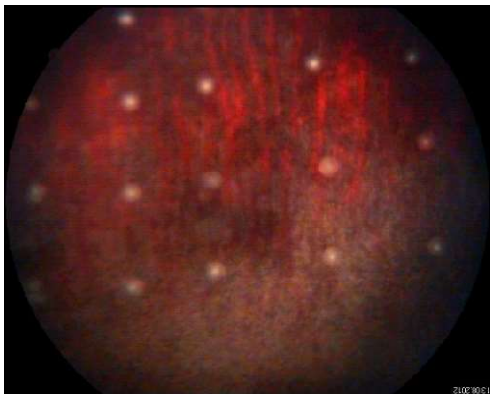

Figure 38. Rabbit retina after treatment. Marker spots are visible only.

Figure 39. Human retina of a CSCR patient after treatment. Selective lesions are not visible.

3.7.3 Fluorescein angiography

Fluorescein angiography is a common method used to gain information about the state of the RPE in an experiment.[169-171] To collect information about the state of the RPE, its blood-retina barrier properties were investigated, which included observing the inhibition of larger molecules to move through the RPE. A fluorescent dye called Fluorescein falls into this category. At a location with defective blood-retina barriers, the dye could only leak from the choroid to the retina. Thus, local hyper-fluorescence indicates RPE damage by disease or laser irradiation. When injected into the patient's blood stream, these resulting markers from the fluorescein dye indicated whether a retinal region had an intact RPE or not. For every imaging technique, the process was influenced by the optical properties of the anterior eye media. Especially in diseased eyes, timing the acquisition with respect to the moment of injection was critical for the acquired images to remain comparable. Sometimes images of the late phase (several seconds to minutes after dye injection) were unevaluable with respect to RPE damage since pathological leakage was excessively dominant.

In the in vivo threshold study, a Heidelberg retina angiograph (Heidelberg Engineering, Germany) was used to acquire the FA images. In the threshold study, a Visucam lite (Carl Zeiss, Germany) was used for FA. In the animal experiments, 0.5 ml of 10 % fluorescein sodium was injected into the ear artery since the veins of a rabbit ear were too small for an intravenous injection. In the clinical trials, an intravenous injection of fluorescein sodium was used.

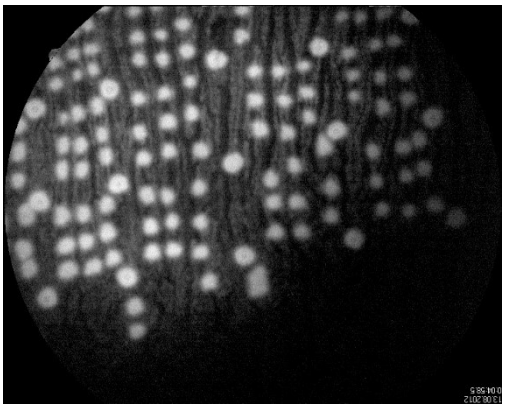

Figure 40. FA image of the same rabbit retina as in Figure 38 after SRT treatment. Selective RPE lesions are visible. SRT lesions are also visible.

Figure 41. FA image of the same test spot region of the human retina in Figure 39after treatment. Selective RPE lesions are visible.

3.7.4 Histological preparation

Three weeks after treatment, the animals were euthanized with an overdose of potassium chloride. The organ explants (retina, RPE, choroid, sclera) was prepared by immersion fixation in 4 % glutaraldehyde, and the anterior parts were removed within 15 minutes. The eyes were fixed for 12 to 24 hours in cool conditions. The eyes were trimmed to block-size after fixation, and the blocks were dehydrated in ethanol. The blocks were cut in into sections of five micrometer thickness, and H&E staining was done on them. These processes were conducted by the colleagues at Yeouido St. Mary's Hospital (The Catholic University of Korea). The author was not involved in the process of making the histologic images.

3.8 Data labeling for classification

3.8.1 Threshold study

3.8.1.1 Labeling criteria

Ex vivo and in vivo data were classified according to microbubble-induced characteristics in the sensor data. These characteristics were extracted by signal processing, including DC-offset removal and filtering. If the pulse duration exceeded 5 µs, two acoustic transients were found in a single raw data acquisition. In the case of no microbubble formation, the starting points of both transients were separated by a value identical to the pulse duration. The pressure amplitudes of the transients were observed to be similar to each other, though the second transient was slightly higher due to the greater temperatures at the end of the irradiation. This data was labeled as OA-negative.

In the case of microbubble formation, the second transient was found to have started earlier. In this case, the second transient amplitude was significantly higher than the first amplitude. This data was labeled as OA-positive.

Presence or absence of microbubble characteristics were identified manually by the author. Figure 42a and b present examples of acoustic transients with and without microbubble formation. The pulse energy applied to the eye up to the point in time of the occurrence of an early second transient was designated as the threshold energy for microbubble formation (Figure 42b purple area).

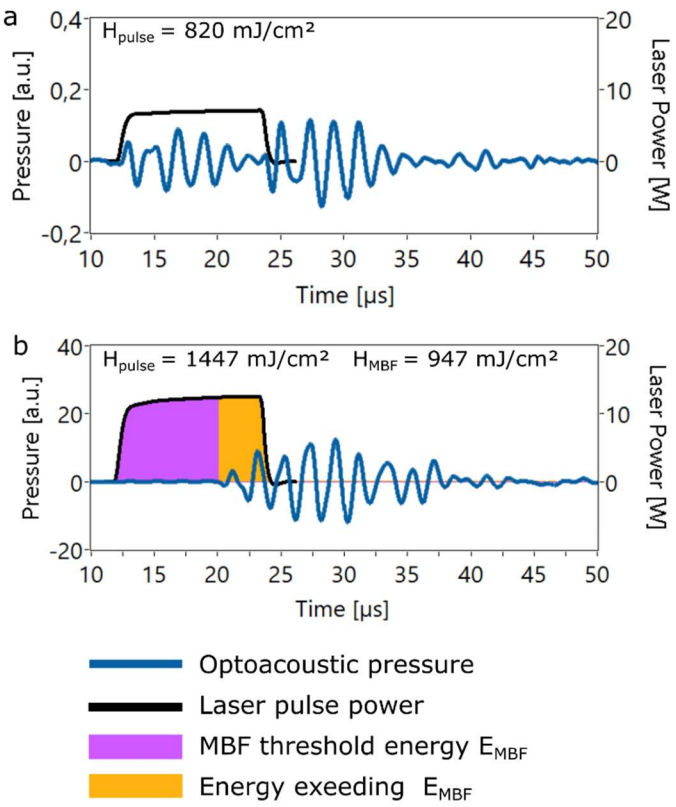

Figure 42. Subfigures a and b depict examples of an optoacoustic signal below and above the threshold for microbubble formation. The received laser pulse is displayed as well. The laser pulse was shifted temporally by the acoustic transition time to make the differences in the time of microbubble formation visible.

In addition to microbubble identification, data was classified according to the state of cell damage. In ex vivo experiments, calcein vitality assays were used. For in vivio experiments, fluorescence angiography was applied to gain information about the presence or absence of cell damage. Data was classified as unevaluable if doubts about the state of cell damage or doubts about the exact spot assignment arose. To be classified as undamaged (FA negative), a retinal region had to be clearly visible and neighboring

spots had to be placed correctly. To be classified as damaged (FA positive), fluorescence had to be identifiable in a region that was known to be treated.

3.8.1.2 Classification based thresholds and threshold ratios

The radiant exposures *H* for each pulse (H_{Pulse}), RPE cell damage (H_{Cell}), ophthalmoscopic visibility (H_{Op}), and MBF (H_{MBF}) were calculated by

$$H_{Pulse} = \frac{E_{Pulse}}{A} \cdot IMF \cdot T \quad \textbf{43}$$

$$H_{MBF} = \frac{\int_{t=0}^{t_{MBF}} P_P(t)dt}{A} \cdot IMF \cdot T \quad \textbf{44}$$

$$H_{Cell} = \frac{E_{Cell}}{A} \cdot IMF \cdot T \quad \textbf{45}$$

$$H_{Oph} = \frac{E_{Oph}}{A} \cdot IMF \cdot T \quad \textbf{46}$$

Laser pulse energy is indicated by E_{Pulse}, the threshold energies for cell damage are represented by E_{Cell}, and ophthalmoscopic visibility is shown as E_{Op} . The laser pulse power is P_P(t), the area of the spot is *A*, the intensity modulation factor is indicated as *IMF*, and the starting time for MBF is shown as $t_{MBF.}$ The direct transmission *T* represents the proportion of the laser light emitted from the slit lamp that reached the target area. The direct transmission was $T = 1$ in the ex vivo experiments performed in a cuvette. A value of $T = 0.5$ was used for rabbits according to findings of former studies and owing to the opacity of the anterior eye media.[166] To obtain an interindividual threshold $\overline{H}$, the mean of the local thresholds H was calculated.

Several ratios *R* of damage thresholds were of interest in the interpretation of the results. The ratio between the threshold radiant exposures for MBF ($\overline{H}_{MBF}$) to that for cell damage ($\overline{H}_{Cell}$) is referred to as

$$R_{MC} = (\overline{H}_{MBF}/\overline{H}_{Cell}) \quad \textbf{47}$$

In the case of simultaneous occurrence of cell damage and microbubble detection, R_{MC} had a value of one. At an R_{MC} of one, it was assumed that initial cell damage was induced by microbubbles. At an R_{MC} higher than one, it was assumed that initial cell damage was induced by other effects, such as heat induced protein denaturation.

In early studies on selective retina treatment, the range from the ratio of the ED50 threshold for cell damage (50 % probability to induce RPE damage) and the ED50 threshold for ophthalmoscopic visibility (50 % probability to induce ophthalmoscopic damage) was used as a practicability measure. A wide therapeutic window (high TW values) was preferable since it indicated that the threshold of RPE cell damage could be exceeded before more collateral damage would be induced to the photoreceptors. In this work, an equivalent to the therapeutic range was evaluated via the ratio of $\overline{H}_{Oph}$ and $\overline{H}_{Cell}$. This equivalent to the therapeutic window is referred to as

$$R_{OC} = \overline{H}_{Oph}/\overline{H}_{Cell} \quad \textbf{48}$$

When microbubble detection systems are discussed, the range from the MBF threshold to the ophthalmoscopic visibility threshold is of importance. This range was quantified with the ratio:

$$R_{OM} = \overline{H}_{Oph}/\overline{H}_{MBF} \quad \textbf{49}$$

The higher this ratio is, the safer the patient is in the case of a false negative decision of the algorithm. However, it need to be pointed out that damage to the photoreceptors may be induced even before the individual H_{Oph} is reached.

For the evaluation of the R_{CM}, R_{OC}, R_{OM}, the data selection process needed to be executed with additional exclusion criteria. Data from a whole pattern were been excluded if H_{Cell}, H_{MBF}, or H_{Oph} were unevaluable. This strict data selection was necessary since eyes with low pigmentation may lead to high FA-visible and OA-positive radiant exposures without producing any ophthalmoscopically visible damage. Moreover, the absence of H_{Oph} in the final evaluation would skew the dataset in a way that falsely reduces the R_{OC} and R_{OM}.

3.8.2 Automated SRT study

The algorithms used to detect microbubbles also served as an indicator of cell damage. To optimize the algorithms presented in chapters 3.3.2.2 and 3.3.2.3 and perform the supervised learning process, data needed to be labeled. Thus, each documented test spot that could be verified by fluorescence angiography received a cell damage label.

Cell damage labeling was done through FA images. Figure 43a displays an FA image taken (days) before treatment. Figure 43b displays a color image taken before treatment with documented spots (notes taken during treatment), and Figure 43c displays an FA image taken after treatment. If there was a mismatch between the documented spots and the FA-visible spots, FA information was labeled "unknown" for all spots of the treatment.

If no hyper-fluorescence was observable in an FA image taken before treatment (e.g., Figure 43a, Spot 12), and if cell damage was observable by hyper fluorescence in an FA image taken after treatment (e.g., Figure 43c, Spot 12) the spot was labeled as "FA-visible." In the case of absence of cell hyper fluorescence, the spot was labeled as "FA-non-visible" (e.g., Figure 43c Spot 1).

If it was not possible to distinguish a selective RPE lesion from its surroundings (e.g., due to intense pathological leakage), all spots of this treatment received the cell damage label "unknown." Likewise, if there were mismatches between the location of a documented spot and visible spots, all spots of a treatment received the label "unknown."

It is important to note that each spot could only have one cell damage classification. In the case of a FA-non-visible spot, all 15 pulses which were applied to a spot were classified as FA-nonvisible. In the case of FA-visible spots, it was not possible to know which pulses contributed to the corresponding visibility. Due to this attribution problem, the pulse with the highest RM or OA value (depending on the algorithm under evaluation) was used for FA-classification.

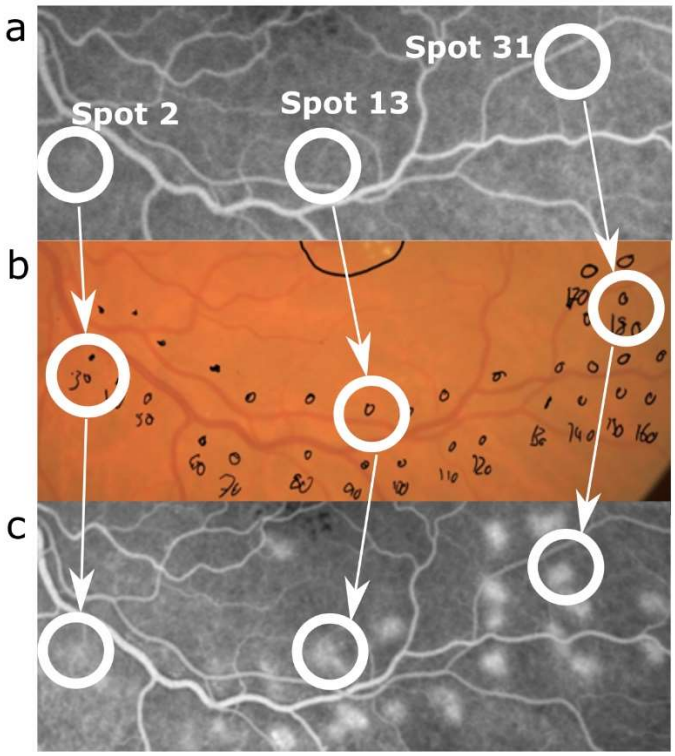

Figure 43. Example of an FA-nonvisible region, an FA-visible region, and an ophthalmoscopically visible region. Subfigure a shows the FA-image taken days before treatment. Subfigure b shows the treatment map and displays the spot allocation in the irradiated test spot region. Subfigure c shows the FA image taken after treatment.

Furthermore, each test spot was assigned to an ophthalmoscopic visibility class. Information about ophthalmoscopic visibility was provided by a note on the treatment maps. In the case of ophthalmoscopically visible spots, the pulses that contributed to the corresponding ophthalmoscopic visibility could not be identified. In these cases, the pulse with the highest pulse energy was considered for ophthalmoscopic visibility classification.

In addition to the spot-wise classification of FA and ophthalmoscopic visibility, each single pulse for each spot was classified according to the (non)existence of microbubble-induced characteristics (modulations) in backscattered light and optoacoustic pressure transients. A classification according to this sensor data was conducted for both the test and treatment spots. In the first step of this classification process, an observer subjectively decided whether data was evaluable or not. If evaluation was not possible (e.g., low by signal-to-noise ratio), the pulse was labeled “unknown.”

Regarding the optical data, modulations could be found on the backscattered pulse. An example of a pulse with no modulations is shown in Figure 44. This data would received the label RM-negative. An example of a pulse with microbubble-induced modulations can be found in Figure 45. This data would receive the label RM-positive.

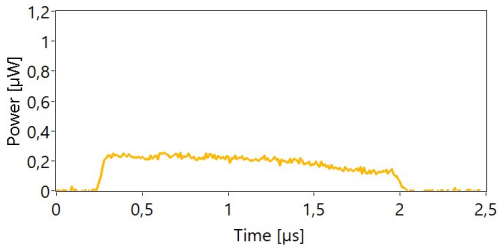

Figure 44. Example of no modulation: The pulse shape is smooth and there are no variations in amplitude other than those caused by white noise.

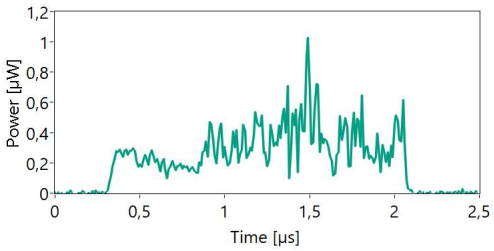

Figure 45. Example of modulation: In this case modulations of the amplitude had occurred.

Regarding the optoacoustic data, both pulse-to-pulse variations of the acquired transients (time-invariance) and sudden increases in the OA-transient amplitude (non-linearity) could only be evaluated by examining more than one transient. Additional transients were needed because neither the researcher nor by the algorithm could classify the first transient.

The OA-algorithms were designed in such a way that all available transients of an (ongoing) irradiation were used for evaluation. The labeling process of pressure transients were considered in this algorithm with the restriction that once a transient was labeled as above threshold, it could not be labeled as below threshold for one of the following transients in the irradiation dataset.

Classification of optoacoustic signals was done for both the test and treatment spots. In the first step of this classification process, the author subjectively decided whether microbubble-induced characteristics could be detected or not. If it was not possible to make a classification (e.g., due to a low signal or noise level), the pulse was labeled “unknown.” Otherwise, a binary classification (OA-positive/OA-negative) was applied. Figure 46 displays the transients without any signs of microbubbles (identical transients). Figure 47 displays a single transient with signs of microbubbles (green transient differs in amplitude and temporal evolution).

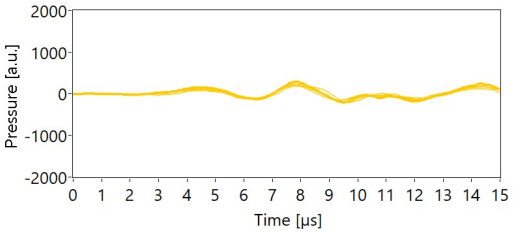

Figure 46. In this instance there were no differences between transients and no sudden increase in pressure amplitude (yellow).

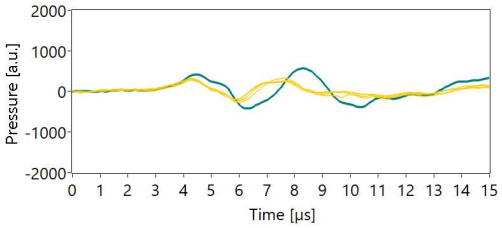

Figure 47. In this case there were no variations between transients and no significant increase in amplitude from transient 1 to 4 (yellow). The green transient differs from yellow transients in amplitude and temporal evolution. This was a sign of the presence of microbubbles.

3.9 Datasets

In statistical evaluations, one single dataset is sufficient (or even necessary) if a mere data summary or a description of a statistical distribution needs to be made. However, as soon as inferential and predictive analyses are required, multiple datasets are mandatory to make the findings generalizable. The easiest test for generalizability is comparing a result of a statistical model with data that was not used in the development process of said statistical model.

This study evaluates algorithms used to predict whether sensor data originated from FA-visible or FA-non-visible regions. Thus, generalizability tests were required and so was the application of multiple datasets. A training dataset originated from test spots that could not be evaluated according to FA imaging (FA-classification unknown) and the treatment spots. Data from treatment spots were labeled with sensor data classification (optical and acoustical) only. The training dataset was the only dataset used for the automatic optimization process.

In the evaluation process, the performance metrics of the training dataset were compared to a cross-validation set (CV set). The data of the CV set fulfilled the same criteria as the training set data. However, none of the data from the CV set were in the training set. There were 15 treatments for 12 patients (nine CSCR, three DME) in the training set, and four treatments of three patients (two CSCR, one DME) in the CV set. Comparisons of sensitivity and specificity values between the training and CV sets offered information about the generalizability of the algorithm performance to detect microbubble-induced modulations in sensor data.

Finally, the data from a test set originated from FA-evaluable test spots exclusively. This data contained all labels (FA visible/non-visible, ophthalmoscopically visible/non-visible, RM positive/negative, OA positive/negative). Data from 11 treatments on 11 patients were included in the test set (nine CSCR, two DME).

3.10 Performance metrics

3.10.1 Sensitivity and specificity

To optimize the algorithms' ability to discriminate between spots with and without laser-induced RPE cell damage, the variables described in chapter 3.3.2.2 (RM), 3.3.2.3 (OA) needed to be adapted for the actual system and input data characteristics. For optimization of the variables for purposes of increasing algorithmic performance, performance metrics were required.

The probability to correctly assign data with RPE cell damage to the class RPE damage is called *sensitivity* (also known as true positive rate or recall). Sensitivity is estimated by calculating the ratio of the number of spots that were correctly estimated to have the label "positive" (i.e., FA visible) and the total number of spots with the label "positive" (i.e., FA visible).

The probability to correctly assign a spot with no RPE cell damage (FA non-visible) to the class FA non-visible is called *specificity* (also known as true negative rate). Specificity is estimated by calculating the ratio of the number of spots correctly estimated to have the label "negative" (i.e., FA non-visible) and the number of all spots with the label "negative" (i.e., FA non-visible).

In this work, sensitivity and specificity were used to judge the performance of the algorithm. The receiver operating characteristic (ROC) curve was arranged as an x-y plot of sensitivity and specificity. Each point in the plot represented a different threshold value. The confidence intervals were calculated according to the Wilson score method with continuity correction.[172] The area under the ROC curve (AUC)[173] was used as the primary value to optimize the algorithm. The ideal threshold was then chosen by a value that merged sensitivity and specificity.[174]

$$h_y = \text{sensitivity} + \text{specificity} - 1 \qquad \textbf{50}$$

3.10.2 Probit analysis

While the ROC curve evaluated the probability of the algorithm to make a correct decision for a given condition, another statistical tool was needed to express the range from FA-visible to ophthalmoscopically visible effects. The microbubble detection system presented in this work was designed to make a binary decision. The RM, NL, and TV values were not designed to scale with the induced damage. This made the RM, NL, and TV values less likely to be applicable as a metric value to define the range from FA visibility to ophthalmoscopic visibility.

Probit analysis is an established method for dose response problems, and it can be used to characterize threshold values for laser induced damage.[175] In the probit approach, the cumulative distribution function of a normal distribution is fitted to the binary cell damage information. The effective dose to achieve a 50 % probability (ED) to induce cell damage is typically used as the threshold value.[175, 176] The ED50 is typically provided in laser pulse energy or radiant exposure.

It is important to know that the code that is used to characterize the probit distribution as well as the code for the fitting procedure varies from implementation to implementation. This can lead to varying estimated ED50 values depending on which evaluation software is used (MATLAB, Origin, etc.). In this work, the probit fit function of MATLAB (Mathworks, USA) was used.

3.10.3 Classical therapeutic window

In previous studies, the metric value (e.g., pulse energy) that led to a 50 % chance of inducing FA-visible RPE damage ($ED50_{FA}$) and the metric value that led to a 50 % chance of ophthalmoscopically visible damage ($ED50_{Oph}$) were used to define the therapeutic window. Since this work was conducted for application in an automatized irradiation procedure, a more conservative interpretation was applied. The lower boundary of the TW was therefore determined by the metric value to achieve an 86 % probability of finding FA-visible lesions ($ED86_{FLA}$). The upper boundary was determined by the metric value to achieve a 16 % probability of finding ophthalmoscopically visible lesions ($ED16_{Op}$). The upper 95 % confidence interval of the lower TW boundary and the lower 95 % confidence interval of the upper TW boundary were used to define the window's width. This width was expressed as a ratio of the upper and lower bounds.

3.10.4 Microbubble detection based therapeutic window

In previous studies, the independent variable of a probit plot was radiant exposure. If the pulse energy for initial microbubble formation was exceeded, there was a rage in which a treatment could still be performed without typical indications of a damaged neural retina. The combination of single-pulse microbubble detection with a pulse energy ramp offered the possibility of identifying a spot-specific reference energy for initial MBF (E_{MBF}) at each spot. Each pulse's energy E_p could be set in relation to such a reference point for initial MBF (E_{Ref}). This reference energy was determined based on the pulse energy of the pulse exceeding the RM threshold for the first time.

$$\delta = \frac{E_p}{E_{Ref}} \qquad \textbf{51}$$

E_{Ref} was evaluated eye-wise, since this value could not be evaluated for FA-nonvisible spots. This value was defined by the mean of the eyes' local E_{MBF} values. The classified data (e.g., FA visibility) and the normalized pulse energy δ were used for the probit evaluations required for the microbubble detection based therapeutic window TW_δ.

3.11 Optimization procedure

For the optimization process, the AUC was used to define the cost function for the optimization algorithm. Together with the learning rate α ($\alpha \in R \cap \alpha > 0$), the AUC defined the cost function J to be minimized by an optimization procedure.

$$J = \alpha \cdot (1 - AUC_n)^2 \qquad \textbf{52}$$

The optimization procedure was a gradient descent process supported by additional routines like feature scaling and automatic learning rate adaption. Through this iterative process, optimal algorithm settings were found. Since finding a global optimum with a single iteration is not guaranteed, this procedure was executed multiple times with random initial starting conditions. In the second step, the Y-index was used to identify the most optimal threshold based on the settings that were evaluated in the optimization procedure.

4 Results

4.1 Threshold evaluation

4.1.1 Ex vivo thresholds

In the ex vivo experiments, 2,310 datasets (cell damage and optoacoustic signal) were obtained. The values for H_{Cell} and H_{MBF} can be found in Table 4. It was found that H_{Cell} was lower than H_{MBF} for pulse durations from 5 to 50 µs. At 2 µs, the threshold values appeared to be almost identical (microbubble delay 1.03). Microbubble delay was found to increase with increasing pulse duration.

Pulse Duration	Cell Damage Threshold H_{Cell}	Microbubble Detection Threshold H_{MBF}	R_{MC}
*2 µs	*249 mJ/cm²	*257 mJ/cm²	*1.03
5 µs	465 mJ/cm²	500 mJ/cm²	1.08
7 µs	505 mJ/cm²	558 mJ/cm²	1.11
12 µs	630 mJ/cm²	727 mJ/cm²	1.15
20 µs	752 mJ/cm²	916 mJ/cm²	1.22
35 µs	955 mJ/cm²	1220 mJ/cm²	1.28
50 µs	1198 mJ/cm²	1700 mJ/cm²	1.42

Table 4. Ex vivo thresholds. Microbubble delay increased with increasing pulse duration. The threshold for microbubble detection had a statistically significant higher threshold than the threshold for cell damage from pulse durations of 5 µs and longer. *At a pulse duration of 2 µs the spot size was reduced to 65 µm, and microbubbles could be detected via amplitude-based information only. In this case, the difference in threshold values was not statistically significant.

To test whether H_{Cell} and H_{MBF}, originated from the same population (null hypothesis) or from different populations (alternative hypothesis), a t-test was applied. A *p* value of 0.01 was defined to be significant. This criterion was exceeded at pulse durations of 5 µs, where a *p* value of 0.003 was achieved.

To evaluate the pulse duration of 2 µs, a total number of 232 spots were analyzed. At this pulse duration the *p* value was larger than 0.01. Based on this information, it can be

theorized that microbubble formation and cell damage have the same threshold value and that the difference of 8 mJ/cm² (effect size) was induced by mere statistical fluctuation. It should be noted that it was not possible to identify the point in time of microbubble formation at a pulse duration of 2 µs because the optoacoustic signal component of the thermoelastic expansion was still present when microbubble formation took place. Microbubble detection was realized by evaluating the maximum amplitude only.

4.1.2 Extrapolation of threshold values

Even though microbubble induced optoacoustic pressure transients can become significantly higher in amplitude than thermoelastic pressure transients, the difference may not be very pronounced just above the threshold of microbubble formation. This possibility would make a reliable microbubble detection at a pulse duration of 2 µs more difficult. At a pulse duration of 50 µs, the number of evaluable samples decreases to just six spots, and the evaluated mean value is less certain. Thus, the data gathered during the interval from 5 µs to 35 µs was the most reliable.

In the 5 µs to 35 µs interval, the threshold values for cell damage and microbubble formation were interpolated with the exponential fitting function $H = A\,\tau^{1/n}$. The parameters for cell damage were $A_{Cell} = 249.38$ and $n_{Cell} = 2.68$. Parameters for MBF were $A_{MBF} = 234.45$ and $n_{MBF} = 2.18$. The fitted curves remained within the 95 % confidence intervals of the fitted points (Figure 48). The curves intersected at $\tau = 2.06$ µs and at a radiant exposure of $327\ \mathrm{mJ/cm^2}$. A comparison between cell damage thresholds and optoacoustic microbubble detection thresholds demonstrated that the microbubble delay would increase with an increasing pulse duration.

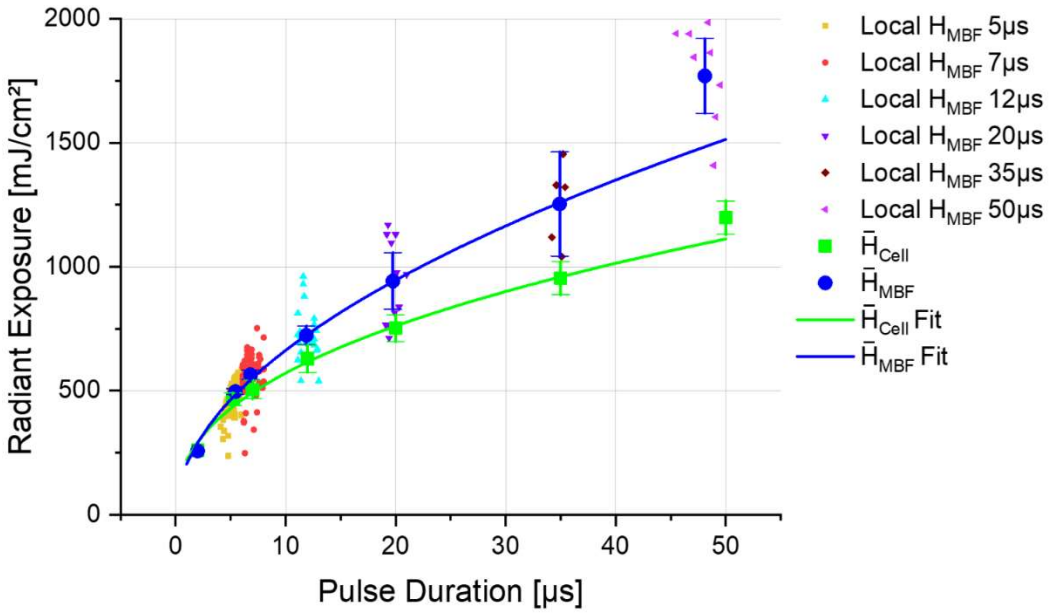

Figure 48. Threshold radiant exposures over pulse duration. The points indicate local H_{MBF} values used for the calculation of the interindividual $\bar{H}_{MBF}$ value. The larger points with error bars display $\bar{H}_{cell}$ (green rectangles) and $\bar{H}_{MBF}$ (blue dots). The error bars show the 95 % confidence interval.

4.1.3 In vivo thresholds

Overall, 2,329 datasets were acquired from irradiations of 11 rabbits. The values for H_{cell} and H_{MBF} can be found in Table 5. As in the ex vivo experiments, H_{cell} was lower than H_{MBF}. In Figure 49a an exemplary color fundus image, a FA image are displayed witch the corresponding optoacoustic pressure transients.

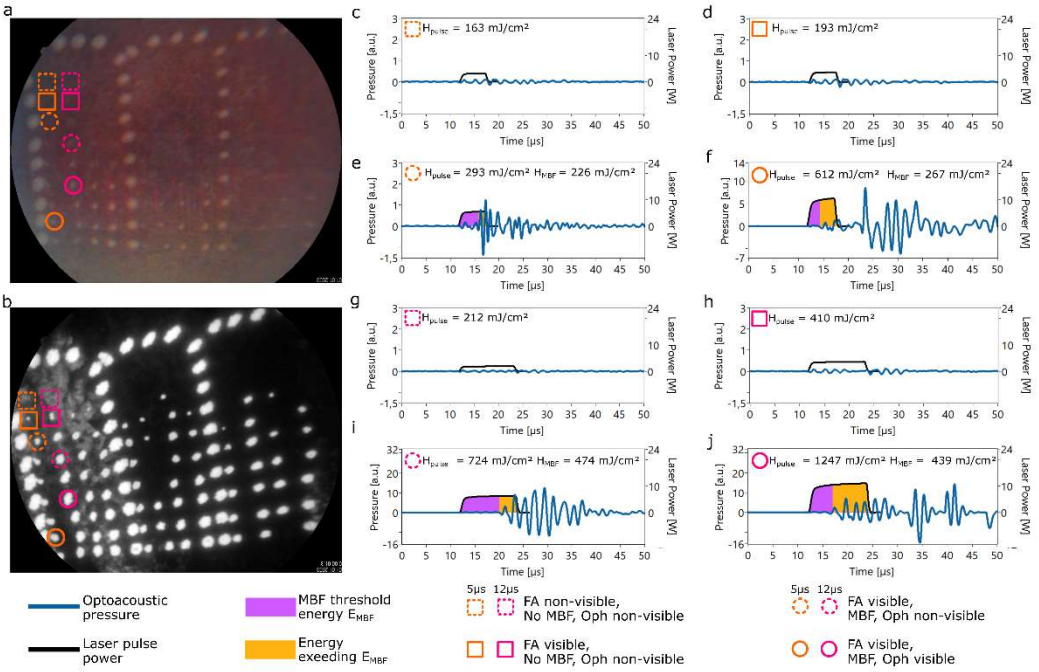

Figure 49 a)Fundus and b)FA image. Regions of identical cell damage are highlighted with colored symbols. Rectangles with dashed lines highlight undamaged regions. Rectangles with solid lines highlight regions with detectable RPE damage (hyper fluorescence in FA images). Rings with dashed lines highlight regions with initial microbubble detection. Rings with solid lines highlight regions with ophthalmoscopically visible effects (during treatment). The subfigures c to j show the optoacoustic pressure transients (blue) and the laser pulses (black lines). The symbols plotted in the upper left of each graph shows which region of the retina (subfigure a and b) was irradiated while the signals were recorded.

The threshold value for microbubble formation H_{MBF} was evaluated based on the mean of the threshold radiant exposures in an interval around the pulse duration of interest (5 µs, 12 µs, 20 µs, and 50 µs). It is important to note that there were no pulses with pulse durations above 50 µs. Thus, the radiant exposure thresholds of 50 µs can be assumed to be underestimated. This is has been accounted for in Table 5 with signs indicating that a value can be larger or smaller than calculated.

As in the ex- vivo experiments, R_{MC} has been found to increase with increasing pulse duration. R_{OC} appeared to be stable around a value of two. R_{OM} has been found to decrease with increasing pulse duration.

Pulse Duration	Cell Damage H_{Cell}	Microbubble Detection H_{MBF}	Ophthalmoscopic Visibility H_{Oph}.	R_{MC} H_{MBF}/H_{Cell}	R_{OC} H_{Oph}/H_{Cell}	R_{OM} H_{Oph}/H_{MBF}
5 µs	239 mJ/cm²	344 mJ/cm²	554 mJ/cm²	1.4	2.3	1.6
12 µs	545 mJ/cm²	606 mJ/cm²	1019 mJ/cm²	1.1	1.9	1.7
20 µs	573 mJ/cm²	840 mJ/cm²	1215 mJ/cm²	1.5	2.1	1.4
50 µs	1030 mJ/cm²	1732 mJ/cm²	2142 mJ/cm²	> 1.7	2.0	< 1.2

Table 5. In vivo thresholds values for cell damage, microbubble formation, and ophthalmoscopic visibility. While microbubble delay increased with increasing pulse duration, the therapeutic window appears to have been constant. The safety range decreased with increasing pulse duration.

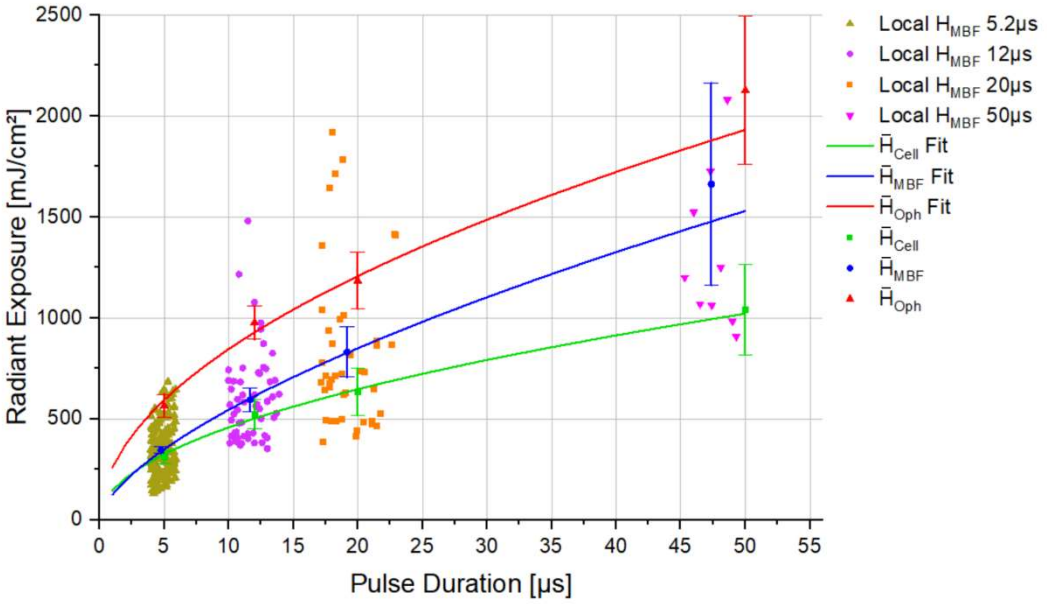

Figure 50. Threshold radiant exposures over pulse duration. The small dots represent local H_{MBF} values of individual spots. The points with error bars display interindividual (mean) threshold values of FA visible cell damage (green rectangles), MBF (blue dots), and ophthalmoscopic visibility (red triangles). Lines show a fit function.

4.2 Simulation of acquired signals

The following chapter contain the results of the simulation process which was used to evaluate which influence the initial part of microbubble expansion has on the signal contrast under the assumption of coherent imaging. With the only exception of the far field solutions (first part of chapter 4.2.1), the processing chain displayed in Figure 25 was used to generate the graphs in the following sub-chapters. The varying inputs to this processing-chain is presented in chapter 3.1.2.1. The effect of the bubble diameter, aperture and spot size, random amplitude and phase, and beam profile is presented.

4.2.1 Bubble size and pulse shape influences

The far-field solution for the scattering characteristics for microbubbles the size of $1\ \mu m$, $2\ \mu m$, and $3\ \mu m$ are displayed in the subfigures a, b, and c in Figure 51. Forward-scattering was dominant, and the backscattered fraction was less than 1 % of the scattered light. The amount of backscattered light tended to vary with bubble size. A linear increase in bubble size led to an modulation of the backscattered light. Subfigure d of Figure 51 displays the fraction of backscattered light of a linearly increasing microbubble. It can be observed that the amplitudes of the oscillations increased when the microbubble diameter also increased.

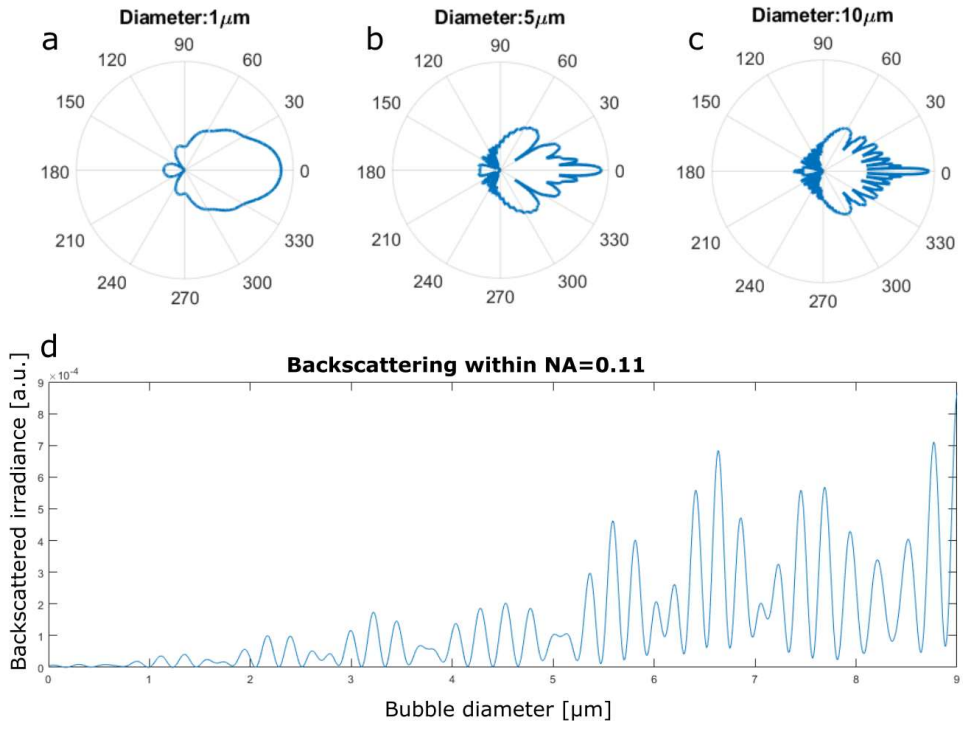

Figure 51. Backscattered irradiance (sum of equations 19 and 20) of the scattered light that could reach the photodiode. Subfigures a to c show the angular scattering distribution with increasing microbubble

diameter (1 µm, 5 µm, and 10 µm). Amplitude scaling was logarithmic. Subfigure d displays the integral of the backscattered light.

Backscattering scenarios with microbubbles of $2.5\ \mu m$ and $5\ \mu m$ were simulated. The results of the simulations that were executed with a rectangular pulse were evaluated with respect to their signal contrast. An increasing microbubble diameter was found to lead to an increase in signal contrast.

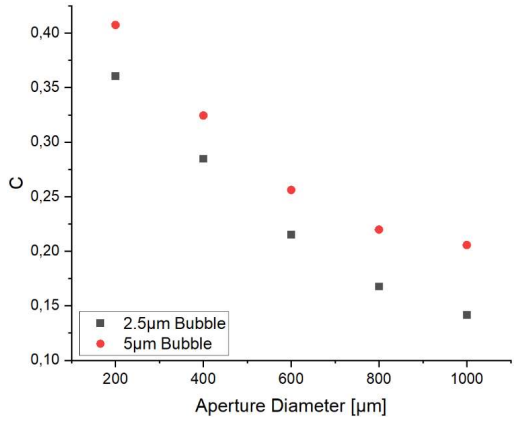

Figure 52. Increasing the bubble diameter led to an increasing signal contrast (the red dots have a higher value than the black squares).

4.2.2 Optic design influences

For spot diameters of at least $50\ \mu m$, the aperture was found to have a larger impact on the acquired speckle contrast than on the spots with diameters of $5\ \mu m$.

Figure 53 displays the speckle contrast for systems with an observation spot diameter between $5\ \mu m$ and $200\ \mu m$ over the aperture. Ten simulations were performed for each data point, and the mean speckle contrast was plotted in the graphs.

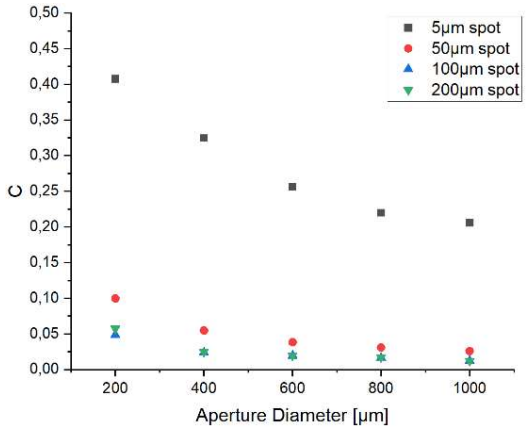

Figure 53. Influence of aperture diameter on speckle contrast. The contrast is highest at a low spot diameter.

4.2.3 Random amplitude and phase influences

During all the simulations I has been observed that identical optical setups with identical laser pulses, identical beam profiles, and identical microbubble properties (size, lifetime, etc.) can lead to different sensor signals. Figure 54 displays two simulated sensor signals under the condition of identical optical setups but different initial random amplitude and phase parameters (a and ϕ in equation 27). In the case displayed in Figure 63, the bubble size was 5 µm, the aperture was set to 200 µm, and the observation spot size was 10 µm. Figure 55 displays the intensity at the sensor under the absence of thermal- and microbubble-induced influences.

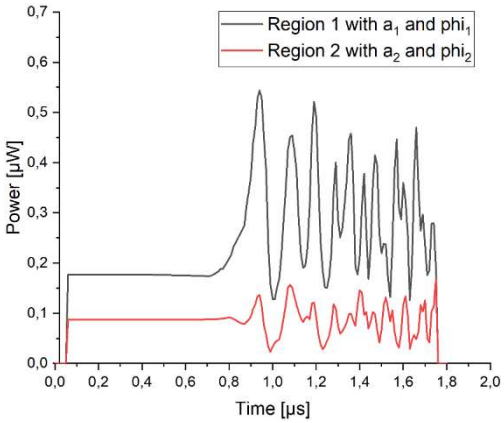

Figure 54. Simulation of two signals with identical optical setups, identical bubbles, but varying random phases and amplitudes. Differences in the overall intensity and the modulations could be found.

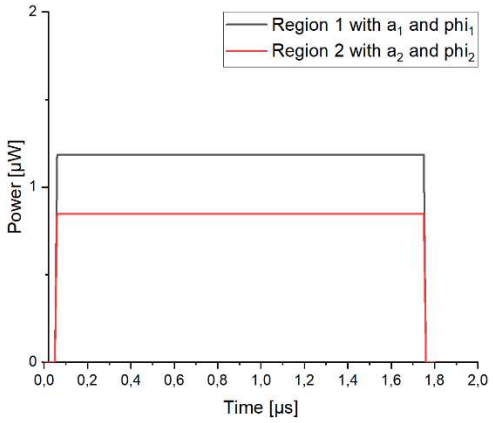

Figure 55. Simulation of two signals with identical optical setups, no thermal influence, no microbubble influence, but varying random phases and amplitudes. Differences in the overall intensity could be found.

4.2.4 Beam Profiles

It can be speculated that it may be possible to make estimation regarding the microbubble-diameter from the received backscattered light. This estimation can only be done if there are no uncontrollable \ uncorrectable influences on the acquired signals. If the beam profile turns out to have an influence on the acquired signal, it would be a uncorrectable\ uncontrollable influence. Figure 56 displays four different beam profiles. All four beam profiles were combined with the same a_{rand} and ϕ_{rand}. The same pulse was applied to all four beam profiles for this simulation. Thus, all differences in the simulated signals in Figure 56 can be attributed to the different beam profiles. In all four simulated signals, the point in time where microbubble modulations became visible is

almost identical (0.6 µs). Moreover, in all four cases modulations increased in amplitude and frequency over time. It is clearly visible that examples a and b showed more high frequency modulations than examples c and d. Furthermore, it can be observed that the overall amplitude of subfigure a_2 was higher than the overall amplitude of subfigure d_2. A comparison of signals generated by this simulation with the results is presented in Figure 65.

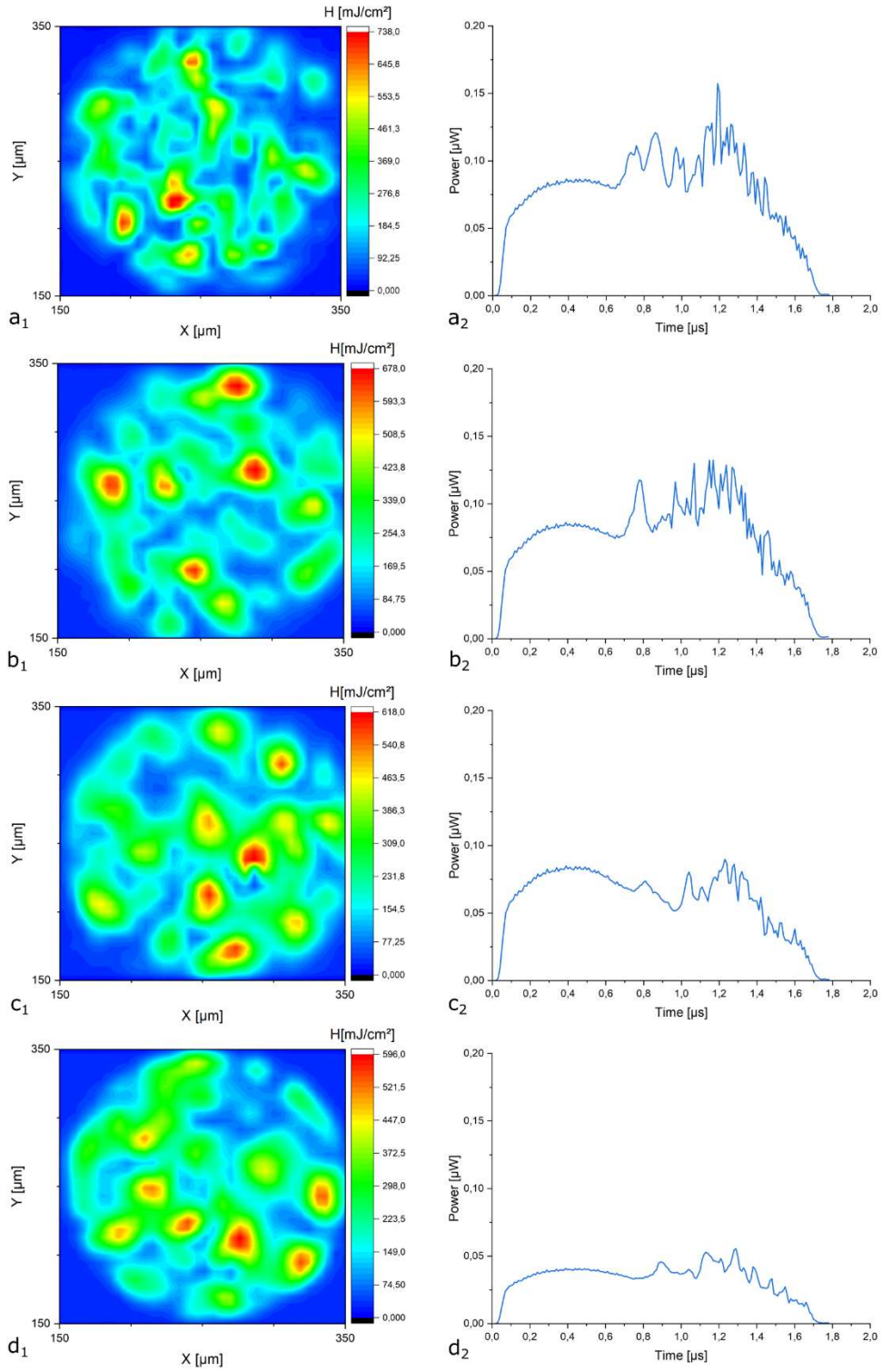

Figure 56. Simulation of signals with identical optical setups. The setups had identical random phase and amplitude, but varying beam profiles. It can be observed that beam profiles influenced the microbubble induced modulations received by the sensor and the energy that would be received by a photodiode. The beam profile was stable over the whole irradiation time.

4.3 Preclinical validation of optical feedback

4.3.1 In vivo intensity variations

In the last chapters, the results of the simulations revealed noticeable influences of spot-to-spot variations and varying beam profiles. In the animal experiments, it was observed that the overall intensity of the acquired pulses varied randomly. For example, Figure 57 displays the 30th pulses of three consecutive spots. The applied pulses in this case are almost identical. Figure 58 displays the corresponding 30th signals acquired by the avalanche photodiode. In this case the laser power of the acquired signals varies.

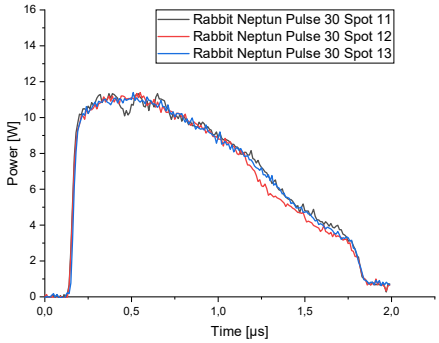

Figure 57. Three 30th pulses applied to rabbit eyes in five consecutive spots treated with the same laser pulse energy (13µJ) below MBF threshold.

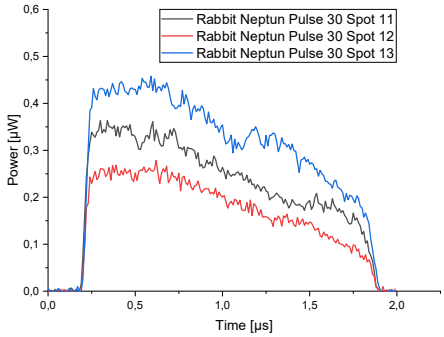

Figure 58. Three 30th backscattered pulses from the rabbit retina (pulses of Figure 57). Pulses vary in the energy received by the photodiode.

Occasionally, research has found that the overall intensity of a laser pulse can vary during the irradiation of a single spot. Figure 59 and Figure 60 display the applied and backscattered pulses of such an irradiation.

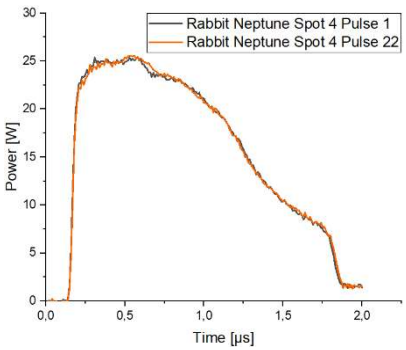

Figure 59. Two pulses with the same laser pulse energy (30µJ) below MBF threshold applied to one spot. In this instance, the time volution of the laser power is almost identical.

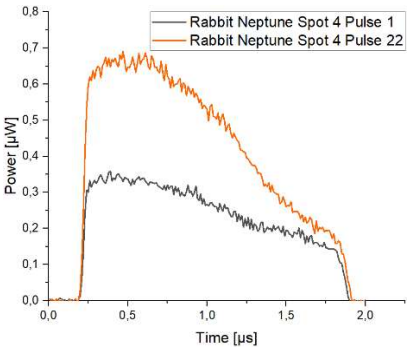

Figure 60. Two signals acquired from one spot (pulses from Figure 59). Pulses vary in the energy received by the photodiode.

Although the first clinical study on patients (with clinic system version 1) was not evaluated in this work, one particular finding must be presented to explain of the discussed variations. As can be seen in Figure 61, the overall intensity of the backscattered light can vary significantly, even if 30 pulses of the same laser pulse energy has been applied. No signs of microbubble formation can be found in the backscattered pulses or in the optoacoustic data. However, the absolute intensity, or pulse energy, of the backscattered pulse varies randomly and according to the pulse. This observation has been made more frequently in clinical data than in preclinical data.

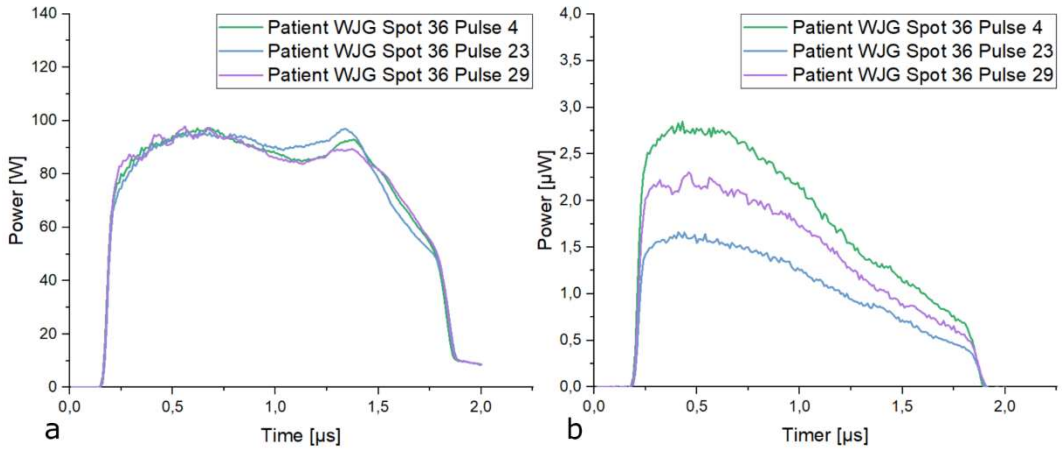

Figure 61. Subfigure a shows three pulses with the same laser pulse energy (130µJ) below the MBF threshold, applied to one spot in a patient's eye. Subfigure b shows backscattered light from the patient's eye. Movement of the patient's eye (within 10 ms pulse intervals) are assumed to cause these fluctuations by creating new random phase and amplitude values.

4.3.2 Modulation dynamics

Pulses applied in the test spot ramp mode were used to gain information about the dynamics of microbubble-induced modulations. The point at which microbubbles form can sometimes be determined by the occurrence of modulations. In Figure 62 the applied pulses (subfigure a) and the backscattered light (subfigure b) belong together. It can be seen that when more laser power is applied, microbubble formation starts earlier during the time of irradiation. However, this relationship about the timing of microbubble occurrence turned out to be difficult to evaluate. The difficulty was mainly due to a low signal, noise ratios, and unwanted modulations on the applied laser pulses themselves (not induced by microbubbles). Thus, no algorithm making use of this phenomena was employed.

In the preclinical study, similar unwanted laser pulse modulations that originated in the laser resonator were observed. These modulations are displayed in Figure 62, subfigure c (applied pulses) and subfigure d (backscattered light). An evaluation of these instabilities revealed that the modulations have frequency components between 5 MHz and 10 MHz.

The algorithm's first clinical study, which is not discussed further in this work, compensated for this circumstance by increasing the cutoff frequency of the digital bandpass filter in the microbubble detection algorithm to 10 MHz. For further product versions, which were discussed later in this work, the laser resonators were improved to have these types of modulations removed.

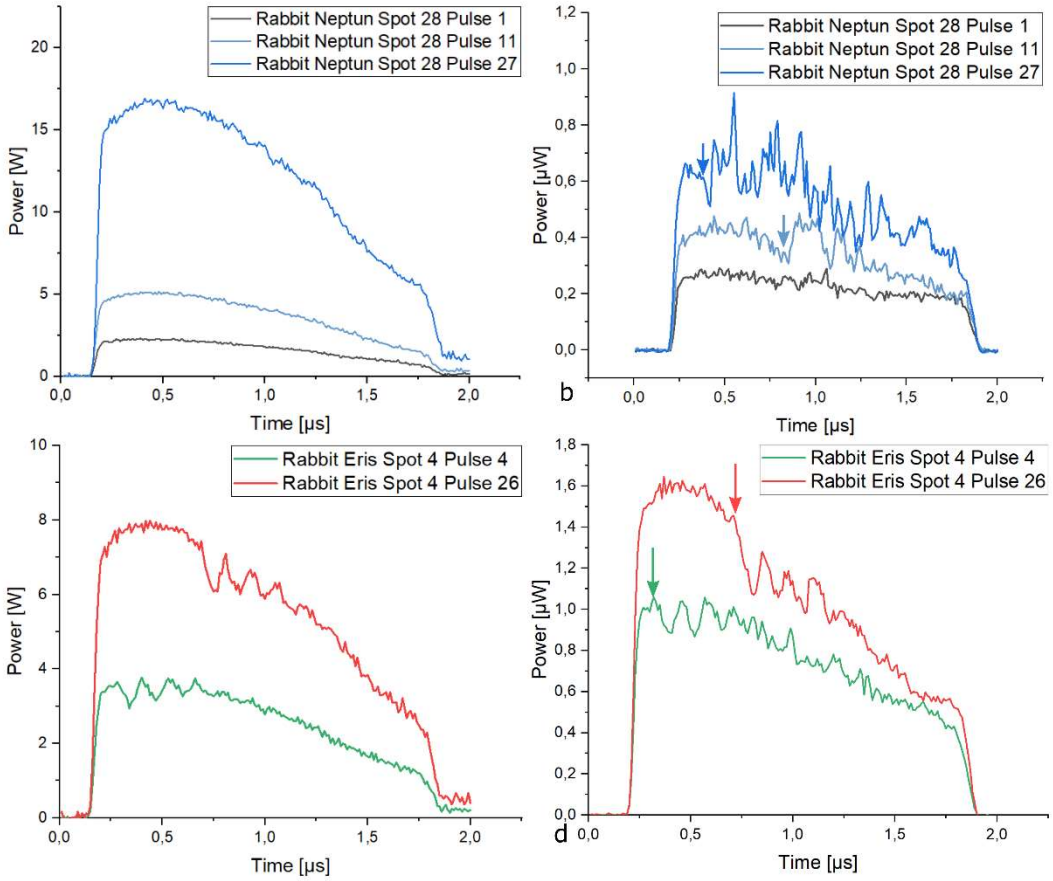

Figure 62. Pulses applied to the RPE (a and c) and the corresponding backscattered light (b and d). On some occasions, the initial point of microbubble formation could be found. In most cases, this point was nearly impossible to detect since laser pulse instabilities led to modulations similar to microbubble-induced modulations.

4.3.3 Applicability for automatic irradiation ceasing

Automated treatments need to be performed during the in-vivo experiments, to test automated irradiation ceasing. If the system works correctly, barely FA visible lesions should be visible in region where the irradiation has been ceased after the first pulse with identifiable modulation in the optical sensor signal. Figure 63a presents the backscattered pulses of the treated spot, and Figure 63b displays the RM values of each pulse applied to the eye. Despite the linear pulse energy increase, the RM_{V1} values varied only slightly until pulse number 16. At pulse number 16, a sudden increase in RM_{V1} value can be observed in the figure.

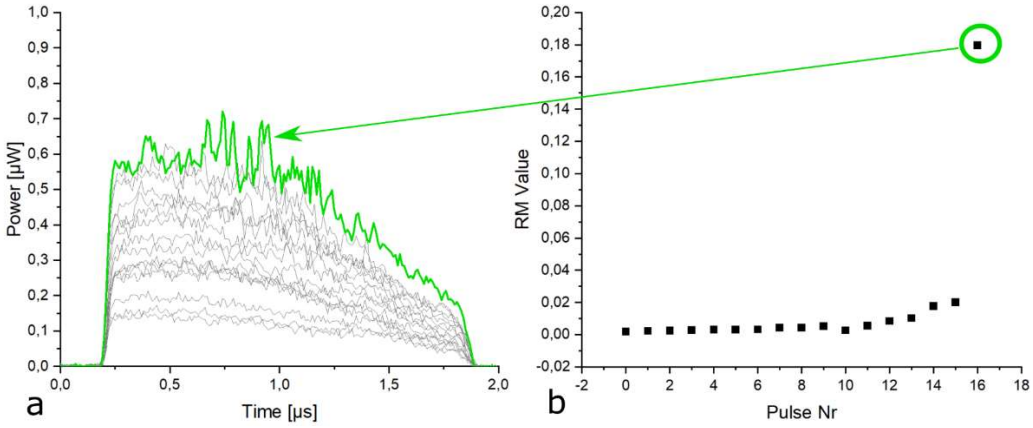

Figure 63. RM signals and their corresponding optical feedback values.[177] The signals measured in vivo were applied successfully within an experimental treatment to cease the laser irradiation.

Figure 64a presents a histogram of the number of FA-visible spots regarding the highest radiant exposure applied to a spot. The direct transmission of 0.5 and the IMF of 3.8 were considered. Figure 64a illustrates the intra- and interindividual variations of the selective cell damage in the rabbit retina through color-coded bars that correspond to the eye from which the data originates. From the bar graph, it can be observed that most radiant exposure levels were accumulated at levels below 200 mJ/cm². The images in Figure 64, subfigures b and c show the fundus and the corresponding FA image, respectively. Figure 64c contains the corresponding maximum radiant exposures for the encircled regions.

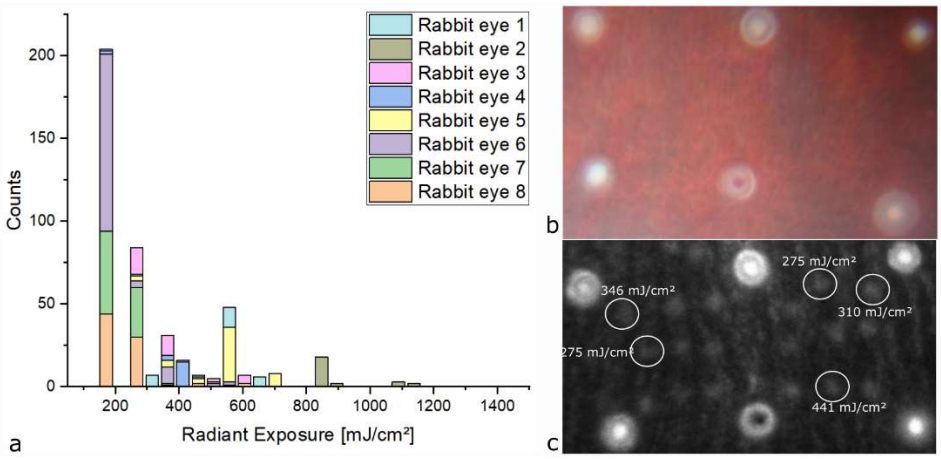

Figure 64. Histogram of maximum radiant exposures where irradiation was ceased (various regions and eyes). These regions were not ophthalmoscopically visible (subfigure b), but they were visible in FA images (subfigure c). The direct transmission (0.5) and the IMF (3.8) were considered in the calculation process of the radiant exposure.

The system did not seem to perform perfectly. Several ophthalmoscopically visible spots were observed during this study. Figure 65 illustrates regions where three ophthalmoscopically visible changes were reported during treatment.

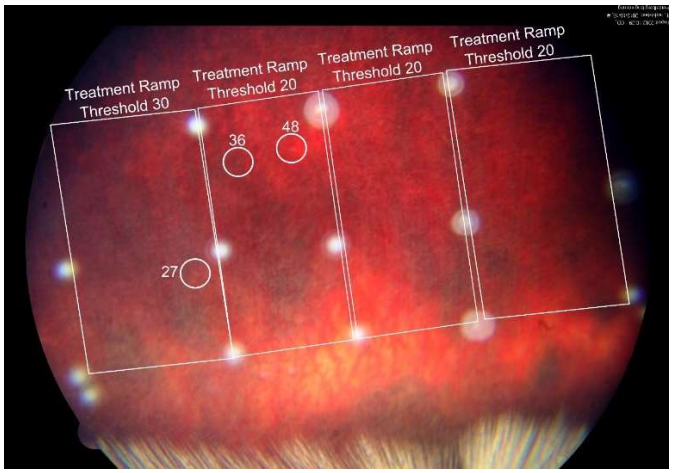

Figure 65. Not all automatic ceasing were successful. Regions with ophthalmoscopically (hardly) visible regions are highlighted.

The first pulse of these ophthalmoscopically visible lesions were found to have induced microbubble formation. Thus, the value I_1 in the RM_{V1} algorithm did not represent a value that was a reference for a case without microbubble formation. Cases where even the first pulse is above threshold can be solved by the TV algorithm (which can detect this with the second pulse) or by optical feedback (which can detect a microbubble with data of just one pulse).

4.3.4 Lesion evaluation

4.3.4.1 OCT based evaluation

SRT lesions were evaluated at St. Mary's Hospital by Park et al. This evaluation included the use of color images, OCT images, FA images, a histological evaluation (H&E staining), and electro-renigrams.[177, 178] The state of the neural retina determined by the OCT did not indicate retinal damage by SRT (Figure 66c arrows). SRT lesions induced just enough damage to break the blood retina barrier. This result was able to be identified by hyper-fluorescence in the FA images (Figure 66b pointers). In addition, the neural retina seemed undamaged in OCT images.

In contrast to SRT lesions, photocoagulation (marker) lesions were detectable in the OCT images (Figure 66c arrows) by changes in the backscattering properties of the neural retina. The center of a coagulation lesion was also observed to appear darker than an SRT lesion (Figure 66b arrows).

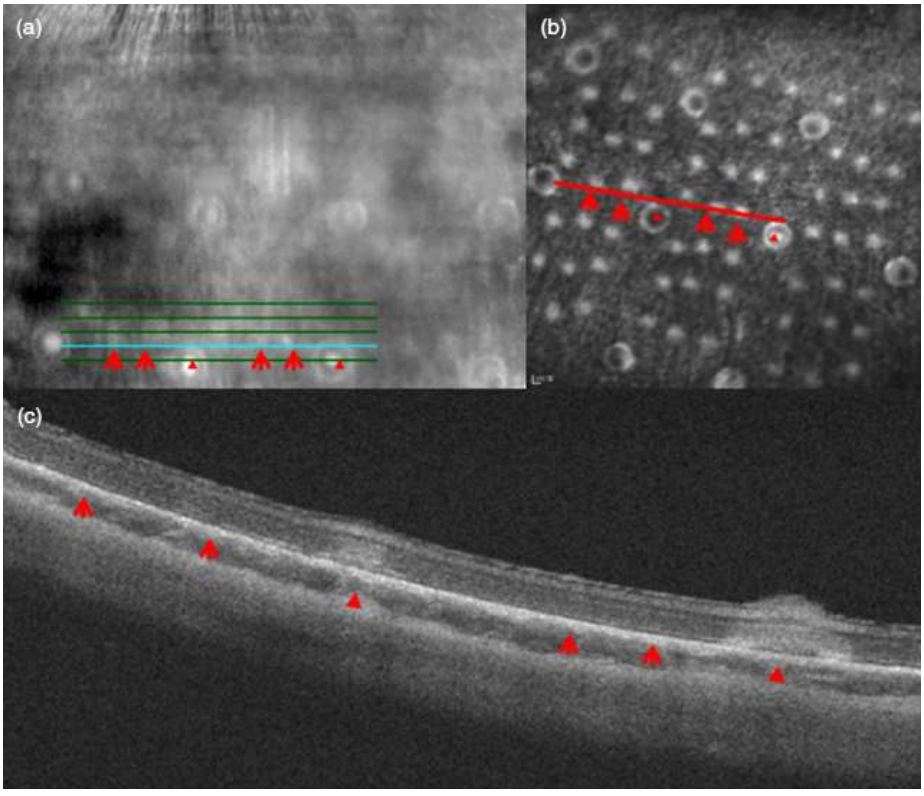

Figure 66. Image a depicts an en-face image, b shows an FA image, and c) shows a OCT B-scan of a rabbit's fundus 1 hour after treatment.[177] The red arrows indicate SRT lesions, and the red triangles indicate marker lesions. Damage done by the SRT can be seen to be less than the damage done by marker lesions. Sometimes the IS/OS layer indicating loss of contrast by the photoreceptors in regions where SRT irradiation was assumed.

4.3.4.2 Histology (H&E staining)

The histological evaluation was done three weeks after treatment. Regarding the damage induced by SRT irradiation (Figure 67a), “the photoreceptor inner segments were preserved, and the distal ends of the photoreceptor outer segments were relaxed. The RPE layer was focally proliferated along the SRT lesions (arrowhead), and the Bruch’s membrane was intact”[177] (Figure 67a, triangles). In the histological image of the coagulation marker lesions (Figure 67b), severe morphological changes can be observed over several retinal layers (entire region above three red triangles).

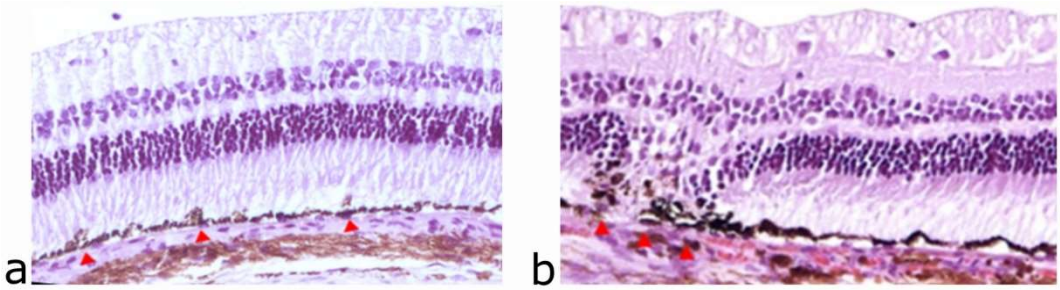

Figure 67. Subfigure a displays SRT lesions with RPE cell accumulation (red triangles). The RPE accumulation was not intended, but the photoreceptor layer seems to be intact. In subfigure b, the coagulation lesion with damaged retinal layers can be seen (entire region above the three red triangles).[177]

4.4 Clinical validation of optical microbubble detection

4.4.1 Unevaluable data

The shortcomings in the algorithm that lead to ophthalmoscopically visible spots in animal trials were removed by software routines like improved normalization and jitter correction. However, there were some error cases that remained and could not be corrected algorithmically. If the intensity of the backscattered light at the sensor was excessively low, possible microbubble-associated characteristics could have been lost in noise. Figure 68 displays such a case.

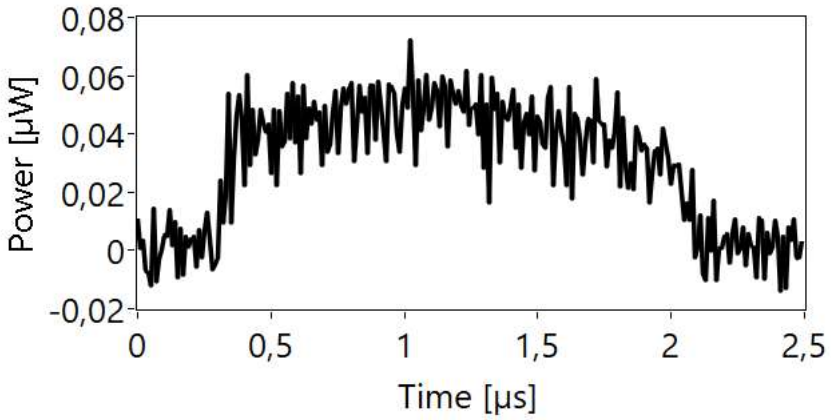

Figure 68. Example of acquired signal with low signal to noise ratio. Such data could not be evaluated.

Overall, 1,384 pulses were regarded as not evaluable by the algorithm. The following evaluations were conducted with the remaining 4,626 pulses.

4.4.2 Overview

The data was acquired during the treatment of 15 patients in the eye clinics of the UKSH Kiel and the Hannover Medical School. The training set consisted of 2,516 pulses classified as RM-positive and 615 pulses classified as RM-negative. The CV set consisted of 1,121 pulses classified as RM-positive and 165 pulses classified as RM-negative. The test set consisted of 106 pulses of spots classified as FA visible and 103 pulses of spots classified as FA-non-visible. The results were published by the author [179].

4.4.3 Training set optima characteristics

The ability of the microbubble detection algorithms, which are presented in this work highly depend on the chosen settings in the digital signal processing steps. An optimization procedure was used to find the optimal settings. The result of the algorithm's optimization suggested an optima with a fitter threshold of F_J = 4.9, a lower cutoff frequency of 3.5 MHz, a higher cutoff frequency of 25.5 MHz, a ROI Range from 0.38 µs to 1.74 µs, and a ROI threshold factor of 5.9. Note that this version of the laser system did not suffer from severe laser pulse modulations from the laser resonator. Thus, the cutoff frequency of the bandpass filter in the algorithm could be lowered.

Sensor data for spots without any microbubble-induced modulations (Figure 69b) were found to lead to RM value accumulation in a low-value regime (Figure 69a, yellow dot). This data could typically be found in FA-nonvisible spots. Figure 69c displays a case where the first pulses did not show any microbubble-induced modulation, but later pulses did. The corresponding RM values can be found in Figure 69a (green rectangles).

Other FA-visible spots received maximum pulse energies far above initial MBF. As a result, even the first pulses displayed microbubble-induced modulations in the sensor data (Figure 69d). In these instances, how far above the MBF threshold the first pulse already was, cannot be predicted (Figure 69a blue rectangles). This observation also implies that δ of the local pulse energy for ophthalmoscopic visibility is typically larger than two.

The same observation (first pulse above MBF threshold) can also be made in the case of ophthalmoscopically visible spots. In the entire dataset, there were only two examples of ophthalmoscopically visible spots from a first pulse without microbubble-induced modulations. One example is displayed in Figure 69e. At this irradiation, initial MBF occurred at 81.4 µJ. The corresponding pulse is plotted in red in the figure. An E_{max} of 141.7 µJ was measured. Thus, there was a δ of 1.74 from the initial microbubble formation to ophthalmoscopic visibility at this pulse. The RM values of these spots are plotted in Figure 69a (red dots).

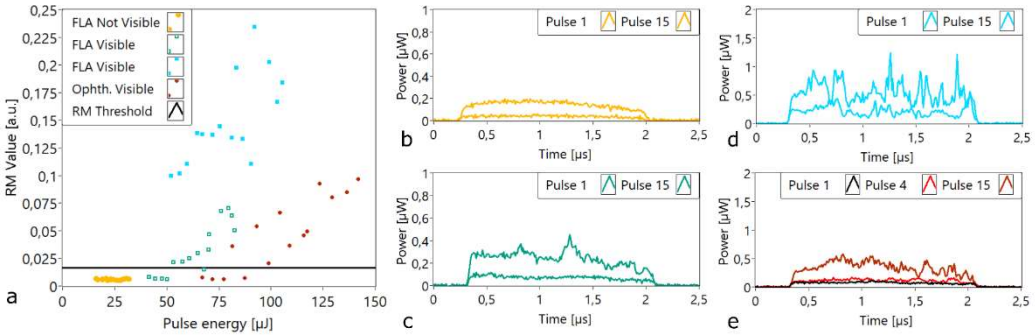

Figure 69. In subfigure a, RM values of selected examples processed with the optimized algorithm settings are presented. In subfigures b to e, the first and last pulses of the mentioned examples are displayed. Subfigure e also displays the first pulse with microbubble-induced modulations (Pulse 4, red). The examples also include the sensor data of FA-nonvisible spots (b), FA-visible spots (c and d), and ophthalmoscopically visible pots (e).

4.4.4 RM value: Training CV set comparison

Performance metrics of the chosen optimum settings are presented for two threshold values. The threshold value of 0.012 led to a maximum Y-index of 0.96 in the cross-validation dataset. Sensitivity and specificity were equally close to the optimum value of one. The PM differences between the CV set and the training set were within the 95 % confidence intervals. In SRT, it is desirable to lower the number of false positives in order to maximize the therapeutic effect of the treatment. One way to achieve this is to increase the RM threshold. At a threshold of 0.023, the CV set does not have any false positives.

However, increasing the specificity by increasing the RM threshold results in a decrease in sensitivity. The Y-index in the CV set in this case was reduced by 0.06. Maximum Performance Measur“ (”M) differences of 0.01 and 0.017 for thresholds of 0.012 and 0.023 were found.

In Figure 70, subfigures a and b depict scatterplots of calculated RM values for the training and CV datasets. Datapoints of sensor signals influenced by microbubbles were colored green, and datapoints of sensor signals without any influence of microbubbles were colored yellow. The horizontal lines indicate threshold values. The solid line represents a threshold of 0.012 (maximum Y-Index in CV set), and the dashed line represents a threshold of 0.023 (no false positives in CV set). Subfigure c displays the ROC curve. The threshold dependent sensitivity-specificity pair (performance metric) is colored black for the threshold with the highest Y-Index in the CV set and blue for the threshold with a specificity of 1 in the CV set. The table in subfigure d summarizes the performance.

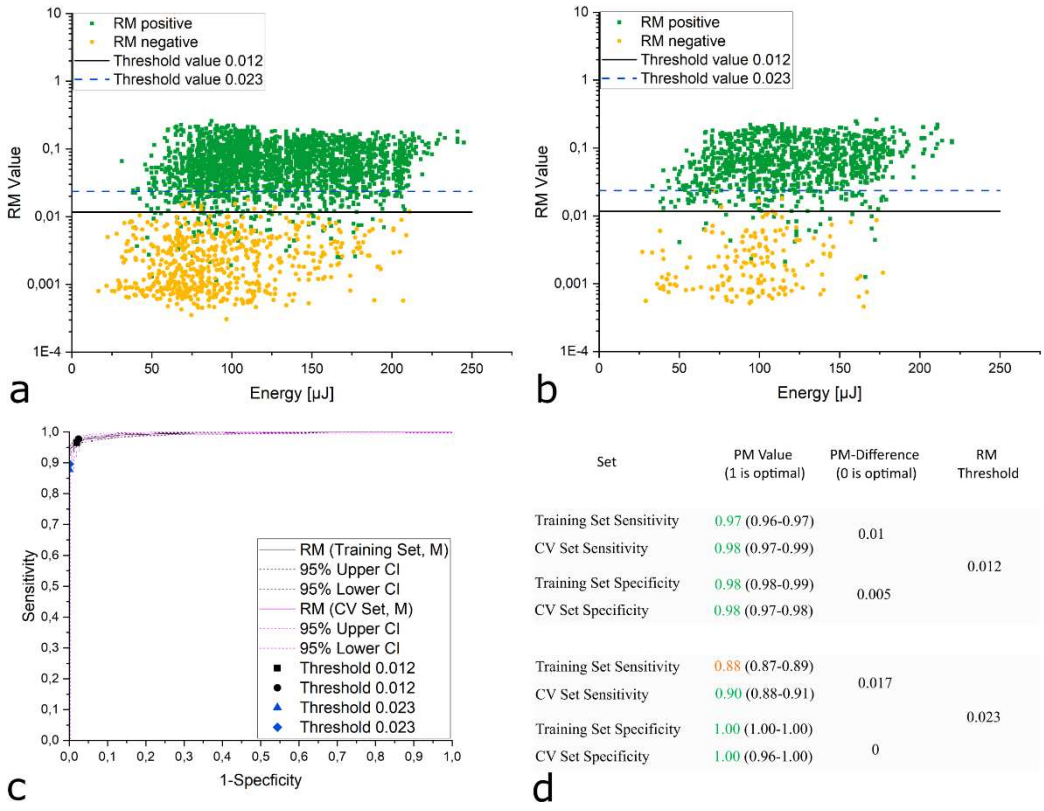

Set	PM Value (1 is optimal)	PM-Difference (0 is optimal)	RM Threshold
Training Set Sensitivity	0.97 (0.96-0.97)	0.01	0.012
CV Set Sensitivity	0.98 (0.97-0.99)		
Training Set Specificity	0.98 (0.98-0.99)	0.005	
CV Set Specificity	0.98 (0.97-0.98)		
Training Set Sensitivity	0.88 (0.87-0.89)	0.017	0.023
CV Set Sensitivity	0.90 (0.88-0.91)		
Training Set Specificity	1.00 (1.00-1.00)	0	
CV Set Specificity	1.00 (0.96-1.00)		

Figure 70. Subfigure a is a scatter plot of the training data set. Subfigure b shows a scatter plot of the CV dataset. Subfigure c shows the ROC curves of the training and CV datasets with two threshold values highlighted in each curve. Performance metrics of the highlighted threshold values are shown in subfigure d. The numbers in parentheses are the 95 % confidence intervals.

4.4.1 RM value: CV test set comparison

The PM difference was both larger and more uncertain in the test set than in the CV set. For example, a threshold value of 0.012 led to a sensitivity and specificity of 1 and 0.93, respectively, in the test set. The PM difference in the CV set were at 0.02 and 0.05. A threshold value of 0.023 led to sensitivity and specificity of 0.98 and 0.98, respectively, in the test set. Compared to the CV set, the PM differences were at 0.08 and 0.02. The PM differences were within the 95 % confidence intervals, except for the specificity values at the 0.012 threshold. Figure 71a and b display the scatterplots of the test and CV set. Subfigure c displays the ROC curve. The threshold dependent sensitivity-specificity pair (performance metric) is colored black for the threshold with the highest Y-Index in the CV set and blue for the threshold with a specificity of 1 in the CV set. The table in subfigure d presents the numbers discussed at the beginning of this chapter.

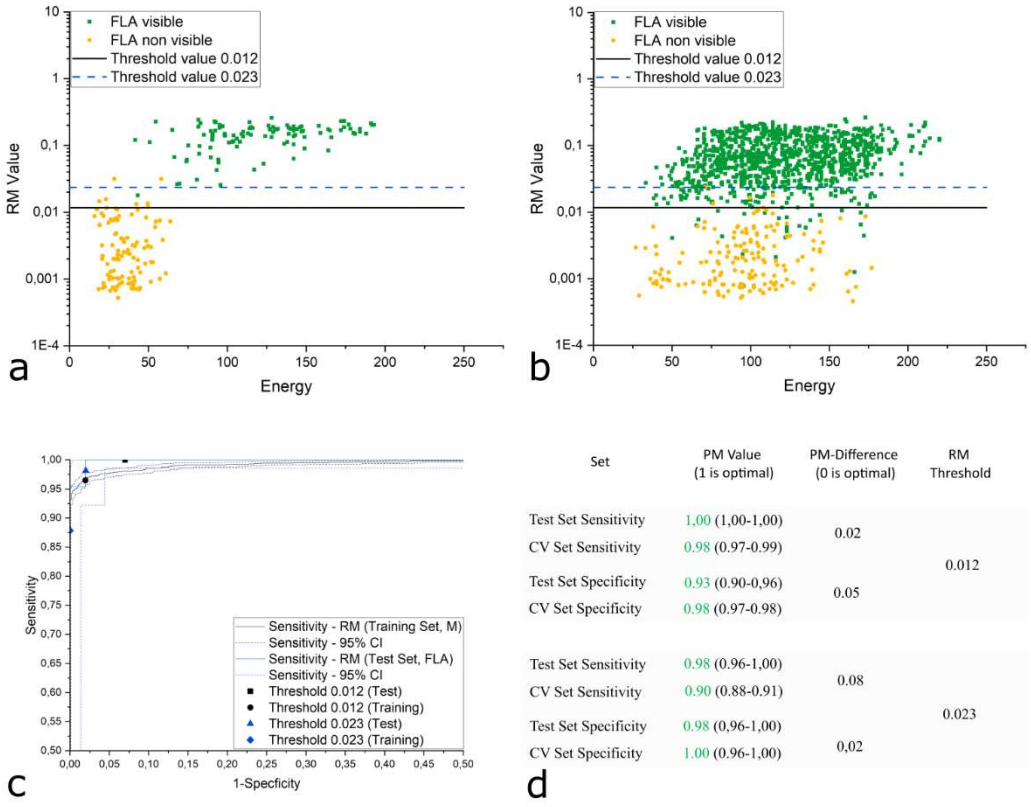

Set	PM Value (1 is optimal)	PM-Difference (0 is optimal)	RM Threshold
Test Set Sensitivity	1,00 (1,00-1,00)	0.02	0.012
CV Set Sensitivity	0.98 (0.97-0.99)		
Test Set Specificity	0.93 (0.90-0,96)	0.05	
CV Set Specificity	0.98 (0.97-0.98)		
Test Set Sensitivity	0.98 (0.96-1,00)	0.08	0.023
CV Set Sensitivity	0.90 (0.88-0.91)		
Test Set Specificity	0.98 (0,96-1,00)	0,02	
CV Set Specificity	1.00 (0.96-1,00)		

d

Figure 71. Subfigure a presents a scatter plot of the test set data. Subfigure b shows a scatter plot of the CV dataset. Subfigure c shows the ROC curves of the test and CV datasets with two threshold values highlighted in each curve. Subfigure d presents the performance metrics of the highlighted threshold values. The numbers in parentheses are the 95 % confidence intervals.

4.4.2 Laser pulse energy comparison

Since no optimization was conducted on the laser pulse energy decision-making, nearly identical ROC curves and nearly identical performance metrics at a certain threshold value were expected to be found. The scatterplot of each feedback method presented in this work (RM, NL, TV) displays the laser pulse energy on the x-axis. It can be observed in most of the scatter plots that microbubble induced signal characteristics (RM modulations, loss of linear increase in pressure transient amplitude, loss of time invariance in consecutive pressure transients) could not be discriminated well by the laser pulse energy.

Test spots were chosen in regions where there was no retinal detachment, while treatment spots were selected in regions with retinal detachment. In diseased regions it is difficult to focus the laser well. In addition, scattering properties and pigmentation of affected regions may differ from regions without retinal detachment. Hence, it was assumed that a single laser pulse energy threshold would lead to very different performance metrics in these affected regions. Figure 72 displays the ROC curves of the RM algorithm (black, green, and blue curves) and the laser pulse energy (brown, orange, and yellow curves). Furthermore, these curves plot the sensitivity and specificity regarding detection of microbubble-induced modulations. It can be observed that a single threshold value led to very different performance metrics in the test set when compared to the use of the same threshold value in the training or CV set (red double arrow in Figure 72). These differences were not present when RM values were used to make a distinction.

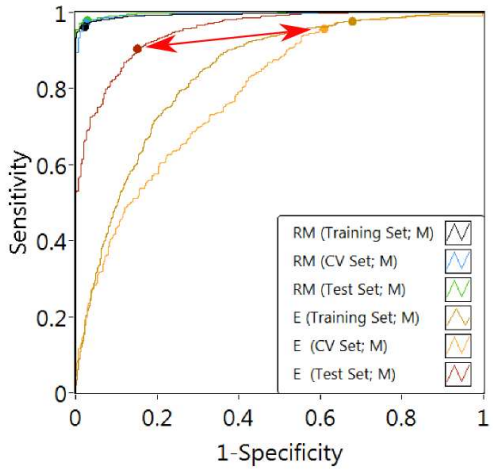

Figure 72. ROC curves of the training, CV, and test sets of the RM algorithm and the laser pulse energy: The sensitivity and specificity to detect microbubbles in raw data is displayed. The RM values are almost identical between datasets. However, pulse energy values differ substantially, especially between the CV and test sets. This was an indicator that pulse energies in diseased regions differ from those in healthy regions.

4.4.3 Intra- and interindividual variations

High intra-individual variations of the local energy for MBF (E_{MBF}) were found. Table 6 summarizes the max-min deviations of the E_{MBF}. The differences were most pronounced in patients DME2, DME3, and CSCR4. It is important to note that this evaluation was limited to nine patients only. This limited number of patients was due to the additional constraint of having at least one spot with the first pulse below the threshold for MBF. Nevertheless, the variations in the max-min values of the local E_{MBF} values (see Table 6) emphasize the necessity for a single-pulse microbubble detection technique. Only with such techniques can knowledge about the position inside and outside the TW_{δ} be gained.

Patient Pseudonym	Mean MBF Energy(µJ)	Min MBF Energy (µJ)	Max MBF Energy (µJ)
CSCR 1	62	55	68
CSCR 2	64	47	87
CSCR 4	90	58	141
CSCR 6	61	55	70
CSCR 8	60	48	81
CSCR 9	40	30	48
CSCR 10	49	41	61
DME 2	76	28	123
DME 3	63	39	109

Table 6. Initial MBF energy: This evaluation was limited to only nine patients due to the necessity to have at least one spot with the first pulse below the threshold for MBF to find the MBF-threshold. The RM threshold of 0.023 was applied for MBF identification. The spot diameter was 200µm and the IMF was 3.8.

4.5 Clinical validation of optoacoustic microbubble detection

4.5.1 Overview

The training, used in the automatic optimization process, set consisted of 1,847 pulses with microbubble-induced variations and 1,414 pulses without. The CV set, used to define the threshold value, consisted of 770 pulses with microbubble-induced variations and 384 pulses without. The test set, used to test the developed microbubble detection to discriminate states of cell damage, consisted of 161 transients of FA hyper-fluorescent regions and 70 transients of FA non-hyper-fluorescent regions. Results were already published in [180]

4.5.2 Unevaluable data

Three main types of unevaluable data were identified. The first type was called early starting optoacoustic transients. These error types were characterized by oscillations in the first nanoseconds after the start of acquisition. The existence of these early oscillations influenced the offset-removal routines of the algorithm and thus each value of the processed signal contributing the OA value. The origin of these early oscillations is unclear. Figure 73a and b illustrate input signals with such early oscillations. The second type of unevaluable data were data with a low amplitude type. With some signals, the amplitude signal was barely higher than the electronic noise which is produced by the acquisition electronics. Figure 73c illustrates this error type. The final primary error type was the “saturated signals” type. In these cases, the voltage at the input of the analog digital converter (ADC) was larger than the ADC’s dynamic rage. Figure 73d illustrates this error type. The error detection process was identical for the NL and TV algorithms. In total, 853 pulses were regarded as not evaluable by the algorithm. The evaluations discussed in the following chapters were conducted with the remaining 4,446 pulses.

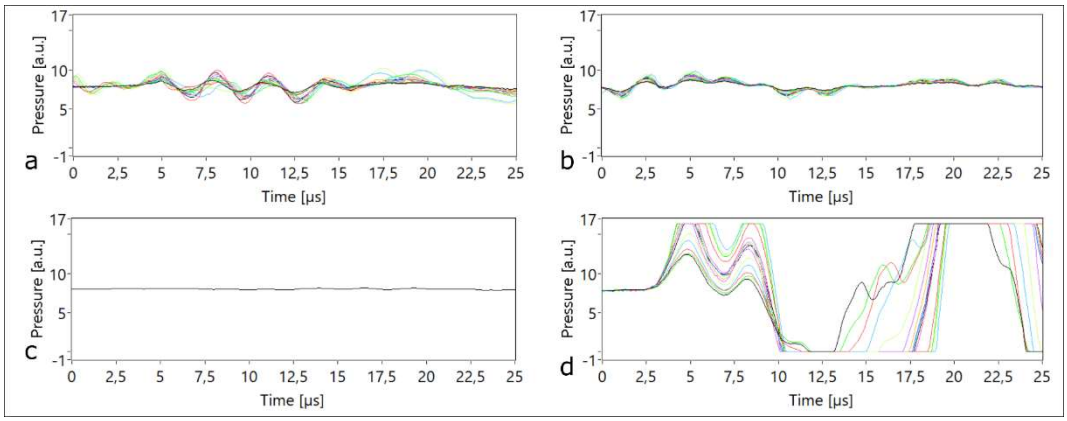

Figure 73. Examples of unevaluable sensor signals for the error types of early transients (subfigure a and b), low amplitude (subfigure c), and saturated signals (subfigure d).

4.5.3 Comparison to baseline characteristics

For both the NL and TV algorithms, the parameter optimization of the training set identified a performance optimum (best discrimination of OA-positive and OA negative in the training set) using a bandpass filter with a high cutoff frequency of around 6 MHz and a low cutoff frequency of around 110 kHz. Additionally, the optimization procedure found the value of $i = 11$ for the algorithm variable as best.

All algorithms, including the baseline algorithm, offered values that increased with microbubble associated characteristics. However, the energy dependence of the BL algorithm was found to lead to false decisions.

In the scenario displayed in Figure 74, subfigures a and b, the baseline algorithm led to BL values above threshold. However, no signs of MBF could be found in the raw data. The results displayed in this graph originated from a treatment spot lesion from the training set. It can also be observed that the NL and TV values were not negatively influenced by the laser pulse energy.

In the scenario displayed in Figure 74, subfigures c and d, it can be observed that the baseline method did not exceed its threshold value in the case of microbubble formation. The low values of the acquired signal (transient) were the cause for these low BL values. The results displayed in this graph originated from a treatment spot in the training set.

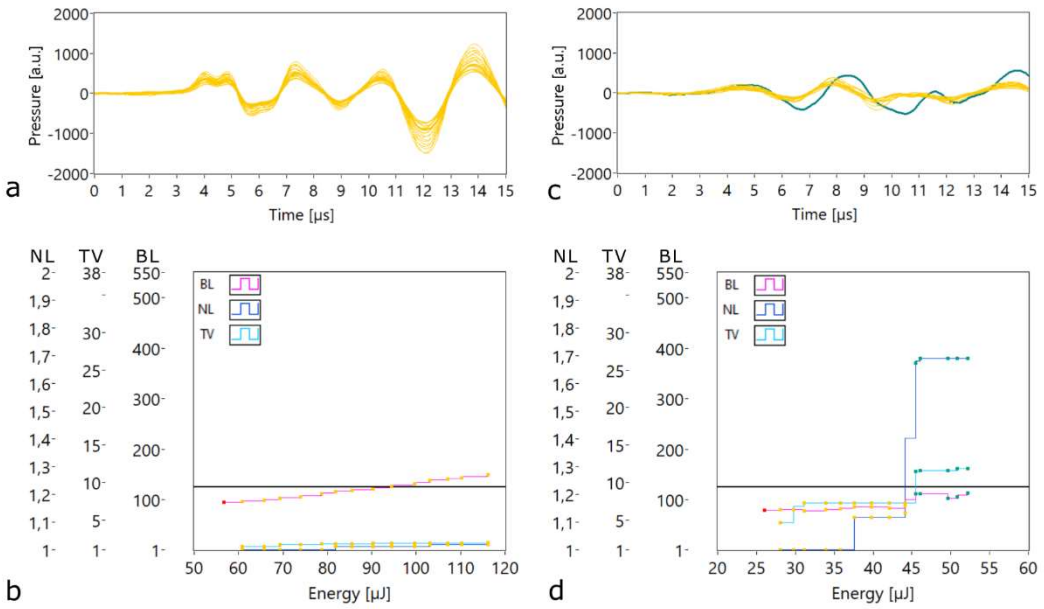

Figure 74. Examples of OA values of a spot above and below the threshold for microbubble formation. The black horizontal line represents the threshold value for all three algorithms. Subfigure a shows sensor data from an FA-visible test spot. Subfigure b presents the corresponding OA values from the data of subfigure a for all three algorithms. Subfigure c shows data from a treatment spot without any sign of microbubble formation in the sensor data, in the OA-sensor signals, nor in any other regard. Subfigure d presents the corresponding OA values from the data of subfigure c for all three algorithms.

4.5.4 Performance measures for optoacoustic microbubble detection

The ability to use optoacoustic techniques for microbubble detection was evaluated by comparing performance metrics of the training and CV sets. These performance metrics were summarized in figures like Figure 75d. In these figures values below 0.8 were colored red, values above 0.8 and below 0.9 were colored orange, and values of at least 0.9 were colored green. Performance metrics of two threshold values were presented. The first threshold had the highest Y-index. The second threshold had the lowest threshold and led to the lowest number of false positives in the CV set. Increasing threshold values is one method for increasing the specificity of an MBF detection system. Another method to keep the number of false positives low is to exceed the threshold radiant exposure by a well-defined amount. The chapter about the threshold dependent therapeutic window explains this method in more detail (see chapter 4.6).

BL algorithm

At a threshold of $BL = 125$, which is where the Y-index was highest in the CV set, sensitivity and specificity of the training set was around 0.77 (sensitivity) and 0.87 (specificity). In the CV set, the sensitivity-specificity pairs were around 0.82 (sensitivity) and 0.87 (specificity). At a threshold of $BL = 199$, which is where the specificity in the CV set reached a value of 1, the sensitivity of the CV and training sets dropped to the 50 % mark. With this threshold the ability to identify cell damage was almost identical to a random decision. Figure 75a and b show the scatterplots of the training and CV sets resulting from the application of the BL algorithm. Since no optimization was done with the BL algorithm, all the PM differences that would be found were expected to be within each other's confidence intervals (e.g., CV sensitivity would be within the 95 % confidence interval of the training sensitivity). However, the PM differences of the CV and test sets were observed to be farther apart than each set's 95 % confidence interval. Figure 75c displays the ROC curves of the training and CV sets. The previously mentioned performance metrics of the thresholds mentioned above were highlighted by the black and blue points in subfigure c and in the table in subfigure d.

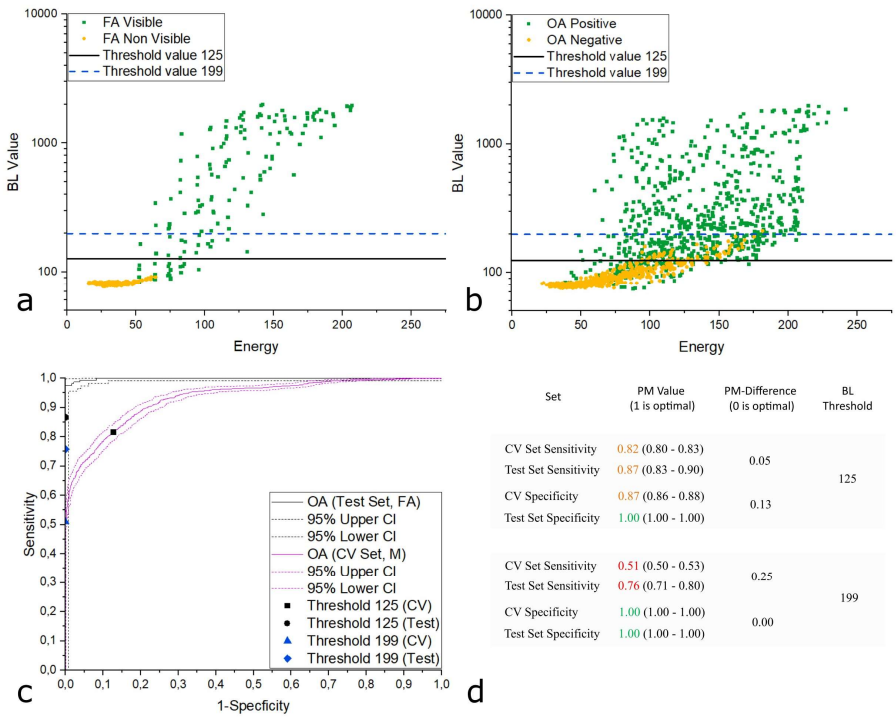

Figure 75. The BL algorithm was used in this scenario. Subfigure a shows the scatter plot of the training data set. Subfigure presents the scatter plot of the CV dataset. Subfigure c depicts the ROC curves of the training and CV datasets with two threshold values highlighted in each curve. Subfigure d shows the performance metrics of the highlighted threshold values. The numbers in parentheses are the 95 % confidence intervals.

NL algorithm

At a threshold of $NL = 1.15$, which is where the Y-index (0.89) was highest in the CV set, the NL algorithm achieved a sensitivity of 0.89 in the training set and a sensitivity of 0.92 in the CV set. These values were outside the 95 % confidence intervals of the datasets. Interestingly, the CV set offered the better performance with this algorithm.

In the scatterplot of the BL algorithm, the OA Negative BL values can be observed to increase with increasing laser pulse energy (see Figure 75, subfigures a and b). The NL algorithm was designed not to have this property. Thus, the scatterplots in Figure 76, subfigures a and b show a steady horizontal threshold region over the whole laser pulse energy range.

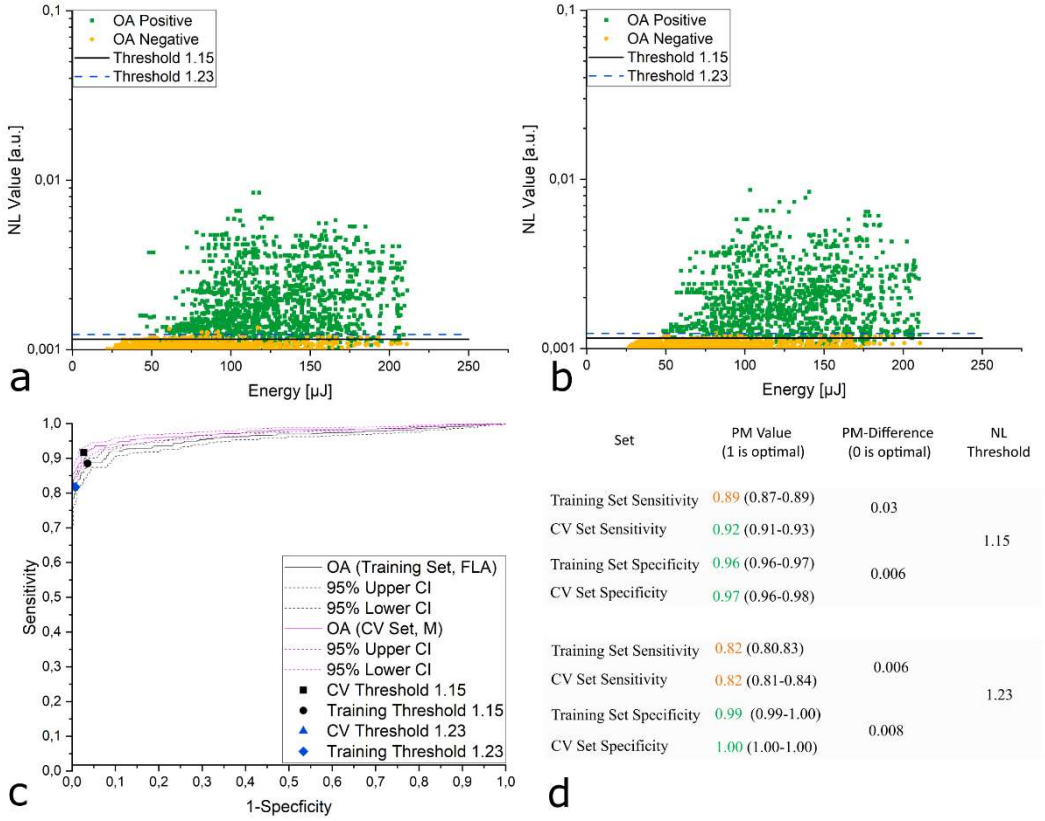

Figure 76. The NL algorithm was used in this scenario. Subfigure a shows the scatter plot of training data set. Subfigure b presents the scatter plot of CV dataset. Subfigure c depicts the ROC curves of the training and CV datasets with two threshold values highlighted in each curve. Subfigure d shows the performance metrics of the highlighted threshold values. The numbers in parentheses are the 95 % confidence intervals.

TV algorithm

At a threshold of $TV = 5.2$, the Y-index (0.87) was highest in the CV set. The sensitivity in the training set was 0.89, and the sensitivity in the CV set was 0.91. These values were outside the 95 % confidence intervals of the datasets. The PM differences of sensitivity and specificity were at 0.02 and 0.001, respectively, between the datasets. When the threshold value was increased to 6.1, which is where the specificity in the CV set reached a value of 1, a drop occurred in the sensitivity to 0.86 and 0.84 in the training and CV sets, respectively. The differences were within the confidence intervals of the datasets. In Figure 87, subfigures a and b, it can be observed that, as with the NL algorithm, there was no monotonic increase of TV values with increasing laser pulse energy.

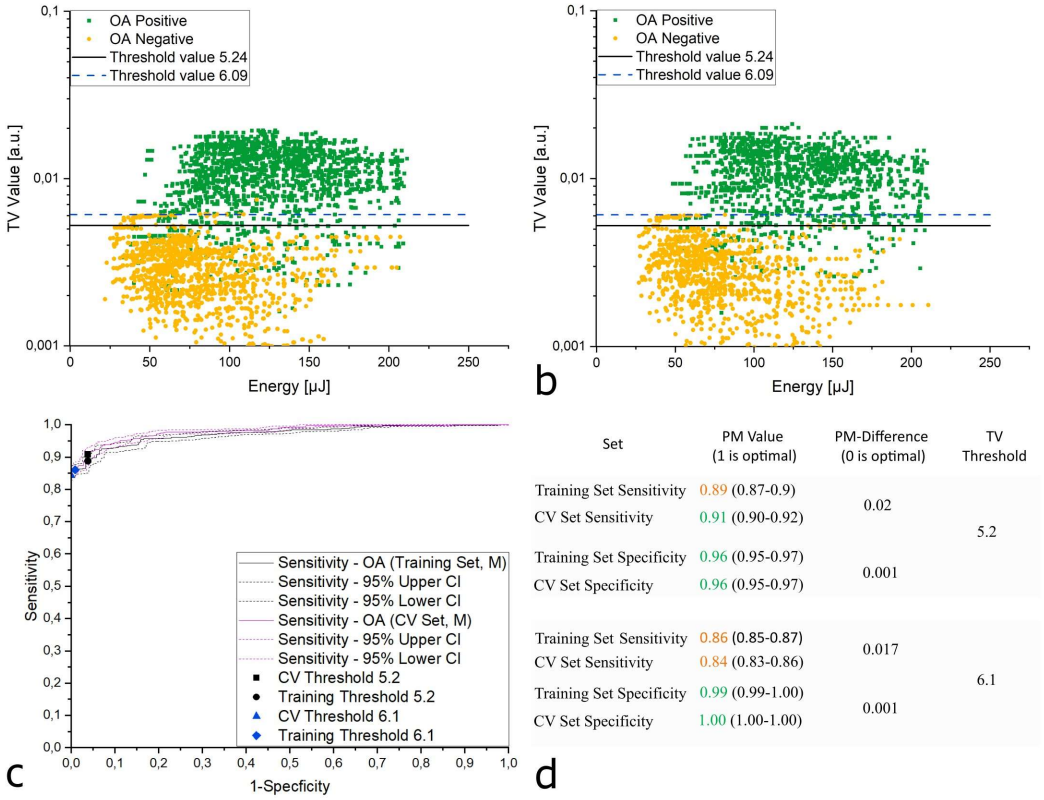

Set	PM Value (1 is optimal)	PM-Difference (0 is optimal)	TV Threshold
Training Set Sensitivity	0.89 (0.87-0.9)	0.02	5.2
CV Set Sensitivity	0.91 (0.90-0.92)		
Training Set Specificity	0.96 (0.95-0.97)	0.001	
CV Set Specificity	0.96 (0.95-0.97)		
Training Set Sensitivity	0.86 (0.85-0.87)	0.017	6.1
CV Set Sensitivity	0.84 (0.83-0.86)		
Training Set Specificity	0.99 (0.99-1.00)	0.001	
CV Set Specificity	1.00 (1.00-1.00)		

Figure 77. This scenario used the TV algorithm. Subfigure a shows the scatter plot of the training data set. Subfigure b presents the scatter plot of the CV dataset. Subfigure c depicts the ROC curves of the training and CV datasets with two threshold values highlighted in each curve. Subfigure d shows the performance metrics of the highlighted threshold values. The numbers in parentheses are the 95 % confidence intervals.

4.5.5 Association between OA value and FA visibility

BL algorithm

At a threshold of $BL = 125$, the Y-index (0.69) was highest in the CV set. The sensitivity in the CV set was 0.82 and the sensitivity in the test set was 0.87. These values were outside the 95 % confidence intervals of the datasets. The specificity in the CV set was 0.87, and the specificity in the test set was 1. Increasing the threshold level to $BL = 199$, which is where the specificity of 1 occurred in the CV set, led to a drop in sensitivity in the CV set to the 50 % mark (which is as good as a random decision). The specificity in the test set was 0.76. The PM-Difference of 0.25 was the largest difference measured in this study.

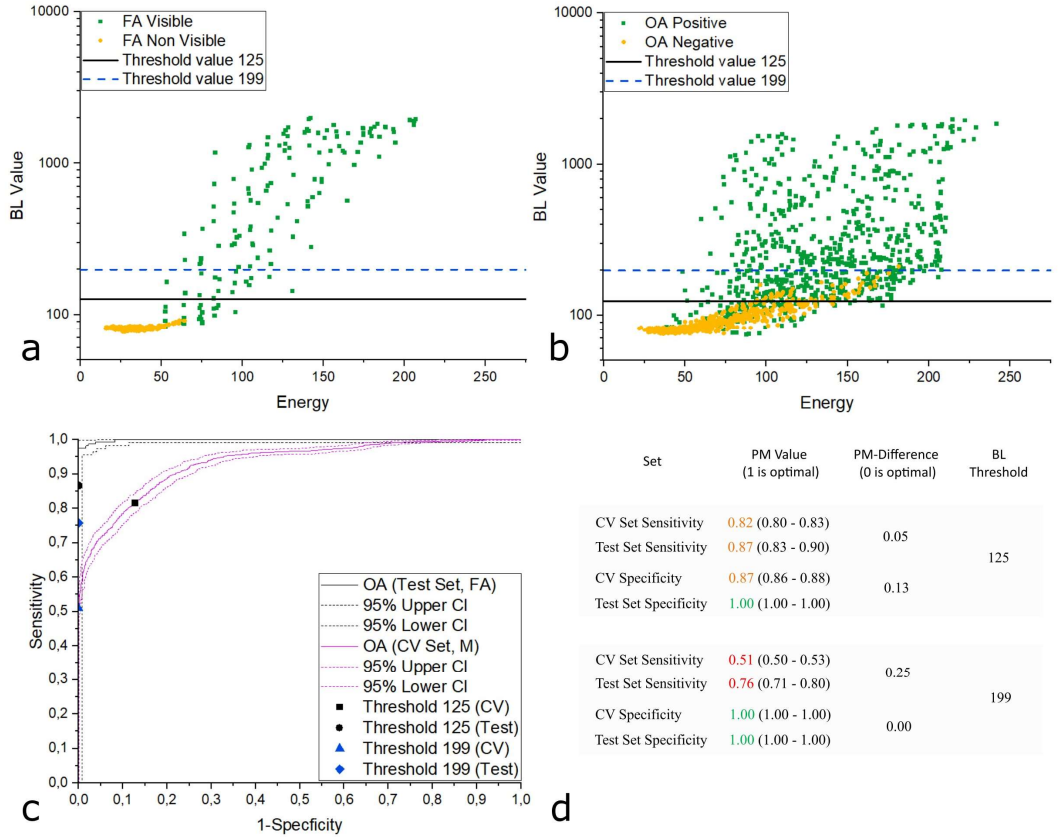

Figure 78. The BL algorithm was used in this scenario. Subfigure a depicts the scatter plot of test data set. Subfigure b shows the scatter plot of CV the dataset. Subfigure c presents the ROC curves of the test and CV datasets with two threshold values highlighted in each curve. Subfigure d shows the performance metrics of the highlighted threshold values. The numbers in parentheses are the 95 % confidence intervals.

NL algorithm

With a threshold value of $NL = 1.15$ (highest Y-index in the CV set), the NL algorithm led to a sensitivity of 0.92 in the CV set and 0.96 in the training set. The specificity was 0.97 and 1 for the CV and training sets, respectively. The false decisions of the test set are discussed in chapter 5.6.3. Increasing the threshold value to $NL = 1.23$ (which rendered a specificity of 1 in the CV set) caused the sensitivity in the CV and test sets to drop to 0.82 and 0.94, respectively.

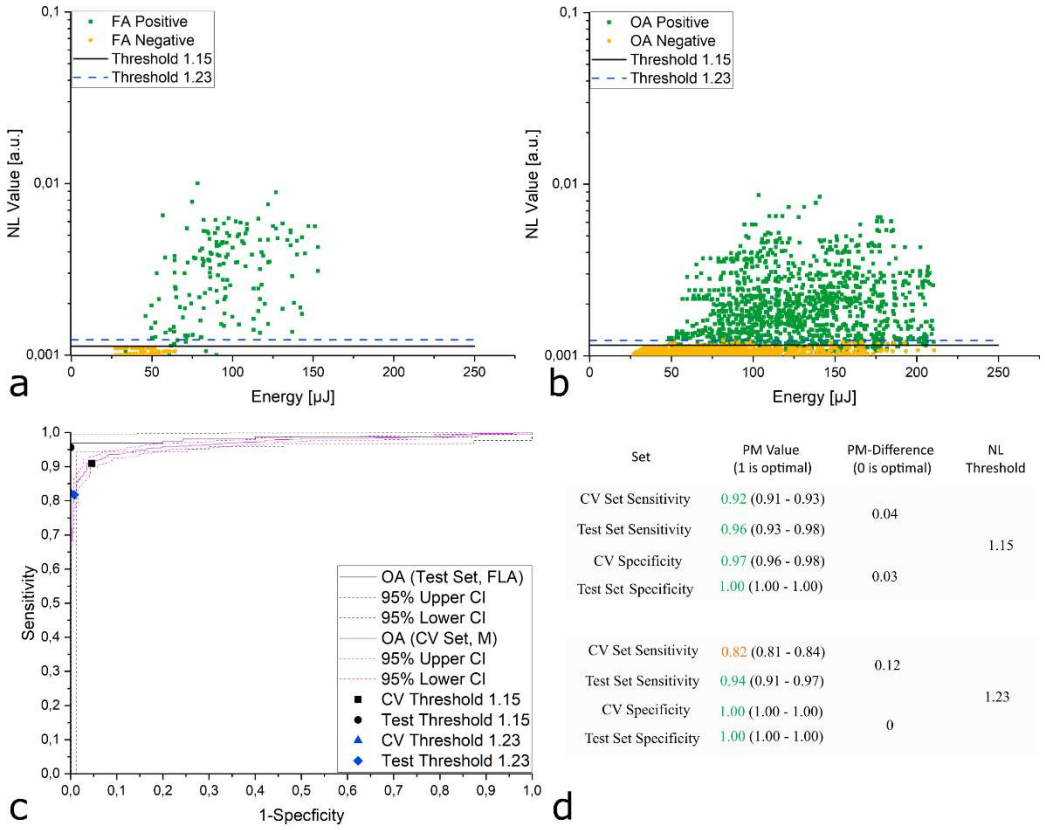

Figure 79. This scenario was run with the NL algorithm. Subfigure a presents the scatter plot of test data set. Subfigure b depicts the scatter plot of the CV dataset. Subfigure c shows the ROC curves of the test and CV datasets with two threshold values highlighted in each curve. Subfigure d depicts the performance metrics of the highlighted threshold values. The numbers in parentheses are the 95 % confidence intervals.

TV algorithm

At a threshold of TV=5.2, the TV algorithm achieved a sensitivity of 0.91 and 0.94 in the CV and test sets, respectively. Specificity values could be found at 0.96 for the CV set and 0.81 for the test set. Sensitivity values were inside the confidence intervals of the datasets, but the specificity values were not. Reasons for the false decisions that led to the performance metric difference are presented in chapter 5.6.3.

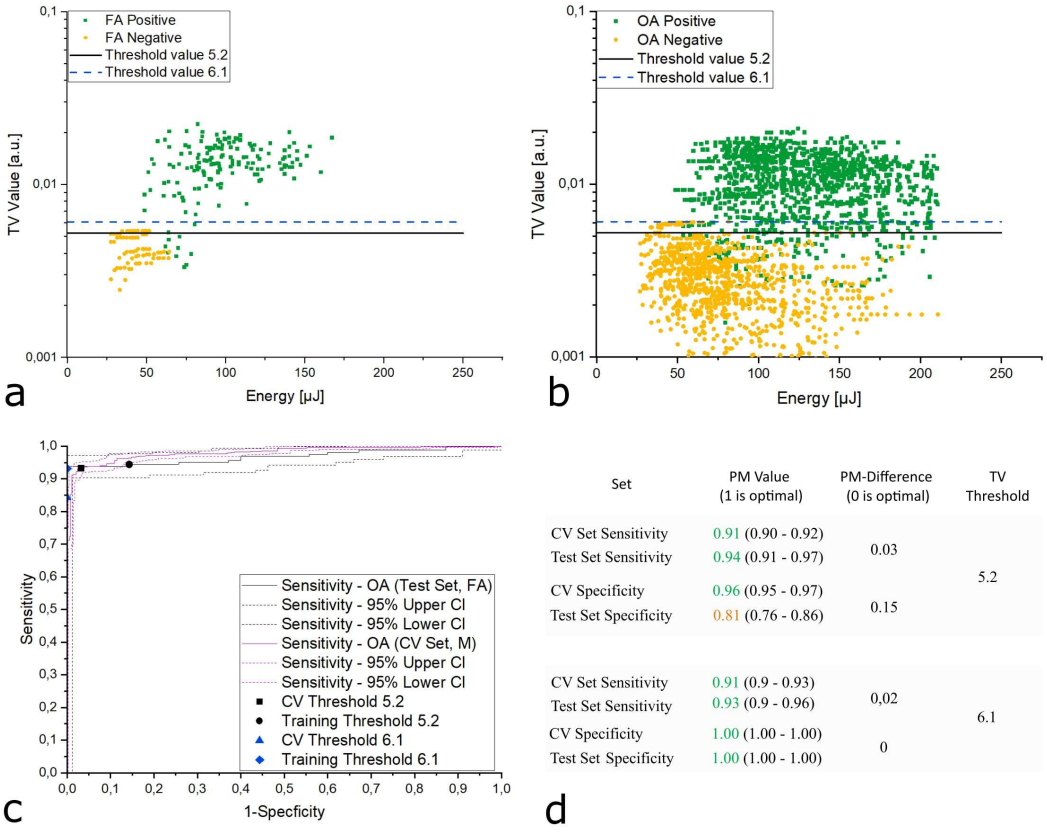

Set	PM Value (1 is optimal)	PM-Difference (0 is optimal)	TV Threshold
CV Set Sensitivity	0.91 (0.90 - 0.92)	0.03	5.2
Test Set Sensitivity	0.94 (0.91 - 0.97)		
CV Specificity	0.96 (0.95 - 0.97)	0.15	
Test Set Specificity	0.81 (0.76 - 0.86)		
CV Set Sensitivity	0.91 (0.9 - 0.93)	0,02	6.1
Test Set Sensitivity	0.93 (0.9 - 0.96)		
CV Specificity	1.00 (1.00 - 1.00)	0	
Test Set Specificity	1.00 (1.00 - 1.00)		

d

Figure 80. This scenario was done with the TV algorithm. Subfigure a presents the scatter plot of the test data set. Subfigure b depicts the scatter plot of the CV dataset. Subfigure c shows the ROC curves of the test and CV datasets with two threshold values highlighted in each curve. Subfigure d presents the performance metrics of the highlighted threshold values. The numbers in parentheses are the 95 % confidence intervals.

4.6 MBF based therapeutic window

4.6.1 Energy threshold

The actual standard of clinical practice is to choose a laser fix pulse energy and to perform a treatment with this chosen energy if no unintended effects are observed. Thus, the laser pulse energy served as a baseline method for the RM algorithm. The ED86 value for the upper 95 % confidence interval of the FA visibility was at 71.2 µJ. The ED16 for the lower 95 % confidence interval of the ophthalmoscopically visibility curve was at 149.3 µJ. The ratio of the $ED16_{oph}$ and $ED86_{FA}$ was 2.1. It should be noted that the lowest laser pulse energy for ophthalmoscopically visible effects was observed at 71.4 µJ. This was almost identical to the $ED86_{FA}$.

4.6.2 RM algorithm

For an RM threshold value of 0.012, the $\mathrm{ED86}$ energy for FA visibility was located at factor 1.11 above the $\mathrm{E_{Ref}}$. The $\mathrm{ED16}$ for ophthalmoscopic visibility was located at factor 2.32 above the $\mathrm{E_{Ref}}$. This led to a microbubble detection based therapeutic window of $\mathrm{TW_{\delta}} = 2.1$. The first ophthalmoscopically visible spot occurred at factor 1.92 above the reference energy.

4.6.1 NL algorithm

It should be highlighted that almost all ophthalmoscopically visible irradiations led to saturation of the sensor signal in the optoacoustic channel. Signal saturation was recognized by the algorithm´s safety procedures. During a real treatment, immediate ceasing of irradiation would be initiated together with a warning to significantly reduce the laser pulse energy. There were only two examples where there was no signal saturation and ophthalmoscopically visible damage. For an NL threshold value of 1.15, the $\mathrm{ED86}$ energy for FA visibility was located at factor 0.92 below $\mathrm{E_{Ref}}$, and the $\mathrm{ED16}$ for ophthalmoscopic visibility was located at factor 1.75 above $\mathrm{E_{Ref}}$. This led to a microbubble detection based therapeutic window of $\mathrm{TW_{\delta}} = 1.9$. The first ophthalmoscopically visible spot (which was not immediately extracted out by the safety routine) was located at factor 1.61 above $\mathrm{E_{Ref}}$.

4.6.2 TV algorithm

The NL algorithm used the safety procedures as the NL algorithm. Thus, only two ophthalmoscopically visible spots contributed to the corresponding probit plot. For a TV threshold value of 5.2, the separation between FA visible and FA non-visible spots was so high (specificity of one) that confidence intervals could not be calculated. The separation between FA visible and FA non-visible spots was at 0.77 of E_{Ref}. The $ED16$ for ophthalmoscopic visibility was located at factor 1.75 above E_{Ref}. The ratio between these values was 2.3. The first ophthalmoscopically visible spot that was not immediately extracted by the safety routines was located at 1.61.

5 Discussion

5.1 Pulse duration dependence of laser induced effects

5.1.1 Ex vivo threshold values

The primary cell damage mechanism at the lower microsecond regime was initially estimated to be a mere thermal effect.[141] Later, it was found that microbubble formation around melanosomes induced cell damage in the pico- and nano-second regime as well as in the lower microsecond regime.[149, 181, 182] A previous study on porcine RPE with optoacoustic microbubble detection and a pulsed laser demonstrated that thermal cell damage was induced with pulse durations of 500 µs.[159] In this previous study, a mixed damage effect was observed at 50 µs, and microbubble-induced cell damage was observed at 5 µs.[159] Other ex vivo experiments on optical microbubble detection with a scanning laser have reported "predominant microbubble-induced cell damage" for pulse durations up to 20 µs in bovine eyes.[158, 183]

In the present study, H_{cell} was found at a lower radiant exposure than H_{MBF} for pulses with a duration of 5 µs or longer. The origin of the difference may be explained by different assumptions regarding signal characteristics and technical differences. A similar observation was made in a previous study based on optoacoustic microbubble detection. In that study the optoacoustic pressure from thermoelastic expansion was assumed to be so low and that it could not be detected with the available sensors.[159] In this study, optoacoustic transients were also considered to be a result of microbubble formation, even if no cell damage had been observed. This assumption was not implausible, since other researchers have found microbubble formation without a simultaneous induction of cell damage.[158]

However, if this assumption is wrong, and some optoacoustic transients of thermoelastic origin have been acquired by the sensor elements, a false positive microbubble detection would be inevitable. Consequently, the evaluated radiant exposure threshold for MBF would have appeared to be lower than it really was.

The sensor elements in the present work (Ring Transducers with a resonance frequency around 1MHz) allowed for the detection of optoacoustic transients induced by thermoelastic expansions. Importantly, these sensor elements made the present method more sensitive than previous methods. Furthermore, the optoacoustic values were

processed differently in this work. In a previous work, the integral of the amplitude squared was used to calculate the OA values (E_A, equation 53).[159]

$$E_A = \int_0^{\tau_L} \big(P(t)\big)^2 dt \qquad 53$$

When the OA values (E_A) are calculated via equation 53, a linear increase in pressure leads to an nonlinear increase in the value of E_A. This makes discrimination between transients originating from thermoelastic expansions and those originating from microbubbles more difficult at the threshold radiant exposure close to H_{Cell}. This condition also increases the chances of false-positive microbubble detection. In the present work, the temporal point of transient appearance was used to detect microbubbles. This approach made a discrimination of transients with thermoelastic and thermomechanical origin possible.

It should be noted that high IMF values are not identical from pulse to pulse. A slight movement of the fiber, changes in temperature, or a change in the excited laser modes can induce a change in the measured IMF from pulse to pulse. The IMF of previous systems (Lutronic Corp R:GEN, IMF=3.8) was much larger than the IMF of the systems in the threshold study (ARC diode laser system, IMF=1.2).[159] A larger IMF can induce a larger spread of evaluated threshold values.

In the present study, the t-test was applied to gain information of whether H_{Cell} and H_{MBF} originate from the same population. Initial cell damage was located at a lower radiant exposure threshold than microbubble detection for pulses with a pulse duration of 5 µs and longer. For a pulse duration of 2 µs, the difference between H_{Cell} and H_{MBF} was around 8 mJ/cm². The t-test could not distinguish between the populations of microbubble formation and cell damage (the difference was not statistical significant). In contrast to a former study on bovine eyes that used a scanning laser and optical microbubble detection, there was no case of microbubble formation without cell damage.[158]

5.1.2 In vivo threshold values

This study found that the range from initial thermal damage to initial microbubble formation (microbubble delay) increases with pulse duration. The decrease in R_{MC} at a pulse duration of 12 µs in the in vivo data was expected to be a statistical fluctuation. It was assumed that thermal damage occurred at early stages of cell damage and was superimposed by mechanical damage when radiant exposure further exceeded the threshold for initial microbubble formation.

5.1.3 Pulse duration selection

Possible pulse durations for SRT treatments could be a low R_{MC} (ideally $R_{MC} = 1$) and a high R_{OM} and R_{OC}. A pulse duration of 5 µs may still be reasonable for this application, even though a slight difference between the cell damage threshold and microbubble formation threshold was found. However, pulse durations below 2 µs are preferred.

5.2 Optic design decisions for automated SRT system

The design of the V1 system was influenced by the design of a previous SRT-system. All features not related to the optical feedback had to be identical to the previous system to maintain conformity to existing risk evaluations. This includes a spot diameter of 200 µm. For the optical observation path, where no previous clinical knowledge existed, it has been decided to work with an aperture of 1 mm in diameter. This quite large aperture was chosen to make sure that even in the case of turbid anterior eye media the overall intensity at the sensor can be sufficiently high for evaluation.

The system modeling (processing chain from Microbubble growth, over Mie scattering, to Coherent optical imaging; displayed in Figure 25) was done after the design of the SRT systems. The simulations suggested small spots (50µm) to be better than large spots (200µm) when it comes to signal contrast. The simulation results have suggested that a design that would lead to the best signal contrast (low aperture, low spot size) would also lead to the lowest irradiance at the sensor.

5.3 Signal characterization

5.3.1 Fluctuations in received backscattered irradiance

The results of the simulations (Figure 25) demonstrate that randomly varying amplitude, phase, pulse shape, and beam profile can lead to differences in the photodiode-signal (integral and time evolution of backscattered irradiance), even under otherwise identical conditions (aperture, spot size, etc.). In this work, the spot-wise fluctuations predicted by the simulations were confirmed in animal trials and clinical treatments. In addition to spot-wise variations in the overall intensity, pulse-wise variations of the overall intensity were also observed. These fluctuations may have originated from breathing movements or saccades between the 150 or 300 ms (15 or 30 pulses with 100Hz) of an irradiation. A comparison with the first clinical trial conducted with the same system demonstrates that the pulse-to-pulse fluctuations were more pronounced in the clinical trial compared to preclinical trials. This supports the assumption that the pulse-to-pulse variations may be

induced by movements, since the eye is less fixated in a clinical treatment than in a preclinical treatment of an anesthetized rabbit.

Experimental examples of such variations can also be found in the literature. In their 2007 work, Lee et al. published graphs displaying the temporal course of backscattered light from the irradiation of bovine RPE. The spot diameter in this case was $16.7\ \mu m$. Examples of Lee et al.'s graphs are presented in Figure 19 (fundamentals chapter). The intensity of the acquired signal varied significantly between spots that were separated by only $50\ \mu m$.

5.3.2 Non-predictability of Modulations

The results have shown that number and size of microbubble induced modulations. Vary with the beam profile. Consequently, the signal contrast differed. Since the beam profile is random and temporally instable and und predictable, it is impossible to use microbubble induced modulation to predict the size of an induce lesion. Thus, modulations can only be used as a binary indicator for absence or presence of microbubbles. Consequently, the microbubble detection algorithm was designed to make such a binary decision.

5.4 Preclinical validation of optical microbubble detection

5.4.1 Threshold radiant exposure comparison

In a former study, an ED50 threshold of 143 mJ/cm² (95 % confidence interval from 101 mJ/cm² to 170 mJ/cm²) was evaluated.[164] Other studies, that have suggested an even lower radiant exposure threshold, did not consider the IMF. [21, 164] The most likely reason for the difference in threshold values is the technical differences between the setups and differences in the optical properties of the rabbit eyes. Regarding the differences in the setup, a lower repetition rate (100 Hz instead of 500Hz), a lower number of pulses per burst (30 instead of 100), and increased energy within a burst (first pulse starts at around 10 % of the maximum energy) were applied in this study. Each of these elements had the effect of increasing the threshold for retinal cell damage.[31]

5.4.2 Ophthalmoscopically visible spots

During the in vivo experiments with activated automatic irradiation ceasing (treatment ramp mode), ophthalmoscopically visible lesions were observed in some cases. It was even observed that the first pulse applied to such spots caused microbubble-induced modulations. At this point, it is important to note that in the first microbubble detection algorithm, each pulse's RM value was set in relation to the RM value of the first pulse in a

pulse train. This was done based on the assumption that the first pulse should always be below the threshold of microbubble formation. This first pulse served as a spot-individual reference. This setup led to the following failure process. If the backscattered light of a first pulse contained microbubble-induced modulations, the reference values (RM value of first pulse) were always higher than a case without modulations in the first pulse. Hence, the non-normalized RM values needed to rise to much higher values until the normalized RM values reached a predefined threshold. The radiant exposure threshold to achieve this was above the threshold for ophthalmoscopic visibility. The ophthalmoscopically visible lesions found in this study were induced by this mechanism.

5.4.3 Improvements of the algorithm

The results demonstrated that the frequency components of the laser pulse fluctuations are stable around 5 to 10 MHz. This allows for the possibility of filtering out these frequency components. Unfortunately, extracting these components can be expected to lower the microbubble-detection algorithms performance. Due to imperfections of the non-optimized algorithm, not all bursts were ceased immediately after the first sign of bubble formation. Therefore, improvements in the laser hardware and construction were required to reduce the unwanted modulations.

In this study, a low number of pulses (two to three) were applied with increasing energy after the threshold of bubble formation was reached. Such delayed ceasing is safe as long as the radiant exposure stays inside the therapeutic window. Even though working at the lower end of the therapeutic window increases safety, including in the case of algorithmic misjudgment, the RM algorithm should be better able to handle difficult cases. An improved microbubble detection algorithm has been developed. The algorithm version 3 (see chapter 3.3.2.2) is this latest version.

5.4.4 Selectivity of retinal lesions

Histology images revealed undamaged photoreceptor layers in a region where SRT lesions were assumed to be located. In addition, the images showed an accumulation of RPE cells in these regions as well. Similar accumulations of RPE cells have also been observed by Framme et al. in OCT images during follow-up observations of clinical SRT application.[184] The accumulations of RPE cells were not intended, and their effect on the function of the RPE is unknown.

In a previous study, it was reported that the RPE “was reformed by a single sheet of hypertrophic retinal pigment epithelium cells.”[185] In the former study, an intact RPE functionality was identified by the phagocytizing of the photoreceptor’s outer segments. In this study, the photoreceptor length in the treated area was equal to the photoreceptor length in the non-treated area. Main differences in the setups of this study and the previous include a pulse duration of $5\,\mu s$ and a repetition rate of 500 Hz. The pulse number varied.

Further investigation was done by other researchers with the rabbits treated in this study regarding photoreceptor functionality via electroretinogram (ERG). The researchers observed that there was “less functional loss than Pan Retinal Photocoagulation in both rod-mediated retinal function and cone-mediated retinal function.”[178] It should be mentioned that the observed eyes also had photocoagulation lesions that served as ophthalmoscopically visible marker lesions for orientation during treatment and diagnosis. The functional loss detected by the evaluation of the ERG data was most likely caused by the marker lesions and not by the SRT lesions.

5.4.5 Issues and limitations

Due to limitations in the available clinical working space, the setup could not be installed in a room in St Mary’s hospital. The setup had to be moved and reassembled for each treatment day (a one-hour process). Although the assembly process was executed systematically and with great care (by the author), it cannot be guaranteed that the system was identical in all aspects for each treatment day. Furthermore, after the first three treatment sessions, the slit lamp provided for the treatments needed to be changed due to incompatibilities between the optical paths of the slit lamp and the laser link. The illumination light of the slit lamp was discovered to reflect in the direction of the treating clinician at the dichroic filter of the laser link, inducing a blurry image of the rabbits retina. Further difficulties occurred during the diagnostic procedures. Since the FA camera was not compatible with the rabbit-holder, the animals needed to be held by hand. This induced a time delay from fluorescein-injection (done on stable ground) to image acquisition, making the process around two minutes or longer. Thus, only the late phase picture could be acquired. Since the rabbits could not be kept completely stable during image acquisition, some images had movement artifacts, which led to repeated acquisitions of the same area and further time delays. Consequently, evaluation of the FA images was difficult.

5.4.6 Attempted improvements

The preclinical study with the V1 SRT system demonstrated that it is possible to detect RPE damage before lesions become visible ophthalmologically during in vivo situations through the use of reflectometry as a primary feedback mechanism. The RM_{V1} algorithm[162] was able to quantify the cell damage if the system was used adequately. This was exhibited through successful automatic irradiation ceasing. However, the algorithm the implemented way the normalization procedure is done in this version of the algorithm makes is not a real single pulse microbubble detection technique, since each pulse is compared to the first pulse. To also be able to identify microbubbles in the first pulse the algorithm needs to be modified.

5.5 Validation of optical microbubble detection

5.5.1 Applicability of RM values for FA visibility detection

In the results chapter, it becomes apparent that microbubble-induced modulations in sensor data and FA visibility are strongly related to each other. However, the correlation was not perfect since performance metric (PM) differences between the training and test sets were observed. The differences were a result of several factors. Systematic differences in the performance of microbubble detection between a healthy test region and a diseased treatment region need to be considered. Mere statistical fluctuations in RM value distribution also need to be accounted for. To test for systematic differences in perfomance to detect microbubbles in test and treatment regions, performance metrics (sensitivity, specificity) to detect modulations in sensor data from these regions were compared. The RM difference between the CV and test sets was 0.02 for sensitivity and 0.05 for specificity. It can be assumed that the detection of microbubble-induced modulations in the sensor signal works almost equally well in the test spot as in treatment regions.

The difference in performance between the training set and the RM modulation labeled test set was smaller than the difference in performance between the training set and FA-classified test set. It can be assumed that difficulties associated with the labeling process of FA images may be the source of these differences. The most optimal way to solve this problem would be to add more data so that more strict exclusion criteria could be applied. Unfortunately, this action was not possible in this study.

To reduce the differences in distribution, the developed algorithm would need to be applied in a mode with automatic laser irradiation ceasing. This would result in an increased amount of data closer to the RM threshold for microbubble formation with FA-based classification. Unfortunately, automatic treatments were not possible in the treatment of patients.

5.5.2 False positive/negative decisions

The possibility of labeling problems is discussed in more detail in this chapter. This issue concerns namely false positives and false negatives. False negatives are datasets with signs of bubble formation (FA-visible) but with an incorrect algorithmic assignment of the opposite label (FA-nonvisible). These cases can lead to unwanted and potentially dangerous overtreatments. There were no false positives in the dataset for the case of a RM threshold of 0.012. False positives are spots without any sign of microbubble formation (FA-non-visible) but with an incorrect algorithmic assignment of the opposite class (FA-visible). A false-positive case occurs if the RM value is above the RM value threshold for an acquisition (30 Pulses) labeled as FA non-visible for at least one single pulse. There were seven false-positive pulses originating from five spots and four patients in this work.

In all false positive sensor data pulses, modulations were identified in the sensor data. In one case, modulations in the sensor data did not continue until the end of the pulse. This is unusual for larger microbubbles, but more common for laser pulse modulations of the applied pulses (as presented in chapter 4.3.2). Since the Version 3 system (R:GEN) did not store the applied laser pulses, whether these modulations originate from Mie scattering at the RPE or by modulations originating in the laser resonator cannot be verified.

5.5.3 Safety aspects

5.5.3.1 Microbubble detection based therapeutic window

It was made apparent in Figure 69a that RM values of FA-visible regions can be higher than RM values of ophthalmoscopically visible regions. Thus, knowledge regarding potential ophthalmoscopic visibility cannot be gained based solely on RM values.

As in previous SRT studies, a therapeutic window expresses the range from FA-visible to ophthalmoscopically visible effects. Despite the more conservative definition of the microbubble detection based therapeutic window (TW_δ; see chapter 3.10.4), it is still wider ($\mathrm{TW}_\delta = 2.1$) than the classic TW ($\mathrm{TW} = 1.69$) evaluated in former studies for a

series of 30 pulses of constant pulse energy, a pulse duration 1.7 µs, repetition rate 100 Hz, and a spot size 200 µm. These former studies have been defined as interindividual therapeutic windows in terms of radiant exposure ratios. This condition causes the lower TW boundaries to be influenced by eyes with a high FA-visibility energy threshold. These energy levels may be caused by low transparency of the anterior eye media and low RPE pigmentation. Similarly, the upper TW boundaries can be influenced by eyes with a low energy threshold for ophthalmoscopic visibility. Lowered upper TW boundaries may be caused by high transparency of the anterior eye media and high RPE pigmentation. However, with the microbubble detection-based definition presented in this work, interindividuality does not narrow the therapeutic window.

5.5.3.2 Adverse events

In contrast to conventional photocoagulation, SRT spots never caused bleedings in any study performed for this work (one preclinical study and three clinical studies). In the preclinical study on rabbits, an ophthalmoscopically visible discoloration of the retina may also be considered as an adverse event. However, the cause of this event was identified and solved with changes in the microbubble detection algorithm.

5.5.4 Limitations of the optical detection method

Despite the advantages of the optical microbubble detection technique, compared with arbitrary pulse energy selection, several influential factors need to be considered. Changes in the optical conditions of the anterior eye media may reduce the amount of backscattered light to an extent that makes the evaluation of the signal impossible. The optimization process was performed for only 15 eyes (10 were evaluable by FA imaging). This led to uncertainties in the statistical analysis (ROC and Probit). More data, especially more FA-nonvisible and ophthalmoscopically visible data, is required to reduce these uncertainties. Furthermore, all data belong to a certain sub-group (i.e., CSCR and DME patients). To include a larger variety of factors influencing the system performance, a larger sample size would be needed. In addition, a spot-related evaluation of the therapeutic window was not possible since there were not enough ophthalmoscopically visible spots with the first pulse below the threshold for bubble formation. A lower starting pulse energy (<50 % of maximum pulse energy) for the ramp could solve this problem for future studies.

5.6 Validation of optoacoustic microbubble detection

5.6.1 Baseline model

The generalizability of algorithmic performance can suffer when an algorithm is fine-tuned according to individual nuances in a dataset. This fact has been indicated through the increasingly different performance measures obtained from the datasets used in this work. Since no optimization or fine-tuning was done with the BL algorithm, low performance measure differences were achieved. Nevertheless, the performance measure differences between the training set and CV set, as well as the CV set and test set, were not zero. This raises the question of the origin of the apparent differences. Although the optical properties of the eye have low influence on the acoustic signal, variability in the acoustic coupling (contact lens to eye) and the angular dependence of the time evolution of the acoustic signal could have influenced the acquired transients.[136] In other words, under otherwise identical conditions, a signal from the periphery (test spots) may be lower in amplitude than a signal originating from the center (macula).

5.6.2 NL and TV algorithms

The acoustic pressure acquired by the ultrasonic transducer is proportional to the material specific Grüneisen coefficient, the radiant exposure (and consequently to the laser pulse energy), and the absorption coefficient. For each spot the absorption coefficient is assumed to stay constant over the time of irradiation, as long as no microbubble formation is induced. The laser pulse energy varies in the case if a pulse energy ramp is applied to one spot. Thus, the NL and TV algorithms included normalization procedures that eliminated the direct influence of the laser pulse energy on the NL and TV values. The spot wise changing absorption is taken care of by the design of the microbubble detection algorithms, which look for changes from a subthreshold condition (linear increase of pressure with laser pulse energy, or time invariance of time evolution of pressure transietns).

Thus, in the case of a constant Grüneisen coefficient, the NL and TV values should have been independent of the laser pulse energy. Evidence of the independence of the NL and TV values can be best seen in their low increase in the regime below microbubble formation in Figure 74. The existence of a low increase in NL and TV values in the regime below the threshold originated from the changing signal-to-noise levels of the evaluated transients. This phenomenon could be reduced if the signal-to-noise ratio were improved.

In the results section it was shown that the majority of all false negative decisions made by the NL algorithm shared the commonality that even the first pulse of the ramp led to microbubble formation. The first pulse induced microbubble formation, usually leads to decreased NL values and consequently to false negative decisions. The TV algorithm was able to identify microbubble formation from the second pulse on. All false positives with this algorithm originated from the noise influences of one single spot, and these noise influences were unique for each pulse. Individual noise-peaks were perceived as microbubble-induced transient-to-transient fluctuations to the algorithm. If a peak induced a false decision at an early pulse, all the following pulses were false positives as well. The low number of microbubble-associated characteristics in the false-negative data could be further reduced with filtering techniques, which are required to reduce the noise level. An improvement of the sensor sensitivity or an improvement of the analog amplification would reduce the necessity of filtering and lead to a decreased number of this type of false decision.

Knowledge about the state of MBF, including knowledge of the first pulse (which is independent from the signal-to-noise level of the acquired transients) could be gained through an optical feedback mechanism.[179] Hence, it can be speculated that a combination of the optoacoustic feedback techniques with an optical feedback technique would improve combined sensitivity and specificity.

5.6.3 False positive/negative decisions

With regard to the BL algorithm, there were 22 false negative decisions and zero false positive decisions in the test dataset when a threshold value of 125 was applied. The pulse energy dependence was found to induce a systematic error. This systematic error has already been outlined in chapter 4.5.3. The NL and TV algorithms were designed to remove this systematic error.

The NL algorithm led to zero false positive decisions and six false negative decisions in the test dataset when a threshold value of 1.15 was applied. In four of the six false negative decisions made by the NL algorithm, the chosen pulse energy of the first pulse was so high that it even displayed signs of microbubble formation. In such a case the steep increase in optoacoustic amplitude, which occur at the transition from thermoelastic to thermomechanical cell damage, could be observed. The early microbubble formation was detected via comparisons with an optical feedback technique that is able to detect microbubbles by evaluating single pulses.[179] In the remaining two false negative

decisions, the microbubble-associated characteristics were hard to detect even by the gold standard: a human observer. However, human error in making the gold-standard decision cannot be excluded.

With regard to the TV algorithm, there were nine false negative decisions and 10 false positive decisions in the test dataset when a threshold value of 5.2 was used. All nine false positive decisions originated from the same spot with a low-pressure amplitude and high-frequency noise. The false negative decisions originated from nine spots. For all of these spots, the microbubble-associated characteristics were minute.

5.6.4 Limitations of the acoustical detection method

The optimization process was performed for only 15 eyes (10 were evaluable by FA imaging). This led to uncertainties in the statistical analysis. The treatment protocol, which had to be followed to ensure a safe and effective treatment, introduced a higher number of FA-visible and OA-positive spots compared to FA-nonvisible and OA-negative spots. More data, especially more FA-nonvisible and ophthalmoscopically-visible data, is required to improve the statistical evaluation.

6 Summary

It was the aim of this work to develop an algorithm for the prediction of selective RPE damage which can be used for treatment automatization in SRT treatments. The prediction of RPE damage shall be based on the prediction of microbubble formation. For this reason, it is important that microbubble formation is the origin of cell death at the threshold of selective RPE cell death. Thus, it has been looked out for the pulse duration where the threshold for microbubble formation is statistically not discriminable from the threshold of cell damage. Microbubble formation thresholds were detected by a novel optoacoustic approach which uses the time until microbubble formation and the time evolution of the laser power to evaluate the required radiant exposure.

In ex vivo experiments on porcine explants, at a pulse duration of 5 µs, the threshold for cell damage (465 mJ/cm²) was still lower than the threshold for microbubble detection (500 mJ/cm²). This spread increased with increasing pulse duration. For a pulse duration of 2 µs, the difference between the H_{Cell} and H_{MBF} was around 8 mJ/cm² (3% difference). This difference was not statistically significant. During the in vivo experiments and clinical studies that followed, a pulse duration of 1.7 µs, a wavelength of 527 nm, and a repetition rate of 100 Hz were applied.

Similarly, in in vivo experiments on rabbits, the threshold for cell damage (239 mJ/cm²) was lower than the threshold for microbubble detection (344 mJ/cm²) at a pulse duration of 5 µs. Again, the difference in threshold values for cell damage and microbubble detection was observed to increase with increasing pulse duration. At 5 µs, a t-test resulted in *p* values of 0.003 for the ex vivo experiments. All threshold-differences between the MBF and cell damage remained statistically significant for longer pulse durations. The threshold for 2µs could not be evaluated in vivo due to a low maximum laser power.

Simulations of the entire signal chain (microbubble growth, mie scattering, coherent optical propagation) were performed to study the influence of optic design decisions and instable side conditions, including movements during irradiation on the signal acquired by the photodiode (optical microbubble detection). Therefore, the time evolution of microbubbles was needed to be estimated by solving the Rayleigh-Plesset equation. The models used for the calculation of bubble dynamics assumed the existence of one

spherical bubble. Effects like thermal isolation of the absorbing particles by the microbubble, scattering of laser light by the microbubble, and bubble movement (thermal convection) were not considered in this model.

The model for optical propagation consisted of 2 lenses of equal focal length in a distance to each other of twice the focal length. The model considered an aperture stop between the lenses at the point of the focal lengths. The diameter of the aperture and the size of the spot can be varied. Calculations were done for two polarizations and the sum of both intensities (unpolarized light) was considered as input for the photodiode.

The simulation suggested the best signal contrast is obtained with a low aperture diameter (200 µm) and a low spot diameter (5 µm). An increase in aperture diameter or spot diameter results in a reduction in the signal contrast of the microbubble induced signal in the simulated sensor data.

The simulations have also shown that larger bubbles lead to larger modulations. Which raised the question, whether the microbubble diameter can be predicted. Unfortunately, the simulations have also shown that the two-dimensional distribution of laser power within the irradiated area (beam profile) has an influence on the modulations in the acquired signal. The beam profile is characterized by the number, location, and intensity of hotspots where the irradiance is highest. During a measurement the exact beam profile is unknown at the time of irradiation since the beam profile can change over time. Thus, predictions regarding the microbubble size cannot be made.

Another issue is induced by backscattering of the coherent treatment light. From a wave optical perspective, this leads to a random distribution of the amplitude and phase values in the object plane. Those random values are affected by many influences (among others by changes in location). The acquired signal is a complex interference pattern of all neighboring regions. If the random values of amplitude and phase change, the interference pattern changes. Even if there is no microbubble (modulation free signal). The changes in the modulation free signal, were confirmed by the in vivo experiments and clinical data.

To validate the performance of automatic treatment systems, a clinically applicable device was built. Using the first SRT clinic device (built by Medizinisches Laserzentrum Lübeck GmbH), a preclinical trial on chinchilla gray rabbits was performed. Compromises were needed to be made in the optical design, regarding the aperture diameter and the spot

diameter. A 200 µm aperture could not be used, since the resulting drop in power received by the photodiode, was expected to be too low to lead to evaluable signal to noise levels. An aperture of 1mm was used instead. Furthermore, a spot size of 200 µm was applied to meet clinical requirements and to keep conformity with previous systems. The SRT system was able to increase the laser pulse energy for a series of 30 pulses at 100Hz (ramp).

Optical and optoacoustical microbubble detection was implemented, and automatic irradiation ceasing of the ramp was performed with the optical microbubble detection (RM_{V1} algorithm). Information about presence or absence of RPE cell damage was gained by fluorescein angiography. Selective lesions were achieved with automatic irradiation ceasing. The radiant exposure levels of selective lesions ranged from below 200 mJ/cm² up to values above 1000 mJ/cm² (highest laser pulse energy in the ramp). Corresponding OCT images did not show any visible changes in the SRT irradiated areas. Histological and electrophysiological observations suggested an undamaged photoreceptor layer in the region treated with the SRT. In histological images, an accumulation of RPE cells was observed in regions associated with SRT irradiation. However, the implemented way of how the normalization procedure was done in the RM_{V1} algorithm makes it not a real single pulse microbubble detection technique, since each pulse is compared to the first pulse.

For a following clinical studies the algorithm to evaluate the photodiode signals was improved to require just one single backscattered pulse for microbubble detection. Furthermore, two optoacoustic signals have been evaluated. One was designed to detect a nonlinear increase in optoacoustic amplitude compared to the linearly increasing laser pulse energy (NL algorithm) and the other one was designed to detect differences in the time evolution of sequential optoacoustic pressure transients (TV algorithm).

Clinical trials for the treatment of CSR and DME (15 patients) were performed to evaluate the system's ability to work under more unstable conditions, like turbid eye media, movements (saccades) and diseased retinal regions. A pulsewise increase laser pulse energy over 15 pulses was applied without automatic irradiation ceasing. The sensor data was labeled with technical data (MBF characteristics in sensor data) and diagnostic data (visibility in fluorescein angiography). Automatic optimization procedures (Gradient Descent) were applied to the algorithms to find the optimal settings for discrimination between signals with and signals without signs of MBF. The optimization process, the

selection of a threshold value, and the final test on the performance to discriminate data from irradiation which induced cell damage from those which did not ,was done with data of different patients. Cell damage was evaluated by fluorescein angiography.

In a training set the improved RM_{V3} algorithm achieved a sensitivity of 1.00 and a specificity of 0.93 to correctly predict FA visibility in a test set. The NL algorithm and the TV algorithm (both calculated with optoacoustic signals) achieved a sensitivity of 0.96 (NL) and 0.94 (TV) and a specificity of 1.00 (NL) and 0.81 (TV). The RM, NL, and TV approaches were found to be superior to the baseline methods (e.g. selecting a fix laser pulse energy).

In clinical practice, it may turn out to be reasonable to treat above the threshold for bubble formation. In such cases, it is acceptable to use a factor by which the laser pulse energy can exceed the threshold for MBF instead of the RM or OA value. This is because the RM and OA values are not explicitly designed to scale with cell damage. Furthermore, a dose response method (probit analysis) has shown that RM, NL, and TV bubble detection thresholds may be exceeded by a factor of 1.2 without a major risk of inducing ophthalmoscopically visible lesions.

In conclusion, automated SRT can be performed under clinical conditions with optical or optoacoustic approaches with the presented systems and algorithms.

From a technical aspect, future work about automated SRT should focus on improving the sensor elements with respect to sensitivity [V/bar], since most difficulties in this project originated from disturbed signal and noise.

From a economic aspect, the financial reimbursement of DME and CSCR treatments are not high enough to justify the cost of a SRT system. Therefore, the potential of SRT on other RPE-related diseases like dry age related macula degeneration should be investigated.

7 Appendix

Overview of interferometric techniques

The mathematical models in this work made use of the time independent complex amplitude (phasor) to describe the light wave (details in chapter 2.7).

$$U(r) = a(r)e^{i\varphi(r)} \quad \textbf{54}$$

In this equation, which describes a plane wave, U is the optical field, r is the point in space, a is the amplitude, and φ is the phase. The irradiance (sometimes called optical intensity) I [W/m²] can be detected by sensors (e.g., photodiodes). It is defined by:

$$I = |U(r)|^2 \quad \textbf{55}$$

If a plane wave is reflected by a deformed surface, the temporal or spatial change in surface height h can be expressed as a ratio of the wavelength of the incoming light (phase difference).

$$\Delta\varphi = (\mathrm{h}(\mathrm{x}_1, \mathrm{y}_1, t_1) - \mathrm{h}(\mathrm{x}_2, \mathrm{y}_2, \mathrm{t}_1))\frac{2\pi}{\lambda} \quad \textbf{56}$$

A typical way to evaluate surface deformations of a plane is interferometry. In this approach, reflected light of the specimen irradiating beam interferes with a reference beam, of the same light source, at the sensor (see Figure 81 a1). The intensity I at the sensor is determined by the stable reference wave U_1 and the spatially varying (or temporally varying) probing wave U_2 (Figure 81 a3).

$$I = \langle |U_1 - U_2|^2 \rangle = I_1 + I_2 + 2(I_1 I_2)^{\frac{1}{2}} \cos(\varphi_2 - \varphi_1) \quad \textbf{57}$$

The spectral bandwidth of the light source $\Delta\nu_C$ determines the time interval τ_C (coherence time) in which emitted light can interfere with light of the same source. If the optical path difference significantly exceeds the coherence length $l_C = c\tau_C$ (with the speed of light c), interface effects do not occur. Interferometers usually make use of light sources with a short spectral line width. The resulting long coherence length enables measurements over longer distances (Figure 81 a2). Such techniques can be applied to observe changes in the size of objects like micrometer-sized bubbles (see chapter 2.4.5). In another technique, a light source with a broad spectral range (short coherence length) may be applied to an interferometric setup with a variable reference arm to enable depth

scans of scattering media. Since scattering increases the optical path length and the coherence time is noticeably short, only those photons that (a) were scattered back directly (ballistic photons) and (b) were at the same distance from the sensor as the reference arm can contribute to the interference signal (other photons received by the sensor are considered as physical noise). Figure 81 b1 displays the schematic of such an optical coherence tomography (OCT) device. If the reference arm scans over a distance identical to different layers in an object, the location of the layers can be distinguished in the interference pattern. This is illustrated in Figure 81 b2. The shorter the coherence length, the lesser the influence of distant regions is (see Figure 81 b3; small pointers). A single OCT scan can is referred to as an A-scan. A stacked series of spatially neighboring A-scans (cross sectional image of A-scans) is called a B-scan. In this work, B-scans of the fundus (retina and RPE) were used to illustrate retinal diseases and effects of laser irradiation. The described interferometric techniques are typically applied on surfaces or volumes with a surface roughness much smaller than the wavelength of the measurement light. If an extended surface or scattering volume is illuminated with coherent light (Figure 81 c1), a random interference pattern can be found at the senor (Figure 81 c2). Such an interference pattern shows bright and dark regions referred to as a speckle pattern. The properties of a speckle pattern are described in statistical terms by speckle variance techniques. The number of phasors contributing to the interference pattern are determined by the roughness of the object, the illuminated area, the polarization, and other optic design parameters (details in chapter 2.7). Figure 81 c3 illustrates the geometrical addition process of multiple random phasors (random walk). In this work, it is shown that the effects of speckle effects have a big influence on optical microbubble detection techniques.

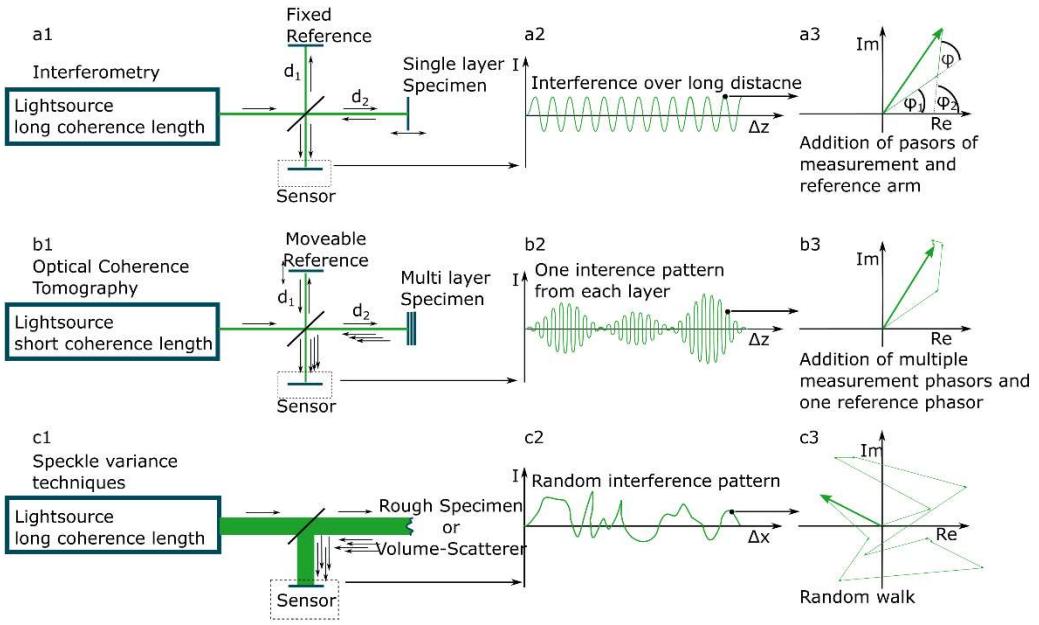

Figure 81. A Michelson interferometer (a1) makes use of the interference of a stable reference beam and a probing beam. Due to the long coherence length of the light source, an interference of these two beams can be detected over a long range (a2). Since the number of interfering waves is limited to two and the reference wave is kept stable over time, measurements of the relative phase change can be made (a3). A classical OCT (b1) system makes use of a short coherence wavelength with a movable reference arm to scan through a scattering media. Layers of changing scattering properties can be distinguished well (b2). The shorter the coherence length, the less influence neighboring regions have on scan direction (b3, tiny pointers). If the surface roughness is not significantly larger or smaller than the wavelength, the random height differences of the surface translate into random phase differences (c1). Thus, the phase at the sensor is distributed randomly as well (c2). The random interference pattern is called a speckle pattern. The phasor sum is a result of a random walk (c3).

8 References

[1] V. Czerny, [Über Blendung der Netzhaut durch Sonnenlicht], (1867).

[2] R. Deutschmann, "Ueber die Blendung der Netzhaut durch directes Sonnenlicht," Arch. f. Ophth, 28, 241 (1882).

[3] G. Meyer-Schwickerath, "Koagulation der Netzhaut mit Sonnenlicht," Berichte der Deutschen Ophthalmologischen Gesellschaft, 55(1), 256-259 (1949).

[4] H. Littmann, "Der Zeiss-Lichtkoagulator nach Meyer-Schwickerath mit Xenonhochdrucklampe," Ber Dtsch Ophthalmol Ges, 61, 311-316 (1957).

[5] A. L. Schawlow, and C. H. Townes, "Infrared and optical masers," Physical Review, 112(6), 1940 (1958).

[6] T. H. Maiman, "Stimulated optical radiation in ruby," Nature, (1960).

[7] M. M. Zaret, G. M. Breinin, H. Schmidt, H. Ripps, I. M. Siegel, and L. R. Solon, "Ocular lesions produced by an optical maser (laser)," Science, 134(3489), 1525-1526 (1961).

[8] C. Campbell, C. Koester, V. Curtice, K. Noyori, and C. Rittler, "Clinical studies in laser photocoagulation," Archives of Ophthalmology, 74(1), 57-65 (1965).

[9] Z. Flocks, "Laser coagulation of ocular tissues," Archives of Ophthalmology, 72(5), 604-611 (1964).

[10] V.-P. Gabel, R. Birngruber, and F. Hillenkamp, "Visible and near infrared light absorption in pigment epithelium and choroid," Proc. 23rd Consilium Ophthalmologicum, Kyoto Excerpta Medica, 450, 658-62 (1978).

[11] Birngruber, "Choroidal circulation and heat convection at the fundus of the eye," Laser Applications in Medicine and Biology, 5, 277-361 (1991).

[12] J. Roider, R. Brinkmann, C. Wirbelauer, H. Laqua, and R. Birngruber, "Subthreshold (retinal pigment epithelium) photocoagulation in macular diseases: a pilot study," Br J Ophthalmol, 84(1), 40-47 (2000).

[13] C. Klatt, H. Elsner, E. Poerksen, R. Brinkmann, A. Bunse, R. Birngruber, and J. Roider, "Selective retina therapy in central serous chorioretinopathy with detachment of the pigmentary epithelium," Ophthalmologe, 103(10), 850-855 (2006).

[14] J. Roider, S. H. M. Liew, C. Klatt, H. Elsner, E. Poerksen, J. Hillenkamp, R. Brinkmann, and R. Birngruber, "Selective retina therapy (SRT) for clinically significant diabetic macular edema," Graefes Arch Clin Exp Ophthalmol, 248(9), 1263-1272 (2010).

[15] J. Roider, S. H. M. Liew, C. Klatt, H. Elsner, E. Pörksen, J. Hillenkamp, R. Brinkmann, and R. Birngruber, "Selective retina therapy (SRT) for clinically significant diabetic macular edema," Graefes Arch Clin Exp Ophthalmol, 248(9), 1263-1272 (2010).

[16] C. Klatt, M. Säger, T. Oppermann, E. Poerksen, F. Treumer, J. Hillenkamp, E. Fritzer, R. Brinkmann, R. Birngruber, and J. Roider, "Selective retina

therapy for acute central serous chorioretinopathy," Br J Ophthalmol, 95(1), 83-88 (2011).
[17] R. R. Anderson, and J. A. Parrish, "Selective photothermolysis: precise microsurgery by selective absorption of pulsed radiation," Science, 220(4596), 524-527 (1983).
[18] Roider, Michaus, Flotte, and Birngruber, "Mikrokoaguation am Augenhintergrund," Fortschirotte in der Ophthalmologie, 88, 473-476 (1991).
[19] J. Roider, F. Hillenkamp, T. Flotte, and R. Birngruber, "Microphotocoagulation: Selective Effects of Repetitive Short Laser Pulses," Proc. Natl. Acad. Sci. USA, 90 (6), 8643-7 (1993).
[20] J. Roider, N. Michaud, T. Flotte, and R. Birngruber, "Histologie von Netzhautlasionen nach kontinuierlicher Bestrahlung und nach selektiver Mikrokoagulation des retinalen Pigmentepithels," Der Ophthalmologe, 90(3), 274-278 (1993).
[21] J. Roider, N. A. Michaud, T. J. Flotte, and R. Birngruber, "Response of the Retinal Pigment Epithelium to Selective Photocoagulation," Arch. Ophthalmol., 110(12), 1786-1792 (1992).
[22] Brinkmann, and Birngruber, "Selektive Retina-Therapie (SRT)," z. Med. Phys., (2006).
[23] J. Neumann, and R. Brinkmann, "Cell disintegration by laser-induced transient microbubbles and its simultaneous monitoring by interferometry," Journal of biomedical optics, 11(4), 041112-041112 (2006).
[24] C. P. Lin, and M. W. Kelly, "Ultrafast time-resolved imaging of stress transient and cavitation from short-pulsed laser irradiated melanin particles." 2391, 294-299.
[25] J. Neumann, and R. Brinkmann, "Cell disintegration by laser-induced transient microbubbles and its simultaneous monitoring by interferometry," J Biomed Opt, 11(4), 041112 (2006).
[26] R. Brinkmann, G. Huettmann, J. Roegener, J. Roider, R. Birngruber, and C. P. Lin, "Origin of retinal pigment epithelium cell damage by pulsed laser irradiance in the nanosecond to microsecond time regimen," Lasers Surg Med, 27(5), 451-464 (2000).
[27] G. Schuele, H. Elsner, C. Framme, J. Roider, R. Birngruber, and R. Brinkmann, "Optoacoustic real-time dosimetry for selective retina treatment," Journal of biomedical optics, 10(6), 064022-064022 (2005).
[28] G. Schüle, M. Rumohr, G. Hüttmann, and R. Brinkmann, "RPE damage thresholds and mechanisms for laser exposure in the µs to ms time regimen," Inv Ophthalmol & Vis Sci, 46(2), 714-719 (2005).
[29] E. A. Boettner, and J. R. Wolter, "Transmission of the ocular media," Investigative Ophthalmology Visual Science, 1(6), 776-783 (1962).
[30] W. Geeraets, R. C. Williams, G. Chan, H. William, G. Dupond, and F. Schmidt, "The relative absorption of thermal energy in retina and choroid," Invest Ophthalmol, 1, 340-347 (1962).
[31] C. Framme, G. Schuele, J. Roider, R. Birngruber, and R. Brinkmann, "Influence of pulse duration and pulse number in selective RPE laser treatment," Lasers Surg Med, 34(3), 206-215 (2004).

[32] G. Schuele, E. Joachimmeyer, C. Framme, J. Roider, R. Birngruber, and R. Brinkmann, "Optoacoustic control system for selective treatment of the retinal pigment epithelium." 4256, 71-76.
[33] H.-L. Liou, and N. A. Brennan, "Anatomically accurate, finite model eye for optical modeling," J. Opt. Soc. Am., 14(8), 1684-1695 (1997).
[34] M. Guillon, D. P. Lydon, and C. Wilson, "Corneal topography: a clinical model," Ophthalmic Physiol Opt, 6(1), 47-56 (1986).
[35] Y. Yang, K. Thompson, and S. A. Burns, "Pupil location under mesopic, photopic, and pharmacologically dilated conditions," Invest Ophthalmol Vis Sci, 43(7), 2508-2512 (2002).
[36] G. Walsh, "The effect of mydriasis on the pupillary centration of the human eye," Ophthalmic Physiol Opt, 8(2), 178-182 (1988).
[37] N. Brown, "The change in lens curvature with age," Exp Eye Res, 19(2), 175-183 (1974).
[38] Artal, [Age-Related Changes of the Human Eye] Humana Press, (2008).
[39] S. Heegaard, O. A. Jensen, and J. U. Prause, "Structure and composition of the inner limiting membrane of the retina. SEM on frozen resin-cracked and enzyme-digested retinas of Macaca mulatta," Graefes Arch Clin Exp Ophthalmol, 224(4), 355-360 (1986).
[40] S. Omri, B. Omri, M. Savoldelli, L. Jonet, B. Thillaye-Goldenberg, G. Thuret, P. Gain, J. C. Jeanny, P. Crisanti, and F. Behar-Cohen, "The outer limiting membrane (OLM) revisited: clinical implications," Clin Ophthalmol, 4, 183-195 (2010).
[41] J. J. Weiter, F. C. Delori, G. L. Wing, and K. A. Fitch, "Retinal pigment epithelial lipofuscin and melanin and choroidal melanin in human eyes," Invest Ophthalmol Vis Sci, 27(2), 145-152 (1986).
[42] Birngruber, Boergen, Drechsel, Gabel, Hillenkamp, Welsch, and Lund, "Untersuchungen zur Lichtabsorption am Auge," Gesellschaft für Strahlen und Umweltforschung mbH München, 277, 1-22 (1978).
[43] H. G. Birngruber, [Experimentelle und theoretische Untersuchungen zur thermischen Schaedigung des Augenhintergrundes durch Laserstrahlung] Gesellschaft fuer Strahlen-und Umweltforschung, (1978).
[44] V. P. Gabel, R. Birngruber, and F. Hillenkamp, [Die Lichtabsorption Am Augenhintergrund] Augenklinik der Universität München, (1976).
[45] Lachenmayer, Birngruber, and Gabel, "The wavelengthdependence of light absorption in the Fundus of the eye," Docum. Ophthal. Proc. Series, 36, 3-10 (1984).
[46] L. J. Rizzolo, "Development and role of tight junctions in the retinal pigment epithelium," International review of cytology, 258, 195-234 (2007).
[47] J. Cunha-Vaz, R. Bernardes, and C. o. Lobo, "Blood-retinal barrier," European journal of ophthalmology, 21, S3-S9 (2011).
[48] R. Simo, M. Villarroel, L. Corraliza, C. Hernandez, and M. Garcia-Ramirez, "The retinal pigment epithelium: something more than a constituent of the blood-retinal barrier--implications for the pathogenesis of diabetic retinopathy," Journal of biomedicine and biotechnology, 2010, 190724 (2010).

[49] R. Simo, E. Carrasco, M. Garcia-Ramirez, and C. Hernandez, "Angiogenic and antiangiogenic factors in proliferative diabetic retinopathy," Current diabetes reviews, 2, 71-98 (2006).
[50] M. Lu, M. Kuroki, S. Amano, M. Tolentino, K. Keough, I. Kim, R. Bucala, and A. P. Adamis, "Advanced glycation end products increase retinal vascular endothelial growth factor expression," The Journal of clinical investigation, 101, 1219-1224 (1998).
[51] M. D. Sternfeld, J. E. Robertson, G. D. Shipley, J. Tsai, and J. T. Rosenbaum, "Cultured human retinal pigment epithelial cells express basic fibroblast growth factor and its receptor," Current eye research, 8, 1029-1037 (1989).
[52] M. S. Burns, and M. J. Hartz, "The retinal pigment epithelium induces fenestration of endothelial cells in vivo," Current eye research, 11, 863-873 (1992).
[53] W. G. Roberts, and G. E. Palade, "Increased microvascular permeability and endothelial fenestration induced by vascular endothelial growth factor," Journal of cell science, 108 (Pt 6), 2369-2379 (1995).
[54] M. Saint-Geniez, T. Kurihara, E. Sekiyama, A. E. Maldonado, and P. A. D'Amore, "An essential role for RPE-derived soluble VEGF in the maintenance of the choriocapillaris," Proceedings of the National Academy of Sciences of the United States of America, 106, 18751-18756 (2009).
[55] G. L. King, and K. Suzuma, "Pigment-epithelium derived factor a key coordinator of retinal neuronal and vascular functions," New England Journal of Medicine, 342(5), 349-351 (2000).
[56] D. Lanneau, A. de Thonel, S. Maurel, C. Didelot, and C. Garrido, "Apoptosis versus cell differentiation: role of heat shock proteins HSP90, HSP70 and HSP27," Prion, 1, 53-60 (2007).
[57] J. T. Beckham, G. J. Wilmink, M. A. Mackanos, K. Takahashi, C. H. Contag, T. Takahashi, and E. D. Jansen, "Role of HSP70 in cellular thermotolerance," Lasers in surgery and medicine, 40, 704-715 (2008).
[58] M. N. Rylander, Y. Feng, J. Bass, and K. R. Diller, "Thermally induced injury and heat-shock protein expression in cells and tissues," Annals of the New York Academy of Sciences, 1066, (2005).
[59] C. Soti, E. Nagy, Z. Giricz, L. Vigh, P. Csermely, and P. Ferdinandy, "Heat shock proteins as emerging therapeutic targets," British journal of pharmacology, 146, 769-780 (2005).
[60] C. Sramek, M. Mackanos, R. Spitler, L.-S. Leung, H. Nomoto, C. H. Contag, and D. Palanker, "Non-damaging retinal phototherapy: dynamic range of heat shock protein expression," Invest Ophthalmol Vis Sci, 52(3), 1780-1787 (2011).
[61] J. Roider, N. A. Michaud, T. J. Flotte, and R. Birngruber, "Response of the retinal pigment epithelium to selective photocoagulation," Archives of ophthalmology, 110, 1786-1786 (1992).
[62] E. Richert, S. Koinzer, J. Tode, K. Schlott, R. Brinkmann, J. Hillenkamp, A. Klettner, and J. Roider, "Release of Different Cell Mediators During Retinal Pigment Epithelium Regeneration Following Selective Retina Therapy," Investigative ophthalmology visual science, 59, 1323-1331 (2018).

[63] C. Klatt, M. Saeger, T. Oppermann, E. P？¶rksen, F. Treumer, J. Hillenkamp, E. Fritzer, R. Brinkmann, R. Birngruber, and J. Roider, "Selective retina therapy for acute central serous chorioretinopathy," Br J Ophthalmol, 95(1), 83-88 (2011).
[64] H. Elsner, C. Klatt, S. H. M. Liew, E. Porksen, A. Bunse, M. Rudolf, R. Brinkmann, R. P. Hamilton, R. Birngruber, H. Laqua, and J. Roider, "Selective retina therapy in patients with diabetic maculopathy," Ophthalmologe, 103(10), 856-860 (2006).
[65] J. E. Shaw, R. A. Sicree, and P. Z. Zimmet, "Global estimates of the prevalence of diabetes for 2010 and 2030," Diabetes Res Clin Pract, 87(1), 4-14 (2010).
[66] E. Stefansson, T. Bek, M. Porta, N. Larsen, J. K. Kristinsson, and E. Agardh, "Screening and prevention of diabetic blindness," Acta ophthalmologica Scandinavica, 78, 374-385 (2000).
[67] U. K. P. D. S. Group, "Efficacy of atenolol and captopril in reducing risk of macrovascular and microvascular complications in type 2 diabetes: UKPDS 39. UK Prospective Diabetes Study Group," BMJ (Clinical research ed.), 317, 713-720 (1998).
[68] C. Diabetes, G. Complications Trial Research, D. M. Nathan, S. Genuth, J. Lachin, P. Cleary, O. Crofford, M. Davis, L. Rand, and C. Siebert, "The effect of intensive treatment of diabetes on the development and progression of long-term complications in insulin-dependent diabetes mellitus," N Engl J Med, 329(14), 977-86 (1993).
[69] Y. Ohkubo, H. Kishikawa, E. Araki, T. Miyata, S. Isami, S. Motoyoshi, Y. Kojima, N. Furuyoshi, and M. Shichiri, "Intensive insulin therapy prevents the progression of diabetic microvascular complications in Japanese patients with non-insulin-dependent diabetes mellitus: a randomized prospective 6-year study," Diabetes Res Clin Pract, 28(2), 103-17 (1995).
[70] C. H. Meyer, "Current treatment approaches in diabetic macular edema," Ophthalmologica, 221(2), 118-131 (2007).
[71] H. Lee, K. E. Kang, H. Chung, and H. C. Kim, "Prognostic Factors for Functional and Anatomic Outcomes in Patients with Diabetic Macular Edema Treated with Dexamethasone Implant," Korean J Ophthalmol, 32(2), 116-125 (2018).
[72] D. Group, "Progression of retinopathy with intensive versus conventional treatment in the Diabetes Control and Complications Trial. Diabetes Control and Complications Trial Research Group," Ophthalmology, 102(4), 647-61 (1995).
[73] E. S. Group, "Photocoagulation for diabetic macular edema. Early Treatment Diabetic Retinopathy Study report number 1. Early Treatment Diabetic Retinopathy Study research group," Arch Ophthalmol, 103(12), 1796-806 (1985).
[74] E. Group, "Photocoagulation for diabetic macular edema. Early Treatment Diabetic Retinopathy Study report number 1. Early Treatment Diabetic Retinopathy Study research group," Arch Ophthalmol, 103(12), 1796-806 (1985).
[75] E. Group, "Photocoagulation treatment of proliferative diabetic retinopathy. Clinical application of Diabetic Retinopathy Study (DRS)

findings, DRS Report Number 8. The Diabetic Retinopathy Study Research Group," Ophthalmology, 88(7), 583-600 (1981).
[76] E. Stefansson, D. L. Hatchell, B. L. Fisher, F. S. Sutherland, and R. Machemer, "Panretinal photocoagulation and retinal oxygenation in normal and diabetic cats," Am J Ophthalmol, 101(6), 657-64 (1986).
[77] M. B. Landers, 3rd, E. Stefansson, and M. L. Wolbarsht, "Panretinal photocoagulation and retinal oxygenation," Retina, 2(3), 167-75 (1982).
[78] D. Lavinsky, J. A. Cardillo, Y. Mandel, P. Huie, L. A. Melo, M. E. Farah, R. Belfort, and D. Palanker, "Restoration of retinal morphology and residual scarring after photocoagulation," Acta Ophthalmol, 91(4), e315-23 (2013).
[79] N. Lois, V. McBain, E. Abdelkader, N. W. Scott, and R. Kumari, "Retinal pigment epithelial atrophy in patients with exudative age-related macular degeneration undergoing anti-vascular endothelial growth factor therapy," Retina, 33(1), 13-22 (2013).
[80] U. Schmidt-Erfurth, C. Schuetze, S. Waldstein, B. Gerendas , C. Simader, L. Zhang, M. Abramoff, M. Sonka, B. Baumann, and H. Christoph, "Morphologic effects of anti-VEGF therapy on retinal pigment epithelium (RPE) and choroidal vasculature (CV) in neovascular age-related macular degeneration (AMD)." 54, 1.
[81] M. Young, L. Chui, N. Fallah, C. Or, A. B. Merkur, A. W. Kirker, D. A. Albiani, and F. Forooghian, "Exacerbation of choroidal and retinal pigment epithelial atrophy after anti-vascular endothelial growth factor treatment in neovascular age-related macular degeneration," Retina, 34(7), 1308-15 (2014).
[82] V. Sitnilska, L. Altay, P. Enders, M. Hermann, P. S. Muether, and S. Fauser, "Onset of Retinal Pigment Epithelium Atrophy Subsequent to Anti-VEGF Therapy in Patients with Neovascular Age-Related Macular Degeneration," Ophthalmologica, 241(3), 154-160 (2019).
[83] A. Li, N. B. Rieveschl, F. F. Conti, F. Q. Silva, J. E. Sears, S. Srivastava, J. P. Ehlers, A. P. Schachat, A. S. Babiuch, P. K. Kaiser, D. F. Martin, and R. P. Singh, "Long-Term Assessment of Macular Atrophy in Patients with Age-Related Macular Degeneration Receiving Anti-Vascular Endothelial Growth Factor," Ophthalmol Retina, 2(6), 550-557 (2018).
[84] M. Yamamoto, Y. Miura, K. Hirayama, T. Kohno, D. Kabata, D. Theisen-Kunde, R. Brinkmann, and S. Honda, "Predictive factors of outcome of selective retina therapy for diabetic macular edema," Int Ophthalmol, 40(5), 1221-1232 (2020).
[85] Y. G. Park, J. R. Kim, S. Kang, E. Seifert, D. Theisen-Kunde, R. Brinkmann, and Y. J. Roh, "Safety and efficacy of selective retina therapy (SRT) for the treatment of diabetic macular edema in Korean patients," Graefes Arch Clin Exp Ophthalmol, 254(9), 1703-13 (2016).
[86] G. Liew, G. Quin, M. Gillies, and S. Fraser-Bell, "Central serous chorioretinopathy: a review of epidemiology and pathophysiology," Clinical & experimental ophthalmology, 41(2), 201-214 (2013).
[87] L. A. Yannuzzi, "Type-A behavior and central serous chorioretinopathy," Retina (Philadelphia, Pa.), 7, 111-131 (1987).

[88] A. von Graefe, “Notizen und casaistische Mitheilugnen vermischtenInhalts: VI. Ueber zentrale recidivirende Retinitis,” Albrecht Von Graefes Arch Klin Exp Ophthalmol, 12(211-215), (1866).
[89] J. D. Gass, “Pathogenesis of disciform detachment of the neuroepithelium,” American journal of ophthalmology, 63, (1967).
[90] A. S. Kitzmann, J. S. Pulido, N. N. Diehl, D. O. Hodge, and J. P. Burke, “The incidence of central serous chorioretinopathy in Olmsted County, Minnesota, 1980-2002,” Ophthalmology, 115, 169-173 (2008).
[91] D. R. Guyer, L. A. Yannuzzi, J. S. Slakter, J. A. Sorenson, A. Ho, and D. Orlock, “Digital indocyanine green videoangiography of central serous chorioretinopathy,” Arch Ophthalmol, 112(8), 1057-1062 (1994).
[92] M. Spitznas, “Pathogenesis of central serous retinopathy: a new working hypothesis,” Graefe's Archive for Clinical and Experimental Ophthalmology, 224(4), 321-324 (1986).
[93] M. Gemenetzi, G. De Salvo, and A. J. Lotery, “Central serous chorioretinopathy: an update on pathogenesis and treatment,” Eye, 24(12), 1743-1756 (2010).
[94] L. Laatikainen, and M. Hoffren, “Long-term follow-up study of nonsenile detachment of the retinal pigment epithelium,” European journal of ophthalmology, 1, 79-84 (1991).
[95] R. F. Spaide, L. Campeas, A. Haas, L. A. Yannuzzi, Y. L. Fisher, D. R. Guyer, J. S. Slakter, J. A. Sorenson, and D. A. Orlock, “Central serous chorioretinopathy in younger and older adults,” Ophthalmology, 103, (1996).
[96] A. Daruich, A. Matet, A. Dirani, E. Bousquet, M. Zhao, N. Farman, F. Jaisser, and F. Behar-Cohen, “Central serous chorioretinopathy: Recent findings and new physiopathology hypothesis,” Prog Retin Eye Res, 48, 82-118 (2015).
[97] M. L. Klein, E. M. Van Buskirk, E. Friedman, E. Gragoudas, and S. Chandra, “Experience with nontreatment of central serous choroidopathy,” Archives of ophthalmology, 91(4), 247-250 (1974).
[98] D. T. Liu, A. C. Fok, W. Chan, T. Y. Lai, and D. S. Lam, [Retina] Elsevier, Central Serous Chorioretinopathy (2013).
[99] D. Bujarborua, “Long-term follow-up of idiopathic central serous chorioretinopathy without laser,” Acta Ophthalmologica Scandinavica, 79(4), 417-421 (2001).
[100] L. A. Yannuzzi, J. L. Shakin, Y. L. Fisher, and M. A. Altomonte, “Peripheral retinal detachments and retinal pigment epithelial atrophic tracts secondary to central serous pigment epitheliopathy,” Ophthalmology, 91(12), 1554-1572 (1984).
[101] T. Iida, L. A. Yannuzzi, R. F. Spaide, N. Borodoker, C. A. Carvalho, and S. Negrao, “Cystoid macular degeneration in chronic central serous chorioretinopathy,” Retina, 23(1), 1-7 (2003).
[102] M. S. M. Wang, B. Sander, and M. Larsen, “Retinal atrophy in idiopathic central serous chorioretinopathy,” American journal of ophthalmology, 133(6), 787-793 (2002).
[103] F. C. Piccolino, C. M. Eandi, L. Ventre, R. Roberta, and F. M. Grignolo, “Photodynamic therapy for chronic central serous chorioretinopathy,” Retina, 23(6), 752-763 (2003).

[104] W. M. Chan, D. S. C. Lam, T. Y. Y. Lai, B. S. M. Tam, D. T. L. Liu, and C. K. M. Chan, "Choroidal vascular remodelling in central serous chorioretinopathy after indocyanine green guided photodynamic therapy with verteporfin: a novel treatment at the primary disease level," British journal of ophthalmology, 87(12), 1453-1458 (2003).
[105] T. Y. Y. Lai, W.-M. Chan, and D. S. C. Lam, "Transient reduction in retinal function revealed by multifocal electroretinogram after photodynamic therapy," American journal of ophthalmology, 137(5), 826-833 (2004).
[106] R. Tzekov, T. Lin, K.-M. Zhang, B. Jackson, A. Oyejide, W. Orilla, A. D. Kulkarni, B. D. Kuppermann, L. Wheeler, and J. Burke, "Ocular changes after photodynamic therapy," Investigative ophthalmology & visual science, 47(1), 377-385 (2006).
[107] P. Y. Lee, K. S. Kim, and W. K. Lee, "Severe choroidal ischemia following photodynamic therapy for pigment epithelial detachment and chronic central serous chorioretinopathy," Japanese journal of ophthalmology, 53(1), 52-56 (2009).
[108] T. Y. Y. Lai, W.-M. Chan, H. Li, R. Y. K. Lai, D. T. L. Liu, and D. S. C. Lam, "Safety enhanced photodynamic therapy with half dose verteporfin for chronic central serous chorioretinopathy: a short term pilot study," British journal of ophthalmology, 90(7), 869-874 (2006).
[109] W.-M. Chan, T. Y. Y. Lai, R. Y. K. Lai, D. T. L. Liu, and D. S. C. Lam, "Half-dose verteporfin photodynamic therapy for acute central serous chorioretinopathy: one-year results of a randomized controlled trial," Ophthalmology, 115(10), 1756-1765 (2008).
[110] M.-W. Zhao, P. Zhou, H.-X. Xiao, Y.-S. Lv, C.-A. Li, G.-D. Liu, and X.-X. Li, "Photodynamic therapy for acute central serous chorioretinopathy: the safe effective lowest dose of verteporfin," Retina, 29(8), 1155-1161 (2009).
[111] M. Reibaldi, N. Cardascia, A. Longo, C. Furino, T. Avitabile, S. Faro, M. Sanfilippo, A. Russo, M. G. Uva, F. Munno, and others, "Standard-fluence versus low-fluence photodynamic therapy in chronic central serous chorioretinopathy: a nonrandomized clinical trial," American journal of ophthalmology, 149(2), 307-315 (2010).
[112] Greite, and Birngruber, "Low Intensity Argon Laser Coagulation in Ceirtsal Serous Reinopaty (CSR)," OphtlhalmoIogica, Basel, 171, 214-223 (1975).
[113] L. Ficker, G. Vafidis, A. While, and P. Leaver, "Long-term follow-up of a prospective trial of argon laser photocoagulation in the treatment of central serous retinopathy," British journal of ophthalmology, 72(11), 829-834 (1988).
[114] Maia, "A New Treatment for Chronic Central Serous Retinopathy," Retina today, 1, 62-64 (2010).
[115] F. Ricci, F. Missiroli, F. Regine, M. Grossi, and G. Dorin, "Indocyanine green enhanced subthreshold diode-laser micropulse photocoagulation treatment of chronic central serous chorioretinopathy," Graefes Arch Clin Exp Ophthalmol, 247(5), 597-607 (2009).
[116] S.-N. Chen, J.-F. Hwang, L.-F. Tseng, and C.-J. Lin, "Subthreshold diode micropulse photocoagulation for the treatment of chronic central

serous chorioretinopathy with juxtafoveal leakage," Ophthalmology, 115(12), 2229-2234 (2008).
[117] F. Ricci, F. Missiroli, and L. Cerulli, "Indocyanine green dye-enhanced micropulsed diode laser: a novel approach to subthreshold RPE treatment in a case of central serous chorioretinopathy," Eur J Ophthalmol, 14(1), 74-82 (2004).
[118] P. Lanzetta, F. Furlan, L. Morgante, D. Veritti, and F. Bandello, "Nonvisible subthreshold micropulse diode laser (810 nm) treatment of central serous chorioretinopathy. A pilot study," Eur J Ophthalmol, 18(6), 934-940 (2008).
[119] C. Klatt, H. Elsner, E. Poerksen, R. Brinkmann, A. Bunse, R. Birngruber, and J. Roider, "Selektive Retina-Therapie bei Retinopathia centralis serosa mit Pigmentepithelabhebung," Der Ophthalmologe, 103(10), 850-855 (2006).
[120] H. Elsner, E. Porksen, C. Klatt, A. Bunse, D. Theisen-Kunde, R. Brinkmann, R. Birngruber, H. Laqua, and J. Roider, "Selective retina therapy in patients with central serous chorioretinopathy," Graefes Arch Clin Exp Ophthalmol, 244(12), 1638-1645 (2006).
[121] C. Framme, A. Walter, L. Berger, P. Prahs, C. Alt, D. Theisen-Kunde, J. Kowal, and R. Brinkmann, "Selective Retina Therapy in Acute and Chronic-Recurrent Central Serous Chorioretinopathy," Ophthalmologica, 234(4), 177-88 (2015).
[122] A. Yasui, M. Yamamoto, K. Hirayama, K. Shiraki, D. Theisen-Kunde, R. Brinkmann, Y. Miura, and T. Kohno, "Retinal sensitivity after selective retina therapy (SRT) on patients with central serous chorioretinopathy," Graefes Arch Clin Exp Ophthalmol, 255(2), 243-254 (2017).
[123] S. Kang, Y. G. Park, J. R. Kim, E. Seifert, D. Theisen-Kunde, R. Brinkmann, and Y. J. Roh, "Selective Retina Therapy in Patients With Chronic Central Serous Chorioretinopathy: A Pilot Study," Medicine (Baltimore), 95(3), e2524 (2016).
[124] R. Birngruber, [Thermal modeling in biological tissue] Plenum Press (1980).
[125] R. Birngruber, F. Hillenkamp, and V.-P. Gabel, "Theoretical investigations of laser thermal retinal injury," Health Physics, 48(6), 781-796 (1985).
[126] Kandulla, "Experimentelle und theoretische Untersuchungen zur optoakustischen Temperaturbestimmung während Transpupillarer Thermotherapie", Lübeck University, 2009
[127] D. E. Freund, R. L. McCally, R. A. Farrell, and D. H. Sliney, "A Theoretical Comparison of Retinal Temperature Changes Resulting from Exposure to Rectangular and Gussian Beams," Lasers Life Sc., 7(2), 71-89 (1996).
[128] Neumann, and Brinkmann, "Boiling nucleation on melanosomes and microbeads transiently heated by nanosecond and microsecond laser pulses," Journal of biomedical optics, 10(2), 024001-02400112 (2005).
[129] J. Neumann, and R. Brinkmann, "Microbubble Dynamics around Melanosomes Irradiated with Microsecond Pulses." 4617, 180-6.

[130] J. Neumann, and R. Brinkmann, “Self-limited growth of laser-induced vapor bubbles around single microabsorbers,” Applied Physics Letters, 93(3), 033901-033901 (2008).
[131] C. E. Brennen, [Cavitation and Bubble Dynamics] Oxford University Press, New York(1995).
[132] R. A. Wentzell, “Van der Waals Stabilization of Bubbles,” Physical Review Letters, 56(7), 732-733.
[133] B. Yasunori, and N. Hideaki, “Boiling Acoustic Emission and Bubble Dynamics in Nucleate Boiling,” Journal of Nuclear Science and Technology, 13(9), 520-522 (1976).
[134] G. Schule, P. Huie, A. B. Vankov, E. Vitkin, H. Fang, E. B. Hanlon, L. T. Perelman, and D. V. Palanker, "Noninvasive monitoring of the thermal stress in RPE using light scattering spectroscopy." 95-99.
[135] J. Kandulla, and R. Brinkmann, “Non invasive real-time temperature determination during laser treatments at the retina,” Photonik Stuttgart, 40(1), 42 (2008).
[136] G. Schüle, H. Elsner, C. Framme, J. Roider, R. Birngruber, and R. Brinkmann, “Optoacoustic real-time dosimetry for selective retina treatment,” J. Biomed. Opt., 10(6), 064022 (2005).
[137] G. Schülle, G. Hu, C. Framme, J. Roider, and R. Brinkmann, “Noninvasive optoacoustic temperature determination at the fundus of the eye during laser irradiation,” Journal of biomedical optics, 9(1), 173-179 (2004).
[138] J. Neumann, and R. Brinkmann, “Boiling nucleation on melanosomes and microbeads transiently heated by nanosecond and microsecond laser pulses,” Journal of biomedical optics, 10(2), 024001-02400112 (2005).
[139] J. Neumann, "Mikroskopische Untersuchungen zur laserinduzierten Blasenbildung und -dynamik an absorbierenden Mikropartikeln", Universität zu Lübeck, 2005
[140] R. Brinkmann, S. Koinzer, K. Schlott, L. Ptaszynski, M. Bever, A. Baade, S. Luft, Y. Miura, J. Roider, and R. Birngruber, “Real-time temperature determination during retinal photocoagulation on patients,” Journal of Biomedical Optics, 17(6), 0612191-06121910 (2012).
[141] J. Roider, F. Hillenkamp, T. Flotte, and R. Birngruber, “Microphotocoagulation: selective effects of repetitive short laser pulses,” Proc Natl Acad Sci U S A, 90(18), 8643-7 (1993).
[142] D. Lavinsky, J. Wang, P. Huie, R. Dalal, S. J. Lee, D. Y. Lee, and D. Palanker, “Nondamaging Retinal Laser Therapy: Rationale and Applications to the Macula,” Invest Ophthalmol Vis Sci, 57(6), 2488-500 (2016).
[143] S. J. Till, P. K. Milsom, and G. Rowlands, “A New Model for Laser-Induced Thermal Damage in the Retina,” B. Math. Biol., 65, 731-46 (2003).
[144] C. P. Lin, M. W. Kelly, S. A. B. Sibayan, M. A. Latina, and R. R. Anderson, “Selective Cell Killing by Microparticle Absorption of Pulsed Laser Radiation,” IEEE J select Topics Quantum Electron, 5(4), 963-968 (1999).
[145] B. S. Gerstman, C. R. Thompson, S. L. Jacques, and M. E. Rogers, “Laser-induced bubble formation in the retina,” 2391, 60-71 (1995).

[146] E. Seifert, S. R. Sonntag, P. Kleingarn, D. Theisen-Kunde, S. Grisanti, R. Birngruber, Y. Miura, and R. Brinkmann, “Investigations on Retinal Pigment Epithelial Damage at Laser Irradiation in the Lower Microsecond Time Regime,” Invest Ophthalmol Vis Sci, 62(3), 32 (2021).
[147] Kandulla, elsner, Hilmes, Hartert, Birngruber, and Brinkmann, “Optoacoustic temperature determination at the fundus of the eye during Transpupillary Thermotherapy,” SPIE, 5688, 208-214 (2005).
[148] G. Schule, G. Huttmann, C. Framme, J. Roider, and R. Brinkmann, “Noninvasive optoacoustic temperature determination at the fundus of the eye during laser irradiation,” J Biomed Opt, 9(1), 173-179 (2004).
[149] C. P. Lin, and M. W. Kelly, “Cavitation and acoustic emission around laser-heated microparticles,” Applied Physics Letters, 72(22), 2800-2802 (1998).
[150] G. Mie, “Beitrage zur Optik trüber Medien, speziell kolloidaler Metallosungen,” Annalen der Physik, 330 (3), 377-445 (1908).
[151] D. R. H. Craig F. Bohren, [Absorption and Scattering of Light by Small Particles] WILEY-VCH (2007).
[152] J.-P. Schäfer, "Implementierung und Anwendung analytischer und numerischer Verfahren zur Lösung der Maxwellgleichungen für die Untersuchung der Lichtausbreitung in biologischem Gewebe", Univerität Ulm, PhD, 2011
[153] J. Schäfer, S.-C. Lee, and A. Kienle, “Calculation of the near fields for the scattering of electromagnetic waves by multiple infinite cylinders at perpendicular incidence,” J. Quant. Spectrosc. Radiat. Trans., 113(16), (2012).
[154] J. W. Goodman, [Introduction to Fourier Optics] McGraw-Hill Companies, (1996).
[155] J. W. Goodman, [Speckle Phenomena In Optics] Roberts and company Publishers, (2007).
[156] C. F. Bohren, and D. R. Huffman, [Absorption and scattering of light by small particles] John Wiley and Sons, (2008).
[157] C. Alt, "Detection of Intracellular Cavitation During Selective Targeting of the Retinal Pigment Epithelium With a Laser Scanner", Tufts University, 2008
[158] H. Lee, C. Alt, C. M. Pitsillides, and C. P. Lin, “Optical detection of intracellular cavitation during selective laser targeting of the retinal pigment epithelium: dependence of cell death mechanism on pulse duration,” J. Biomed. Opt., 12(6), 064034 (2007).
[159] G. Schuele, M. Rumohr, G. Huettmann, and R. Brinkmann, “RPE damage thresholds and mechanisms for laser exposure in the microsecond-to-millisecond time regimen,” Investigative ophthalmology & visual science, 46(2), 714-719 (2005).
[160] M. Dahlke, "Entwicklung und Aufbau eines mikrokontroller-gestützten Systems zur auautomatisch Abschaltung beid der Selektive Retina Therapie", 2009
[161] J. Krieger, "Untersuchungen zu einem fasergestützten, Reflektometrisch-optischen Dosimetrieverfahren für die Selektive Retina Therapie (SRT)", Lübeck university, 2010

[162] E. Seifert, "Fiber optic reflectometry for Selective Retina Treatment", Aalen University of Applied Sciences, 2011
[163] G. Schüle, "Mechanismen und On-line Dosimetrie bei selektiver RPE Therapie", Universität zu Lübeck, 2002
[164] C. Framme, G. Schüle, J. Roider, D. Kracht, R. Birngruber, and R. Brinkmann, "Threshold determinations for selective retinal pigment epithelium damage with repetitive pulsed microsecond laser systems in rabbits," Ophthalmic Surg Lasers, 33(5), 400-409 (2002).
[165] K. Minhee, Y. G. Park, S. Kang, and Y. J. Roh, "Comparison of the tissue response of selective retina therapy with or without real-time feedback-controlled dosimetry," Graefes Arch Clin Exp Ophthalmol, 256(9), 1639-1651 (2018).
[166] R. Birngruber, E. Drechsel, F. Hillenkamp, and V. P. Gabel, "Minimal spot size on the retina formed by the optical system of the eye," Int Ophthalmol, 1(3), 175-8 (1979).
[167] F. A. Davis, "The anatomy and histology of the eye and orbit of the rabbit," Transactions of the American Ophthalmological Society, 27, 400-2 (1929).
[168] M. Tenopoulou, T. Kurz, P. T. Doulias, D. Galaris, and U. T. Brunk, "Does the calcein-AM method assay the total cellular 'labile iron pool' or only a fraction of it?," Biochem J, 403(2), 261-6 (2007).
[169] Roider, Hillenkamp, Flotte, and Birngruber, "Microphotocoagulation: selective effects of repetitive short laser pulses," Proceedings of the National Academy of Sciences, 90(18), 8643-8647 (1993).
[170] R. G. Borland, D. H. Brennan, J. Marshall, and J. P. Viveash, "The Role of Fluorescence Angiography in the Detection of Laser-Induced Damage to the Retina: A Threshold Study for Q-Switched, Neodymium and Ruby Lasers," Exp. Eye Res., 27, 471-93 (1978).
[171] Birngruber, Puliafito, Gawande, Lin, Schoenlein, and Fujimoto, "Femtosecond laser-tissue interactions: Retinal injury studies," Quantum Electronics, IEEE Journal of, 23(10), 1836-1844 (1987).
[172] R. G. Newcombe, "Two-sided confidence intervals for the single proportion: comparison of seven methods," Statistics in medicine, 17(8), 857-872 (1998).
[173] A. P. Bradley, "The use of the area under the roc curve in the evaluation of machine learning algorithms," Pattern Recognition, 30(7), 1145-1159 (1997).
[174] W. J. Youden, "Index for rating diagnostic tests," Cancer, 3(1), 32-5 (1950).
[175] D. H. Sliney, J. Mellerio, V. P. Gabel, and K. Schulmeister, "What Is the Meaning of Threshold in Laser Injury Experiments Implications for Human Exposure Limits," Health Phys., 82(3), 335-47 (2002).
[176] Finney, [Probit Analysis A Statistical threatment of the sigmoid response curve] Cambridge university press, (1952).
[177] Y.-G. Park, E. Seifert, Y. J. Roh, D. Theisen-Kunde, S. Kang, and R. Brinkmann, "Tissue response of selective retina therapy by means of a feedback-controlled energy ramping mode," Clinical and experimental ophthalmology, 42(9), 846-855 (2014).

[178] Y. G. Park, S. Kang, R. Brinkmann, and Y.-J. Roh, “A Comparative Study of Retinal Function in Rabbits after Panretinal Selective Retina Therapy versus Conventional Panretinal Photocoagulation,” J Ophthalmol, 2015, 247259 (2015).
[179] E. Seifert, J. Tode, A. Pielen, D. Theisen-Kunde, C. Framme, J. Roider, Y. Miura, R. Birngruber, and R. Brinkmann, “Selective retina therapy: toward an optically controlled automatic dosing,” J Biomed Opt, 23(11), 1-12 (2018).
[180] E. Seifert, J. Tode, A. Pielen, D. Theisen-Kunde, C. Framme, J. Roider, Y. Miura, R. Birngruber, and R. Brinkmann, “Algorithms for optoacoustically controlled selective retina therapy (SRT),” Photoacoustics, 25, 100316 (2022).
[181] M. W. Kelly, "Intracellular Cavitation as a Mechanism of Short-Pulse Laser Injury to the Retinal Pigment Epithelium", Tufts University, 1997
[182] J. Roegener, R. Brinkmann, and C. P. Lin, “Pump-probe detection of laser-induced microbubble formation in retinal pigment epithelium cells,” Journal of Biomedical Optics, 9(2), 367-371 (2004).
[183] C. Alt, C. Framme, S. Schnell, H. Lee, R. Brinkmann, and C. P. Lin, “Selective targeting of the retinal pigment epithelium using an acousto-optic laser scanner,” J Biomed Opt, 10(6), 064014 (2005).
[184] C. Framme, A. Walter, P. Prahs, R. Regler, D. Theisen-Kunde, C. Alt, and R. Brinkmann, “Structural changes of the retina after conventional laser photocoagulation and selective retina treatment (SRT) in spectral domain OCT,” Curr Eye Res, 34(7), 568-579 (2009).
[185] J. Roider, N. A. Michaud, T. J. Flotte, and R. Birngruber, “Response of the retinal pigment epithelium to selective photocoagulation,” Arch Ophthalmol, 110(12), 1786-92 (1992).

9 Acknowledgments

This work would not have been possible without the support of many people. I want to thank Prof. Dr. phil. nat. Dr. med. habil. Reginald Birngruber for his time, support, and constructive criticism. Furthermore, I want to thank Dr. rer. nat. Ralf Brinkmann for enabling the research projects and for his trust and support.

The studies presented in this work would not have been possible without the work of many clinicians. I want to thank the team of the ophthalmological department of the university clinic Schleswig Holstein campus Lübeck for the excellent collaboration in multiple studies. Especially Dr. med. Yoko Miura and Dr. med. Svenja Sonntag. I also want to thank the team of the ophthalmological department of the university clinic Schleswig Holstein campus Kiel, including Prof. Dr. med. Johann Roider and Dr. med. Jan Tode, for the collaboration in the SRT-Study which is also presented in this work. Furthermore, I want to thank the team of the ophthalmological department of the medical school Hannover, including Prof. Dr. med. Carsten Framme and Dr. med. Amelie Pielen, for the collaboration in the SRT-Study presented in this work. I also like to thank the team of the ophthalmological department of the St Maries Hospital, including Young-Jung Roh MD PhD, Yong-Gun Park MD, Seungbum Kang MD and Min-Hee Kim MD, for the collaboration in the three SRT studies.

All the studies would not have been possible without the engineers making the clinical devices. Thus, I like to thank my colleagues of the Medical Lasercenter Lübeck for their support.

Furthermore I like to thank Lutronic Corp, for the collaboration during the development of the R:GEN system and for supplying the R:GEN system for the SRT studies.

I also like to thank ARC Laser GmbH, for supplying the diode-laser prototype.

Finally, I like to thank the Korea Institute for Advancement of Technology and the German Federal ministry of education and research for funding the research projects.